Dissertation

submitted to the
Combined Faculties of the Natural Sciences and Mathematics
of the Ruperto-Carola-University of Heidelberg, Germany,
for the degree of
Doctor of Natural Sciences

Put forward by

Michael Vincent Maseda
born in: Tampa, Florida, United States of America

Oral examination: 8 July, 2015

STARBURSTING DWARF GALAXIES AT $z > 1$

– A NEAR-INFRARED SPECTROSCOPIC STUDY –

MICHAEL VINCENT MASEDA

UNDER THE SUPERVISION OF: PROF. DR. HANS-WALTER RIX
DR. ARJEN VAN DER WEL

REFEREES: PROF. DR. HANS-WALTER RIX
PROF. DR. EVA GREBEL

A QUIEN LEYERE

Si las páginas de este libro consienten algún verso feliz, perdóneme el lector la descortesía de haberlo usurpado yo, previamente. Nuestras nadas poco difieren; es trivial y fortuita la circunstancia de que tú seas el lector de estos ejercicios, y yo su redactor.

~Jorge Luis Borges~

CONTENTS

List of Figures

LIST OF TABLES

ABSTRACT

The episodic star-formation histories of dwarf galaxies with present-day stellar masses $\lesssim 10^9\,M_\odot$ present a challenge to our current understanding of galaxy formation and evolution. Hydrodynamical simulations predict that star formation in these galaxies was very burst-like in the past, with feedback in the form of supernovae and winds that heat and deplete the central cold gas reservoirs. Repeated starburst events have been cited as the driving force behind intense feedback that can change the central dark matter profile, potentially addressing one of the principal challenges to the standard Cold Dark Matter cosmological model. Until recently, dwarf galaxies have only been studied in the local universe. Here we use a combination of multiwavelength photometry and near-IR grism spectroscopy to identify an abundant population of extreme emission line galaxies (EELGs) at $z > 1$. Sophisticated modeling of their spectral energy distributions reveals that EELGs, selected only based on their large equivalent widths, have low *stellar* masses. Our high-resolution follow-up spectroscopy in the near-IR shows that the emission lines are very narrow, implying low *total dynamical* masses. Emission line ratios are consistent with low gas-phase metallicities and also demonstrate that the strong emission comes from hot young stars. Therefore, these objects show all the signatures of dwarf galaxies at $z > 1$. By developing a novel method to detect strong emission line sources in grism spectroscopic data, we trace the evolution in the number density of EELGs with cosmic time, observing that they are more than an order of magnitude more common at $z = 2$ than locally. This observationally supports the importance of bursty star-formation in low-mass galaxies at $z > 1$, implying that most stars in today's dwarf galaxies formed in a small number of these early bursts. Taken together, these results constitute the first comprehensive observational study of dwarf galaxies at high redshift.

ZUSAMMENFASSUNG

Die episodische Sternentstehungshistorie von Zwerggalaxien mit heutigen stellaren Massen $\lesssim 10^9\ M_\odot$ stellen eine Herausforderung für unser gegenwärtiges Verständnis der Galaxienentstehung und -entwicklung dar. Hydrodynamischen Simulationen sagen voraus, dass die Sternentstehung in diesen Galaxien abrupt einsetzte und dur Rückkopplung, in Form von Supernovae und Sternwinden, die verbliebenen Vorräte kalten Gases aufheizen. Es wird vermutet, dass wiederholte Sternentstehungsepisoden durch intensive Rückkopplungsvorgänge die Dichteverteilung dunkler Materie im Zentrum der Galaxien verringern können. Dieser Mechanismus stellt eine potentielle Lösung eines der Hauptprobleme des Standarmodelles der Kosmologie dar. Zwerggalaxien wurden bislang nur im lokalen Universum untersucht. Wir verwenden hier eine Kombination aus Multiwellenlängenphotometrie und Nahinfrarotgitterprismaspektroskopie um die zahlreich vorhandenen Extremeemissionsliniengalaxien (hier genannt EELGs) mit $z > 1$ aufzuspüren. Umfangreiche Modellierungen ihrer spektralen Energiedichten zeigen, dass EELGs, welche lediglich nach möglichst großer Äquivalentbreite selektiert wurden, eine geringe *stellaren* Masse aufweisen. Unsere nachfolgenden hochauflösenden Nahinfrarotspektroskopiebeobachtungen zeigen sehr schmale Emissionslinien auf, was auf geringe *total dynamische* Massen hindeutet. Die relativen Intensitäten der Emissionslinie sind konsistent mit niedrigen Gasphasenmetallizitäten und belegen, dass der Ursprung der starken Emission heiße junge Sterne sind. Diese Objekte weisen also alle Merkmale von Zwerggalaxien mit $z > 1$ auf. Mit Hilfe von einer neuartigen Methode zur Entdeckung starker Emissionslinie in gitterprismaspektroskopischen Daten bestimmen wir die Häufigkeit von EELGs als Funktion der kosmischen Rotverschiebung und stellen fest, dass diese bei $z = 2$ um mehr als eine Größenordung über dem lokalen Wert liegt. Dies unterstreicht die Wichtigkeit episodischer Sternentstehung in kleinen Galaxien bei $z > 1$ und impliziert so, dass die meisten Sterne in heutigen Zwerggalaxien in nur wenigen dieser frühen Sternentstehungsepisoden entstanden. In ihrer Gesamtheit stellt diese Arbeit die erste umfassende Beobachtungsstudie von Zwerggalaxien bei großen Rotverschiebungen dar.

Chapter 1

Introduction

[E]s sind Systemata von, so zu sagen, unendliche mal unendlich größerm Durchmesser, als der Diameter unseres Sonnenbaues ist, aber ohne Zweifel auf gleiche Art entstanden, aus gleichen Ursachen geordnet und eingerichtet und erhalten sich durch ein gleiches Triebwerk, als dieses in ihrer Verfassung.

Immanuel Kant
Allgemeine Naturgeschichte und Theorie Des Himmels, 1755

While the term "galaxy" is loosely defined, the narrowest description is a collection of baryonic material at the center of a dark matter potential well. The exact nature of the interplay between the baryons and the dark matter to form luminous structures can in principle be described using nothing but well-understood physics, yet the vast differences in the scales of interactions and uncertain initial conditions prevent us from deriving a simple, complete model of galaxy formation from first principles. If we want to understand the process, then, we can either create simulations based on simplified physical models or perform observations of galaxies at different stages of formation, aided by the finite speed of light and hence the ability to observe galaxies in the (distant) past. These two methods are technically independent but progress is most rapid when they work in tandem: observations inform simulations about what the real universe looks like, and simulations allow for a physical interpretation of observations as well as making observable predictions.

1.1 Cosmological Framework

The idea that the "nebular" regions of the night sky were external to the Milky Way and that the Milky Way itself was a disk of stars was developed in the 18th century by Immanuel Kant and Thomas Wright, among others. Over time, the idea gained support but failed to gain widespread recognition until after the "Great Debate" between Harlow Shapley and Heber Curtis in 1920; determinations of the large nebula in Andromeda via novae (e.g. Lundmark 1925) or Cepheid variable stars (e.g. Hubble 1929)

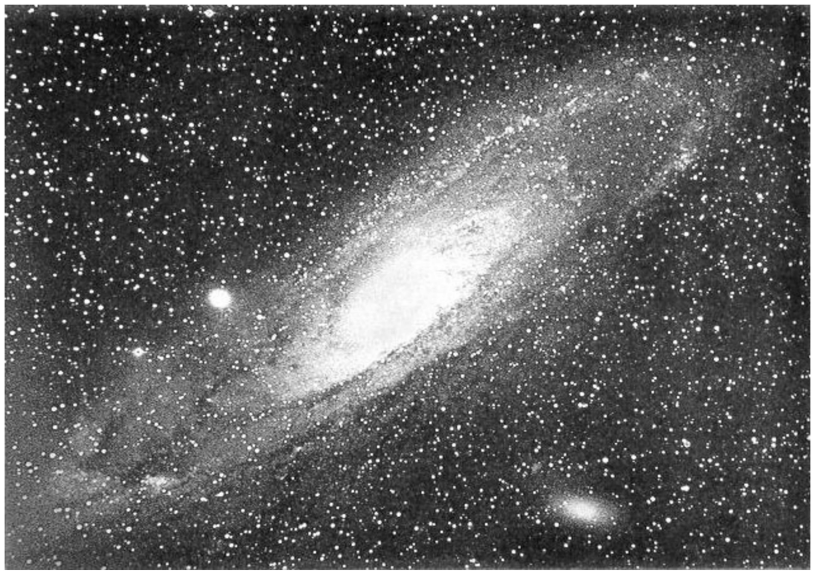

FIGURE 1.1: *The first photograph taken of the Andromeda galaxy, then known as the "Great Nebula in Andromeda" (Roberts 1893).*

showed that it was located at too far away to be part of the Milky Way[1] and must therefore be a separate galaxy. Thus, the "Great Nebula in Andromeda" (see Figure 1.1) became the "Andromeda galaxy."

This notion has immense consequences when combined with the discovery of the expansion of the universe and the implication that objects recede from each other at a rate proportional to their distance by Lemaître (1927, based on the observations of Stromberg 1925; Hubble 1926): since the speed of light is finite, observations of distant objects show light that was emitted in the past. Modern cosmological studies were forever changed in the 1960s with the discovery of the Cosmic Microwave Background (CMB; Penzias & Wilson 1965) and the recognition that such radiation could have been caused by the Big Bang (Dicke et al. 1965, see also Section 1.3). Once Penzias and Wilson were certain that the signal was real and not caused by terrestrial (the infamous "white dielectric material") or galactic sources, the field of observational cosmology was born. The spectrum of the CMB is the closest to Planck's ideal *blackbody* as anything ever observed in nature, measured to have a temperature $T = 2.72548 \pm 0.00057$ K (Fixsen 2009 and Figure 1.2).

When the universe was younger and denser, shortly after the Big Bang, the temperature of the baryonic plasma was so high that protons and electrons remained separated. The distribution of particles at these early times was fairly, but not completely, uniform. Once the universe expanded and cooled to ~ 3000 K at $z \sim 1100$, the charged particles were able to combine to form neutral atoms in what has been termed "Recombination" (although the charged particles were never previously combined). Shortly

[1] Hubble's value of 275 kpc and Lundmark's value of 430 kpc are still much smaller than the currently-accepted value of 770 kpc (Karachentsev et al. 2004).

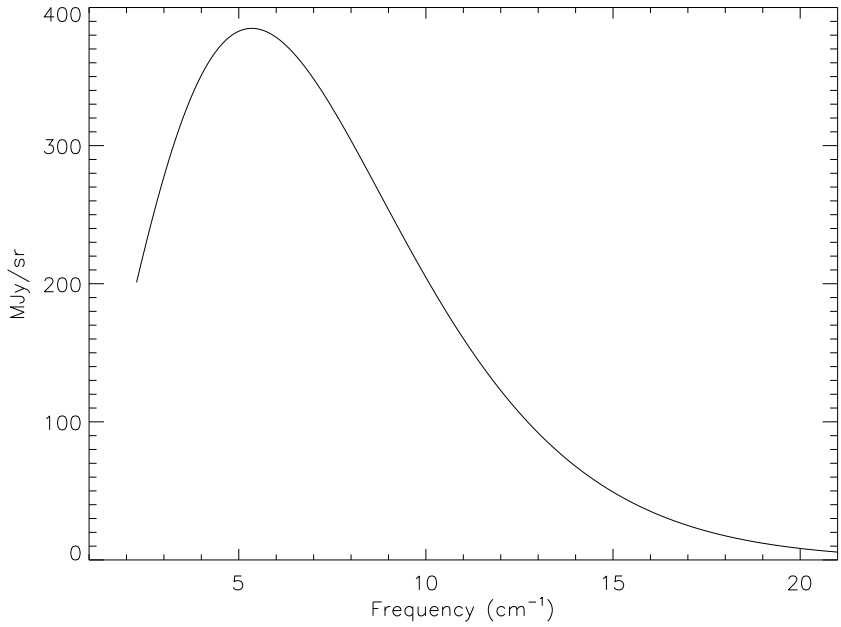

Figure 1.2: *Uniform CMB spectrum and fit to a Planck blackbody ($T = 2.728$ K) from COBE. Uncertainties are a small fraction of the line thickness. (Figure 5 from Fixsen et al. 1996)*

afterwards, the mean free path for photons became much larger than the Hubble distance (the distance at which objects are receding at a rate faster than the speed of light) and hence the universe filled with photons propagating with a blackbody distribution of frequencies. As the universe expanded further, the photons were redshifted and the temperature of this blackbody decreased. These photons reach us today as the (nearly) isotropic CMB, providing an image of the surface of last scattering at $z \sim 1100$.

The space-based COBE, WMAP, and Planck missions (Boggess et al. 1992; Bennett et al. 2003; Tauber et al. 2010, respectively), as well as balloon- and rocket-based studies (e.g. Johnson & Wilkinson 1987; Gush et al. 1990), have all confirmed small anisotropies in the CMB. These anisotropies can be attributed to small differences in the density structure of the universe at very early times. Such minute differences (about 1 part in 100,000; Bennett et al. 1996) are actually too small to be signatures of the initial density perturbations that later formed the most massive galaxies observed in the present-day universe due to baryonic self-gravitation alone, which would be a factor of 10 to 100 larger (Peebles & Yu 1970). This tension can be solved if baryons do not make up the majority of the mass budget of the universe: if there is a significant contribution from massive, weakly-interacting particles, density fluctuations on small scales can grow even before photon decoupling during Recombination since their velocity dispersions are too low to be damped on large scales by free streaming (Peebles 1982; Blumenthal et al. 1984). Such a prediction for "cold" dark matter (as opposed to e.g. "hot" dark matter consisting of neutrinos), based primarily on cosmology, agreed with various observations of galaxies that also indicate that a significant amount of mass is missing.

Arguably the first of these observations was performed by Zwicky (1933) who discovered that, if the Virgo cluster of galaxies is bound, the total mass must consid-

erably exceed the sum of the masses of the individual member galaxies. This missing mass was termed "dunkle Materie" or "dark matter." Later observations of spiral galaxy rotation curves, starting with Rubin & Ford (1970), showed that they flattened at large radii instead of decreasing. Since most of the material in the disk of a spiral galaxy is moving in a circular orbit, the balance between centrifugal force and gravity implies that the rotational velocity should decrease with radius. The observed flattening, therefore, is a sign that the mass density does not decrease significantly with radius. Since this trend continues even beyond the edge of the visible portion of the galaxy, the only plausible explanation is non-luminous material. Similar arguments can be applied to elliptical galaxies, where the virial theorem can be used to show that the average kinetic energy far exceeds the gravitational potential energy from the luminous matter alone.

One candidate for non-luminous but baryonic matter is intergalactic gas. Atomic Hydrogen would be visible via 21-cm absorption (created by a flip in the spin of the Hydrogen atom's electron: Ewen & Purcell 1951; Muller & Oort 1951), while ionized Hydrogen would produce thermal *Bremsstrahlung* radiation which would be visible in radio and X-ray observations. Other dark, low-mass baryonic objects (e.g. dwarf stars, black holes, planets) would be so numerous as to cause frequent gravitational microlensing events, which have not been convincingly observed (Alcock et al. 2000; Tisserand et al. 2007).

1.2 FROM PHYSICS TO GALAXIES

Simulating collisionless dark matter particles through N-body methods first occurred close to the same time as the first observations of the CMB (von Hoerner 1960, 1963, although the first "numerical" simulations were performed in an ingenious way using lightbulbs by Holmberg 1941). Since then, they have rapidly developed in complexity and are well-understood given the simplifying nature of their physical assumptions. These simulations have triumphed in reproducing the growth of large scale structures in the universe (e.g. Springel et al. 2005) and matching the observed clustering distribution of galaxies (e.g. Benson et al. 2000a,b; Norberg et al. 2001). Within this cold dark matter (CDM) framework, galaxies are predicted to live in dark matter halos that extend significantly beyond their visible boundaries. While the edge of a dark matter halo is an ill-defined concept, observations have supported the idea that in massive cases they extend several hundred kiloparsecs from the center (Zaritsky et al. 1993).

By combining the observed mass function of galaxies with N-body simulations of dark matter halos, Moster et al. (2010) parameterized the crucial relationship between a galaxy's stellar mass and the mass of its dark matter halo. As shown in Figure 1.3, star formation is most efficient in dark matter halos of mass $M \sim 10^{12}\ M_\odot$, which typically host galaxies with stellar mass $m \sim 3 \times 10^{10}\ M_\odot$. Perhaps unsurprisingly, we believe that the Milky Way lives in a dark matter halo with a mass of $\sim 1.2 \times 10^{12}\ M_\odot$ and has a stellar mass of $\sim 6.4 \times 10^{10}\ M_\odot$ (McMillan 2011).

Rather than viewing the peak in Figure 1.3 as the most efficient halo mass for star formation, we can view it as the *least inefficient* halo mass for star formation. That is, the critical halo mass of $\sim 10^{12}\ M_\odot$ is simply the crossover point between the efficacy of two separate feedback processes: stellar feedback is thought to dominate at low masses and active galactic nuclei (AGN) feedback is thought to dominate at high masses. Feedback

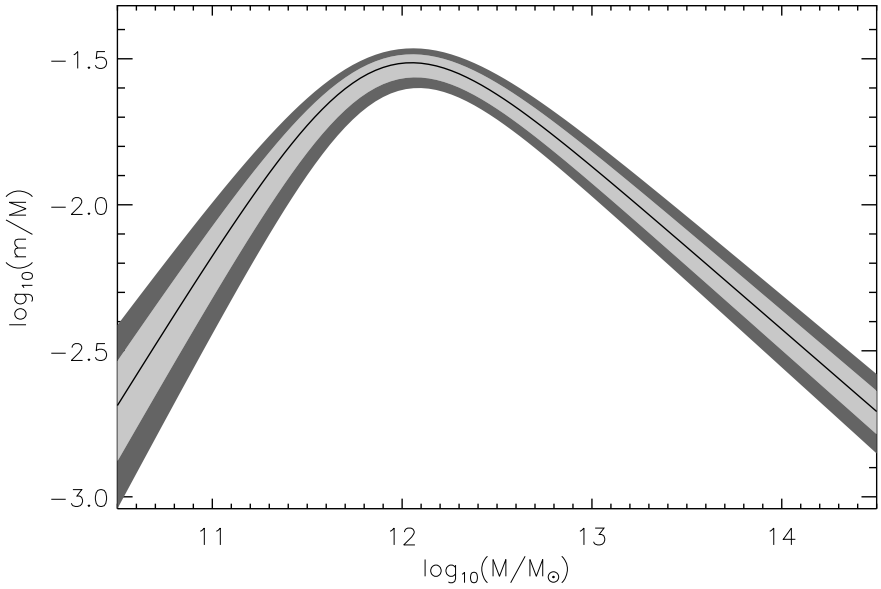

Figure 1.3: *Derived relation between stellar mass "m" and halo mass "M" (stellar mass-halo mass relation; SHM relation). The light shaded area shows the 1σ region while the dark and light shaded areas together show the 2σ region. As explained in the text, lower mass halos are thought to be (relatively) inefficient due to supernova feedback, while higher mass halos are thought to have effective AGN feedback (Figure 4 from Moster et al. 2010).*

from intense events such as supernovae can heat and deplete the central gas reservoirs, in some cases ejecting the gas entirely from the dark matter halo (Larson 1974; Dekel & Silk 1986). As cold gas is the primary fuel for star formation, this has the effect of halting current star formation and delaying future star formation. This process is most effective in low-mass halos, where the gravitational potential is lower, making the required escape velocity smaller. In high-mass galaxies, the mass of the central supermassive black hole (SMBH) is observed to scale with the galactic bulge mass (Häring & Rix 2004). As the radiation from the accreting black hole ionizes normal molecular clouds and destroys H2 molecules, this is an effective way to suppress star formation in the most massive, bulge-dominated galaxies. Additionally, quasar-driven winds can drive galaxy-scale outflows, moving enriched material into the intergalactic medium (IGM; Silk & Rees 1998). This highlights that simulations, in cases when observations can constrain them, are an invaluable tool to study the underlying physical processes in galaxy evolution.

Measurements in N-body simulations of collisionless (cold) dark matter particles have shown that the equilibrium configuration at the center of the halo is a steep, power-law mass-density relation or a "cusp" (Navarro et al. 1996b). Some of the first observations comparing HI rotation curves of dark matter-dominated dwarf galaxies[2] with the CDM predictions noted large discrepancies (Moore 1994; Flores & Primack 1994), specifically showing a shallower mass-density relation close to the center. While the predicted inner distribution scales like $\rho \sim r\alpha$ with $\alpha = -1$, in general the observations are more consistent with a constant density ($\alpha = 0$) in the central kiloparsec.

[2]From this point on, the term "dwarf galaxy" *ad hoc* refers to a galaxy with $M_\star \lesssim 10^9 M_\odot$.

Low-mass satellites around more massive galaxies offer a unique probe of dark matter substructure. Initial studies showed a large discrepancy between the observed number of Milky Way satellites and the number predicted from CDM models (Kauffmann et al. 1993; Klypin et al. 1999), a problem which has not gone away even as a number of ultrafaint Milky Way (e.g. Willman et al. 2005; Belokurov et al. 2006) and Andromeda (where the problem also exists, e.g. Zucker et al. 2004; Martin et al. 2006) companions have been discovered in recent years. In Boylan-Kolchin et al. (2011), simulations show that a majority of the dark matter subhalos[3] of the Milky Way, with masses of $0.2 - 4 \times 10^{10}$ $M_{\odot}$, do not contain luminous galaxies; the circular velocity of the observed satellites is too low compared to the expected circular velocities from the simulations. However, these "dark" subhalos are more massive than many of the host halos of Milky Way satellites and should therefore have been able to form stars.

These two issues (amongst several), known as the "cusp-core" problem and the "too big to fail" problem, respectively, either impugn the CDM model[4] or imply that there are important physical effects that are not properly treated in the simulations. Unfortunately it remains ambiguous as to which is the true cause. One of the fundamental issues with cosmological N-body simulations is that, while they have had many successes in a variety of applications, they do not represent the collisional baryons and the effects baryons can have on dark matter. In order to do that, the hydrodynamical fluid equations need to be solved and extra physics such as magnetic fields, radiation, particle collisions, and turbulence need to be numerically treated to produce realistic baryonic outputs, such as stars and galaxies. Sophisticated versions of such codes have been developed, utilizing the Smoothed Particle Hydrodynamics (SPH; e.g. GADGET-2: Springel 2005) or Adaptive Mesh Refinement (AMR; e.g. RAMSES: Teyssier 2002) techniques. The specific details of these methods are beyond the scope of this Thesis, but see Springel (2010) for an excellent review. These codes have triumphed in many key areas of galaxy formation and evolution on a variety of scales, from individual disk galaxies (Governato et al. 2007) to clusters of galaxies (Borgani et al. 2004), all in a fully cosmological context.

Without requiring any modification to the physics of the dark matter particles themselves, SPH and AMR simulations show that sufficiently strong baryonic feedback in galaxies can potentially address the issues. Feedback from supernovae was thought to be capable of flattening the profile by removing many of the baryons from the center (e.g. Navarro et al. 1996a), but Gnedin & Zhao (2002) demonstrated that a single event can not transfer enough energy into the dark matter particles. Multiple events, with significant gas re-accretion in between, have been shown to create the necessary profile (Read & Gilmore 2005), particularly if they occur on very short timescales (shorter than the dynamical timescale for the galaxy; Pontzen & Governato 2012). Many other simulations show similar results: Governato et al. (2012); Zolotov et al. (2012); Amorisco & Evans (2012); Teyssier et al. (2013). Likewise, baryonic feedback can reduce the central mass of the most massive dark matter subhalos, meaning the observed Milky Way satellites actually inhabit the most massive subhalos which eliminates the problem of having massive, "dark" subhalos.

[3] Subhalos are considered to have been distinct dark matter halos in the past that entered the larger halo via merging during the process of hierarchical assembly.

[4] It must be noted, however, that these problems are not predicted from first principles by the standard CDM model, but rather from analytical studies of numerical simulations that operate within the framework of the model (de Blok 2010).

1.3 Observations of Low-Mass Galaxies

While the particular paradigm of strong baryonic feedback is attractive on a theoretical level, observational evidence is the only way to confirm it and thereby vindicate the standard CDM model. It is logical, then, to study young and/or low-mass galaxies since they seem to be the ideal testbeds to address many of these issues. Locally, these galaxies are numerous and inhabit a large variety of environments (e.g. Zwicky 1957; Hodge 1971). Many of these local dwarf galaxies are close enough for us to resolve individual stars, particularly with the spatial resolution afforded by the *Hubble Space Telescope* (HST). The well-known relationship between the observed colors of a star and its luminosity (the Hertzsprung-Russell or HR diagram; Strömgren 1933) allows us to probe the various phases of stellar evolution and derive important physical parameters for the stellar systems. As outlined in Grebel (1997), distances can be obtained via variable stars with known period-luminosity relations or via the observed brightness of certain types stars of a fixed absolute magnitude, metallicities can be obtained from the length of the Horizontal Branch on the HR diagram, and ages can be obtained by the presence or lack of certain types of stars that exist in fixed age ranges. These derived quantities are direct observables.

More recently, sophisticated methods have been developed to interpret the color-magnitude diagrams (CMDs) from galaxies in order to reveal the previous history of star formation and chemical evolution, namely the star formation rate (SFR) as a function of time and metal enrichment (e.g. Tosi et al. 1989; Dolphin 2002). For example, Weisz et al. (2011) explain that their method takes the initial mass function (IMF), binary fraction, and age and metallicity bin widths to construct synthetic color magnitude diagrams of simple stellar populations (SSPs). They then take linear combinations of these populations with different star formation histories (SFHs) to create composite CMDs, which are then compared to the observed CMD for the galaxy. This process is repeated for a variety of composite CMDs in a Monte Carlo fashion until the likelihood is maximized and the "true" SFH is ascertained. They note that uncertainties in the SFHs due to precision in distance and foreground extinction (required input values) are small compared to the overall uncertainties in the best-fit SFH since both random uncertainties and systematic effects due to the stellar models can be more than an order of magnitude larger (Dolphin 2012, 2013).

The power of this "archaeological" method is clear, as the SFHs for more than 60 local galaxies have been derived in a self-consistent fashion (Weisz et al. 2011, 2014). However, the time resolution of individual star formation episodes that occurred several billion years ago is low. Therefore, while it is possible to determine that e.g. Hercules and Leo IV formed $> 90\%$ of their stellar mass prior to $11 - 12$ Gyr ago ($z \gtrsim 5$; Weisz et al. 2014), it is not possible to determine if that star formation took place in a single burst lasting 10 million years or if it took place over several hundred million years. Yet it is exactly this sort of time resolution that is required to address the issues brought up in Section 1.2. Likewise, bursts of star formation strong enough to produce the necessary baryonic feedback are not currently occuring locally (Lee et al. 2009). This could be a sign that either such a star formation process was more prevalent in the past than today or the volume probed in these studies is simply too small (the study of Lee et al. 2009, for example, extended only to a distance of 11 Mpc).

1.3.1 LOOKBACK STUDIES

The expansion of the universe and the concept of the cosmological redshift mean that observing galaxies at increasing distances opens the time domain to study, important because of the long timescales involved with individual instances of most of the astrophysical phenomena related to galaxy evolution (for example, the orbital time for a star in the Milky Way at the solar radius is ~ 240 Myr). These are thus termed "look-back" studies, relying on samples of objects (observed instantaneously) that span a range in time in order to discern evolutionary trends.

In order to study the formation of galaxies, the natural end point of "look-back" studies is to observe the first galaxies that formed. However, the practical challenges of their intrinsic faintness and distance have made this a formidable proposition. The cosmological redshift exacerbates this issue as the visible light from these galaxies is shifted to longer wavelengths: light produced at optical wavelengths ($\sim 4000 - 7000$ Å) is observed in the near-infrared (NIR) region of the electromagnetic spectrum ($\sim 10,000 - 30,000$ Å) at $1.4 \lesssim (1 + z) \lesssim 7.5$.

Following its initial discovery by Herschel (1800), progress in detecting infrared radiation was slow. Initial detections of extrasolar astronomical sources were made by Nichols (1901) and Pettit & Nicholson (1928). However, it was not until the development of sensitive detectors in the late 1980s using arrays made from HgCdTe (compared to optical charge-coupled devices which use silicon) that infrared astronomy gained widespread popularity. One of the first of this type was used in the Near Infrared Camera Multi-Object Spectrometer (NICMOS) on the HST. From that 128×128 pxiel array, we now have advanced 4096×4096 pixel arrays which offer superior sensitivity, especially at longer wavelengths, and the ability to efficiently conduct large near-IR surveys.

Observations above $z = 1$ have revolutionized our understanding of the galaxy formation process. Specifically, the redshift regime from $1 < z < 3$ is the peak of the cosmic star formation rate density where more than 60% of all star formation took place (Hopkins & Beacom 2006; Bouwens et al. 2007) and where most of the SMBH growth and AGN activity took place (Shaver et al. 1996; Boyle et al. 2000; Silverman et al. 2008). Likewise, this is the same regime where the morphological regularity seen in galaxies today emerged (Elmegreen et al. 2007; Wuyts et al. 2011). Deep, multiwavelength imaging surveys, such as the Cosmic Assembly Near-infrared Deep Extragalactic Legacy Survey (CANDELS; Koekemoer et al. 2011; Grogin et al. 2011), have been crucial in probing this important epoch. Much of this progress is a result of the near-IR capabilities of the new Wide Field Camera 3 (WFC3) on the HST, discussed further in Section 1.4.1. Infrared studies at these redshifts cover the rest-frame optical emission of galaxies, which comes primarily from long-lived stars and represents a more unbiased tracer of the total light output of galaxies: typical galaxies with restframe-UV brightness high enough to make it in to an optical-selected sample are actually part of a small and biased subset of the total galaxy population at these redshifts (Franx et al. 2003; van Dokkum et al. 2006).

Galaxies spanning a wide range of physical properties seem to follow remarkably similar evolutionary paths. Recent observations have proven the existence of a galactic "star forming main sequence" in which there is a tight, linear relationship between a galaxy's stellar mass and its current star formation rate (Noeske et al. 2007). The implication of this is that galaxy formation is a smooth process, where larger galaxies

form stars more quickly. In fact, the existence of the sequence means a galaxy's future evolution is in some sense predetermined, yet little is known about the low-mass end ($M_\star \lesssim 10^9 M_\odot$) at early times. While most galaxies form stars at a relatively constant rate, a few galaxies, however, experience massive bursts of star formation which last for only a short ($\sim 10^{7-8}$ *Myr*, Balzano 1983) period of time. During these bursts, young O- and B-type stars with masses of $M_\star \gtrsim 10\ M_\odot$ and main sequence lifetimes of ~ 10 *Myr* dominate the energy output of the galaxy and ionize the surrounding interstellar medium (ISM). This produces strong, narrow emission lines which can be readily observed spectroscopically.

1.4 Intermediate-z Dwarf Galaxies: A Hybrid Approach

As mentioned previously, understanding the nature of low-mass galaxies is of critical importance in the overall context of galaxy formation. Having "burst-like" star formation histories would alleviate some of the problems brought-up in Section 1.2, and observations at $z > 1$ would reveal the dwarfs during the epoch when they formed a majority of their stars (Weisz et al. 2011). While such high redshifts put the intrinsically-faint dwarfs very far away, thereby making them appear even fainter, the deepest near-IR surveys are now capable of detecting their stellar continua. With a strong burst of star formation comes strong nebular emission lines, which should also be detectable if bursts contribute significantly to the stellar mass buildup in dwarfs.

All of this puts the ability to directly test the paradigm of bursty, episodic star formation in dwarf galaxies in the early universe within reach. Even without spectroscopic data to detect the emission lines directly, nebular lines such as [O III] $\lambda\lambda 4959, 5007$ and Hα ($\lambda 6563$) could be strong enough to make an appreciable difference in the broad-band photometry of a low-mass galaxy. Exactly such a phenomenon was studied in van der Wel et al. (2011): many objects selected from broadband CANDELS observations have peculiar $I-J$ to $J-H$ colors. Such a spectral energy distribution (SED), which is flat in F_ν except for a strong excess in the J-band, cannot be reproduced by any continuum emission process. However, strong nebular [O III] emission at $z = 1.7$ could produce this excess, with the likely-strong Hα emission lying outside the coverage of the H-band. Indeed, slitless grism spectroscopy (described in the next section) for a subsample confirms this notion (see Figure 1.4). These galaxies, with restframe equivalent widths in excess of 500 Å, are termed Extreme Emission Line Galaxies (EELGs).

The objects are interpreted within the framework of the Starburst99 models (SB99; Leitherer et al. 1999), which make predictions for how the relative strengths of Hydrogen recombination lines (e.g. the Balmer lines of Hα, Hβ, Hγ, etc.) evolve with time in a starburst. By assuming a fixed Hβ/[O III] ratio of 1/8 (corroborated by the objects with grism spectra), the excess in the J-band can be transformed into an Hβ equivalent width (EW), which is a sensitive probe of the age of the starburst. For an SB99 model with continuous star formation, a Chabrier (2003) IMF with a high-mass cut off at 100 $M_\odot$, and metallicity 0.2 $Z_\odot$ (in agreement with the Hβ/[O III] ratio), the Hβ EWs imply that these galaxies have typical ages on the order of 10 – 20 Myr. By using the SB99-predicted V-band mass-to-light ratio and applying it to the observed H-band magnitude, which traces the restframe optical emission, a stellar mass of the burst component is derived,

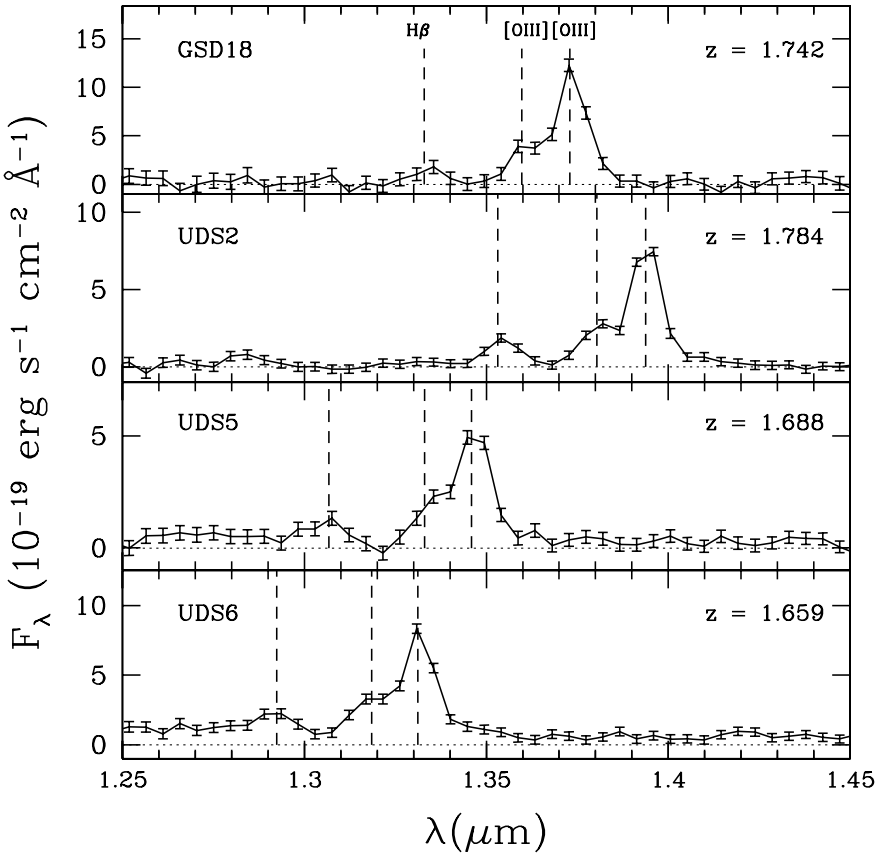

FIGURE 1.4: *WFC3 grism spectra of the four candidates with grism coverage from van der Wel et al. (2011). The IDs refer to those in Appendix A. GSD18 is object 402 from Straughn et al. (2011); the remaining three are from supernova follow-up grism observations (program ID 12099, PI: Riess). The three vertical dashed lines show positions of Hβ, [O III], and Hα for $z = 1.7$. These spectra strongly suggest that the majority of the objects in the sample are [O III] emitters at $z \sim 1.7$ (Figure 4 from van der Wel et al. 2011).*

on the order of 10^8 $M_\odot$. Such low masses in galaxies with strong nebular emission lines are similar to the rare $z \sim 0.1 - 0.3$ "green pea" galaxies of Cardamone et al. (2009) and Izotov et al. (2011), but are observed to be two orders of magnitude more common: 3.7×10^{-4} Mpc^{-3}. Other studies observe galaxies at $z > 1$ with EWs in excess of 500 Å, such as Atek et al. (2011); Shim et al. (2011); Brammer et al. (2012b); and Masters et al. (2014). This already hints that the abundance of such systems may be a strong function of time.

Such bursts are thus commonly-observed, but it is difficult to directly determine just how important these bursts are in the history of all dwarf galaxies given that these galaxies could potentially remain undetected if they were not undergoing the strong burst, even in existing deep surveys. Likewise, model predictions at these redshifts and low masses remain problematic (Guo et al. 2011). By combining the $z = 0$ stellar mass function from Guo et al. (2011) with the assumptions that the bursts last ~30 Myr and occur during the range $1 \lesssim z \lesssim 3.5$ (4 Gyr), van der Wel et al. (2011) conclude that

the descendants of these observed bursts have stellar masses (M_{desc}) of:

$$\frac{M_{desc}}{10^8 M_\odot} \sim 2.4 f_{burst}^{-1.6}, \tag{1.1}$$

where f_{burst} is the fraction of stellar mass created during such starburst events. If f_{burst} is close to one, then $M_{desc} = 1 - 2M_{burst}$; if f_{burst} is smaller, on the order of 0.5, then $M_{desc} = 2 - 3M_{burst} \sim 10^9 M_\odot$. In general, they conclude that most stars in today's dwarf galaxies formed in a small number of such bursts at $z > 1$.

1.4.1 Slitless Grism Spectroscopy

Regardless of the source, strong emission lines in the (restframe optical) spectra of galaxies are a crucial tool to study galaxies. Various emission line strengths and ratios have been empirically calibrated to indicate e.g. the star formation rates, metal contents, and ionizing sources of galaxies. Indeed, even obtaining the redshift distribution of galaxies is substantially simpler with the help of emission lines, since it is easier to discover and determine a redshift for galaxies with strong line emission than for galaxies which lack detectable line emission.

Until recently, large samples of star forming galaxies at $z > 1$ were created exclusively via color selections. These selections, such as the Lyman break (Steidel et al. 1996), BzK (Daddi et al. 2004), and BX/BM selections (Steidel et al. 2004), suffer from issues of incompleteness and contamination from lower-z interlopers, as well as preferentially selecting galaxies with certain dust properties (Ly et al. 2011). For example, the Lyman break selection requires detections in several bands redward of the actual break in the spectral energy distribution, potentially biasing against low-mass bursts with strong emission lines but little stellar continuum light (see Section 5.2.2).

All of this points towards the need for spectroscopic samples, where biases can be minimized and the selection function becomes simpler. In the context of the search for EELGs from the previous section, a complete spectroscopic sample would verify the emission line hypothesis for every object and directly test the idea that these events are common at $z > 1$ with the ability to search over a range in redshift. Since the emission lines are thought to be bright in otherwise faint continuum sources, a slitless grism spectroscopic survey is the ideal way to construct a large sample of EELGs.

Slitless grism spectroscopy involves placing a grism (a combination of a diffraction grating and a prism) in the optical path of a camera. The grism disperses the light from any incident source into multiple spectral orders on the detector, giving three-dimensional information (two spatial directions and wavelength) for every object within the field of view; see Figure 1.5. This allows for untargeted spectroscopic surveys, greatly increasing the number of spectra that can be obtained in a fixed observing time and also increasing the chance for serendipitous discoveries. Data interpretation and analysis can be difficult in crowded fields, as unrelated spectra can overlap on the detector and lead to source confusion. However, the behavior of the grism is stable and in principle the spectrum for an individual object with a known SED can be modeled *a priori* with reasonable accuracy such that overlapping spectra can be disentangled.

The ability to combine slitless grism spectroscopy with observations in the near-IR was only possible with the installation of the WFC3 on the HST; ground-based grism

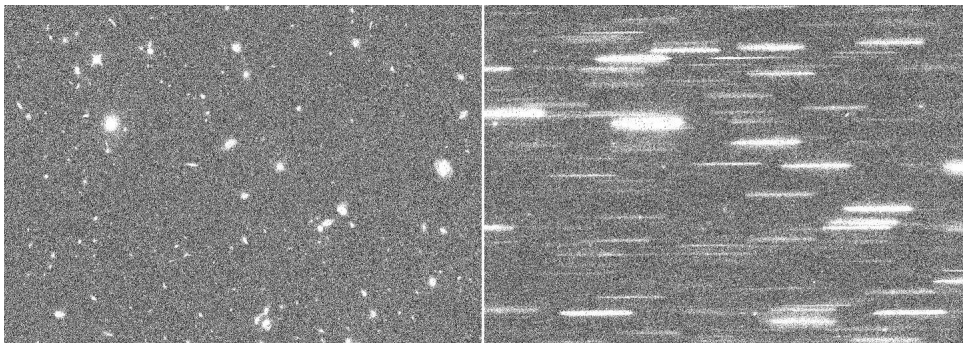

FIGURE 1.5: *(Left) HST/WFC3 near-IR image taken in the F140W band and (right) associated grism spectroscopic exposure taken with the G141 grism spanning* $\sim 1-1.7$ *µm. The slitless nature of the observations means all objects within the field of view have dispersed two-dimensional spectra. The width of the images is approximately 2′.*

surveys, which also offer inferior spatial resolution, are extremely limited in the near-IR due to the high terrestrial background level. The spectroscopic equivalent of the CANDELS survey is 3D-HST[5] (van Dokkum et al. 2011; Brammer et al. 2012a), which provides more than 600 square arcminutes of grism spectroscopy from $\sim 1 - 1.7$ *µm*. This wavelength range, using the *G141* grism, allows for coverage of strong optical emission from Hα at $0.6 \lesssim z \lesssim 1.5$ and [O III] at $1.1 \lesssim z \lesssim 2.3$, which together probe more than 5 Gyr of cosmic time. This is the ideal data set to begin to answer some of the fundamental questions about bursty star formation in low-mass galaxies.

1.5 SCOPE OF THIS THESIS

The following questions will be addressed in this Thesis:

Are these EELGs really low-mass starbursts? Yes; see Chapter 2. We isolate a sample of EELGs using a combination of 3D-HST grism data and the photometric selection of van der Wel et al. (2011) to observe in the near-IR from the ground, using LBT/LUCI1 and VLT/X-Shooter. The narrow (~ 50 km s^{-1}) emission lines imply low dynamical masses, while sophisticated SED modeling implies low stellar masses as well.

What do we know about the internal workings of these bursts? Given that the sources are barely resolved even at the resolution of the HST, we know quite a bit; see Chapter 3. For an expanded sample, ground-based near-IR spectroscopy reveals emission line ratios consistent with low-metallicity gas, plausibly created via star formation and not by AGN activity. Basic dynamical arguments point towards high gas fractions ($f_{gas} \gtrsim 2/3$) and star formation that does not deplete the entire gas reservoir, consistent with the picture that multiple bursts can occur during the lifetime of the galaxy.

How common are these events, and how have they contributed to the SFHs of all dwarf galaxies? Even more common than suggested in van der Wel et al. (2011); see Chapter 4. A systematic search for high-EW emission lines in 3D-HST reveals the evo-

[5] http://3dhst.research.yale.edu/Home.html

lution in the comoving number density of these systems, with an increased incidence at higher redshifts. The evolution with redshift mimics the evolution in the overall cosmic star formation rate density, which implies that mergers are likely not the primary trigger for the bursts.

What comes next? While the paradigm of strong outflows caused by this intense star formation episode is fully consistent with the current observations, no direct evidence has yet been discovered, but this will be tested with future work. Similarly, EELGs have a number of properties in common with very high-redshift galaxies, making them a more "local" laboratory for studying how star formation may have proceeded in the early universe. A complete sample of EELGs from 3D-HST is useful in many ways, providing a large enough number to begin to learn about their clustering (as a way of probing their halo mass) and constrain the duty cycle of the bursts.

For the remainder of this thesis, we adopt a flat ΛCDM cosmology with $\Omega_m = 0.3$ and $H_0 = 70$ km s^{-1} Mpc^{-1}, AB magnitudes (Oke 1974), Angstroms, and a Chabrier (2003) IMF, unless otherwise noted.

Chapter 2

Dynamical and Stellar Masses for Extreme Emission Line Galaxies*

Þá gengu regin öll	*Then sought the gods*
á rökstóla,	*their assembly-seats,*
ginnheilög goð,	*The holy ones,*
ok um þat gættusk,	*and council held,*
hverr skyldi dverga	*To find who should raise*
dróttir skepja,	*the race of dwarfs*
ór Brimis blóði	*Out of Brimir's blood*
ok ór Bláins leggjum.	*and the legs of Blain.*

From the epic poem Völuspá (The Prophecy of the Seeress)
Part of the Ljóþaedda, a 13^{th} century collection of Old Norse poems
Translated by Henry Adams Bellows

Spectroscopic observations from the *Large Binocular Telescope* (LBT) and the *Very Large Telescope* (VLT) reveal kinematically narrow lines (~ 50 km s^{-1}) for a sample of 14 Extreme Emission Line Galaxies at redshifts $1.4 < z < 2.3$. These measurements imply that the total dynamical masses of these systems are low ($\lesssim 3 \times 10^9$ $M_\odot$). Their large [O III] λ5007 equivalent widths (500 – 1100 Å) and faint blue continuum emission imply young ages of 10 – 100 Myr and stellar masses of 10^8 – 10^9 $M_\odot$, confirming the presence of a violent starburst. The dynamical masses represent the first such determinations for low-mass galaxies at $z > 1$. The stellar mass formed in this vigorous starburst phase

*Based on Maseda et al. (2013): "Confirmation of Small Dynamical and Stellar Masses for Extreme Emission Line Galaxies at z ~ 2," ApJ, 778, 22L.

represents a large fraction of the total (dynamical) mass, without a significantly massive underlying population of older stars. The occurrence of such intense events in shallow potentials strongly suggests that supernova-driven winds must be of critical importance in the subsequent evolution of these systems.

2.1 CONTEXT

Without further information, the dwarf interpretation of EELGs galaxies in van der Wel et al. (2011) is merely plausible. More massive populations of older stars could easily be outshone by the young starbursts: an old stellar population can have mass-to-light ratios (M/L) up to 50 times larger than those of the bursts in the near-IR, so the main uncertainty in the interpretation of the observations hinges on the determination of the total masses of these systems. Additionally, the presence of strong emission lines can hinder attempts to determine the stellar mass content, as standard SED-fitting codes do not contain emission line contributions. Hence we do not yet understand the role of this mode of star formation in the broader context of galaxy formation. When these bursts occur in truly low-mass galaxies ($\sim 10^8\ M_\odot$), the EELGs may represent the main formation mode of present-day dwarf galaxies, as argued by van der Wel et al. (2011). Alternatively, if these bursts are embedded in more massive systems ($\gtrsim 10^9\ M_\odot$), we may be witnessing the early formation stage of Milky Way-type galaxies.

Accurate mass estimates are key in addressing this issue, particularly dynamical masses. For this purpose we now present near-infrared spectroscopy of 14 EELGs at redshifts $1.4 < z < 2.3$ with [O III] λ5007 equivalent widths > 500 Å from the LBT and the VLT. These are the first dynamical mass measurements of such low-mass, high-redshift galaxies, and we also derive accurate stellar mass estimates through stringent modeling of the continuum and emission line measurements from CANDELS multi-wavelength photometry and low-resolution grism spectroscopy from the 3D-HST survey.

The remainder of this Chapter is organized as follows. In Section 2.2 we present our initial sample of EELGs for ground-based observations, in Section 2.3 we determine stellar and dynamical masses for the EELGs, and in Section 2.4 we discuss the implications of the results.

2.2 CANDIDATE SELECTION AND OBSERVATIONS

We select a sample of 17 objects with restframe equivalent widths > 500 Å in [O III] λ5007: five are from the photometrically-selected sample of van der Wel et al. (2011) in the UDS and GOODS-S fields, and the 12 remaining objects were selected based on their 3D-HST grism spectra in the UDS, GOODS-S, and COSMOS fields. One object, *COSMOS-10320*, although fulfilling the criteria, exhibits broad and asymmetric [O III] (and also Hα) of 240±10 $\mathrm{km\,s^{-1}}$. As this object is an obvious outlier (with a potential AGN contribution), we exclude it from the subsequent analysis and focus on the remaining 16 objects. Although the targets are very faint in the continuum ($m_{F140,AB} \gtrsim 24$), the emission lines are strong, with fluxes > 10^{-17} $\mathrm{erg\,s^{-1}\,cm^{-2}\,\AA^{-1}}$, making emission line detections possible with ∼1 hour integrations on 8m-class telescopes. We observe five

objects using long-slit observations with the X-Shooter wide-band spectrograph (Vernet et al. 2011) at the VLT from August to December 2012 (one slit contained two objects), focusing here on the combined $YJHK$ NIR region (1024–2480 nm with resolution $R \sim 5000$), although it simultaneously observes in the UV-Blue and the Visible regions. Four had 40 minute integrations, while one object was observed for a total of 120 minutes in the near-IR over the course of two nights. The remaining objects in the sample were observed using the LUCI1 multi-object spectrograph (Seifert et al. 2003) at the LBT with four separate masks between April 2012 and March 2013 in the J-, H-, and/or K-band (depending on the redshift, as we targeted [O III] and/or Hα) with resolution $R = 6000 - 8000$ for a minimum of 45 minutes per band. Two objects in the total LUCI1 sample had *a priori* equivalent widths greater than 500 Å, but severe contamination from OH skylines at the predicted position of the lines prevents a line extraction and they are not included in this sample. In total, five objects were detected in both Hα and [O III], one was detected only in Hα, and eight were detected only in [O III]. The faintest detected line in the X-Shooter (LUCI1) sample is 7.4 (6.0) $\times 10^{-17}$ erg s^{-1} cm^{-2} Å^{-1} with signal-to-noise of 42 (2). For all observations, seeing was better than 1″ and typically between 0.3″ and 0.8″. All exposures were dithered by 3″ to decrease dependence on the pixel-to-pixel detector variations and defects.

Reduction of the X-Shooter data is performed using version 2.0.0 of the ESO XSHOOTER pipeline[1], which provides merged, 2D near-IR spectra. Reduction of the LUCI1 data is performed using a custom pipeline, with the wavelength calibration done using the OH skylines and based on the `XIDL` routines[2]. For the brightest emission lines, we also use `XIDL` for the final sky subtraction, which uses a spline-fitting algorithm to measure and remove the skylines. See Section 3.2.2.1 for more details.

Identified emission lines in the 1D spectra are fit with Gaussian functions, where all lines in a subregion of the spectrum (i.e. [O III] $\lambda\lambda$4959,5007 and Hβ) are forced to have the same width and only the ratio of the two [O III] components is fixed to 2.98 (Storey & Zeippen 2000). When both [O III] and Hα are observed for a single object, we take the width of the higher-S/N line complex to be the "true" width, which is [O III] for this entire sample. The two line widths are always consistent within 1σ. A full description of the data reduction is deferred to Section 3.2.

Extracted emission lines are shown in Figures 2.1 and 2.2. The sample has a median line width of 48 km s^{-1} with an average uncertainty of 8 km s^{-1}, after correcting for seeing and instrumental broadening which is typically $\lesssim 20\%$ of the intrinsic line width.

[1] http://www.eso.org/sci/software/pipelines/xshooter/xsh-pipe-recipes.html
[2] http://www.ucolick.org/~xavier/IDL/

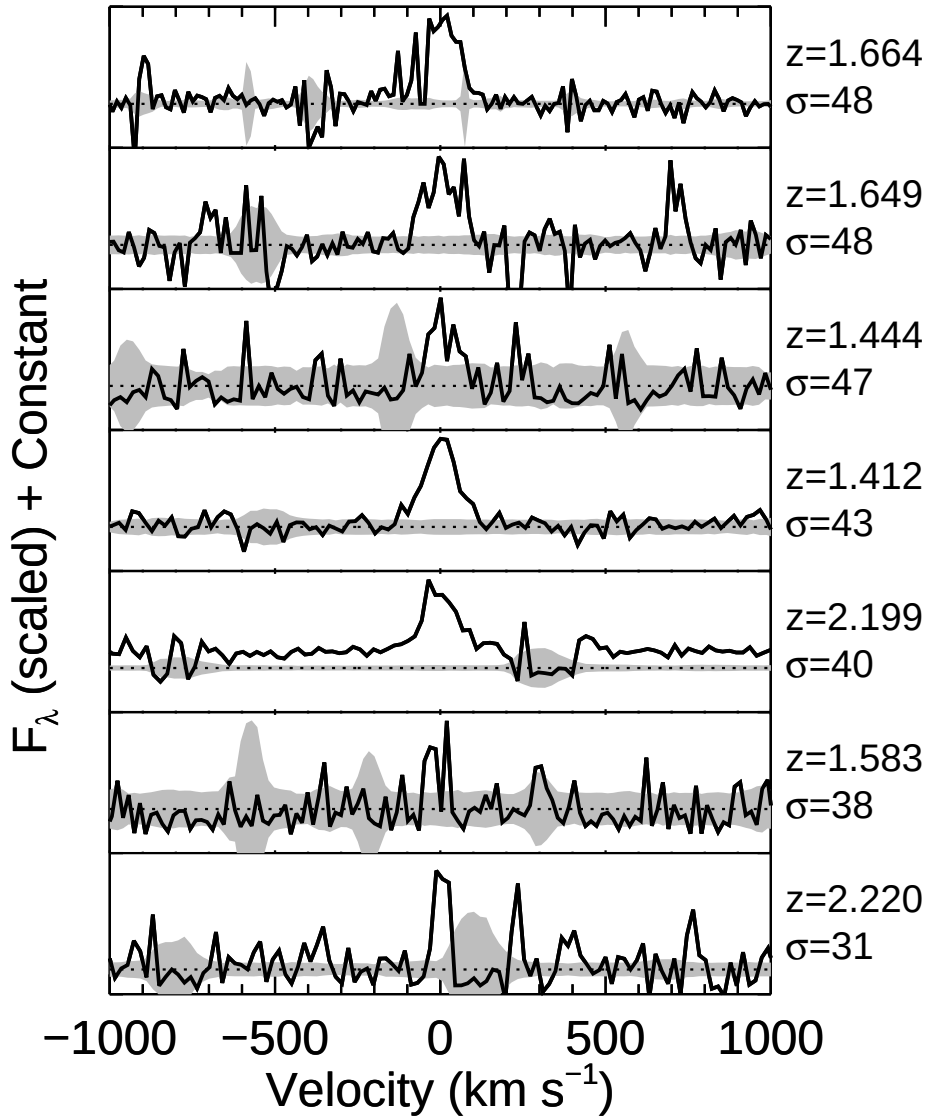

FIGURE 2.1: *Plot of the [O III] λ5007 emission line for each object, scaled to the peak flux value. Gray regions show the +/- 1-σ flux uncertainties. Typical uncertainties are smaller than 10^{-4} in redshift and ∼8* km s^{-1} *in σ.*

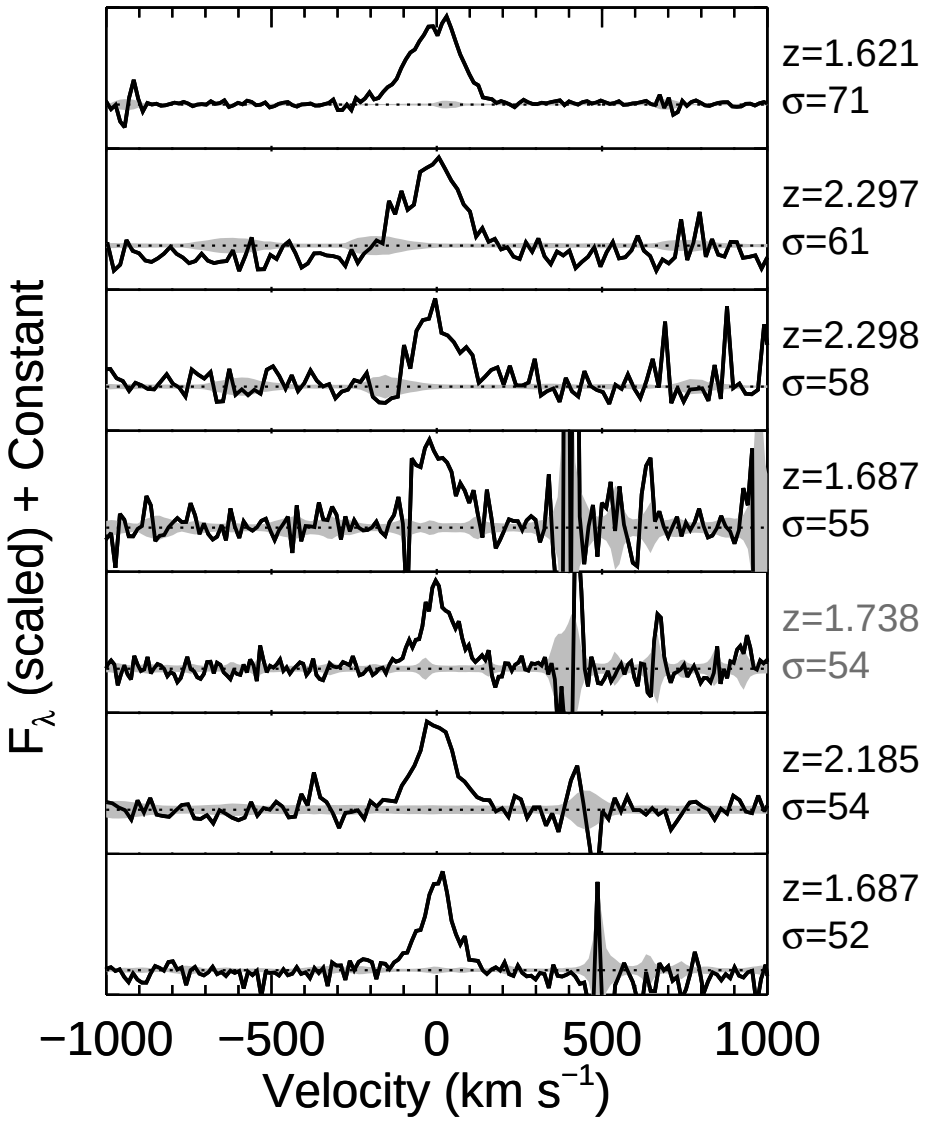

Figure 2.2: *Same as Figure 2.1 for the remainder of the sample. The single object with gray labels denotes Hα.*

2.3 DYNAMICAL AND STELLAR MASSES

2.3.1 DYNAMICAL MASS MEASUREMENTS

The velocity dispersions derived above can be used to estimate the dynamical masses according to:

$$M_{dyn} = C\frac{r_{\rm eff}\sigma^2}{G}. \quad (2.1)$$

Here, we have adopted the half-light radius $r_{\rm eff}$ as the virial radius. We take $r_{\rm eff}$ as the half-light radius from van der Wel et al. (2012), who provide size measurements from the F125W and F160W HST/WFC3 CANDELS imaging. We choose the filter that does not contain the [O III] emission line to ensure that the size is measured from the continuum light as much as possible. In cases where Hα is in F160W and [O III] is in F125W, we use the F160W size as [O III] is brighter and therefore may affect the broadband flux more. For objects in which the only line is [O III] in F125W, van der Wel et al. (2011) note that the sizes measured in both bands are still consistent. The typical $r_{\rm eff}$ is 1 kpc, which is larger than the half width at half maximum (HWHM) of the point spread function (PSF), so these sources are indeed resolved. As noted in Weiner et al. (2006), kinematic estimates using line widths yields a variety of results: Rix et al. (1997) calculate $C = 2.8$ for inclined rotating disks, while Barton & van Zee (2001) calculate $C = 2.1$ for blue compact dwarfs; Erb et al. (2006) use a simple geometric correction to obtain $C = 3.4$. Here we adopt $C = 3$, with a conservative uncertainty of 33%, as in Rix et al. (1997). Note that this value of C would be the same if we assume that these systems are spherical. We find that the 14 EELGs have $\log(M_{dyn}/M_\odot)$ ranging from 8.7 to 9.7, with a median of 9.1 and an average uncertainty of 0.3.

There are several potential systematic effects that may affect these estimates. First, for these systems the measured half-light radius is not necessarily equal to the virial radius. Indeed, some have irregular morphologies that are not well fit by single-component profiles. Second, these systems likely have an irregular dynamical structure and may not be virialized.

2.3.2 STELLAR MASS MEASUREMENTS

With confirmed redshifts, measured EWs of multiple lines, and multi-wavelength photometry, we are now in a position to estimate the stellar masses and improve upon the photometry-only method of van der Wel et al. (2011). We take 0.3–2.2 μm photometry for the two objects in the GOODS-S field from Guo et al. (2013) and the six objects in the UDS field from Galametz et al. (2013). Visual inspection of the *Spitzer Space Telescope* IRAC Ch. 1/2 images reveal that eight out of 14 objects have bright neighboring objects that contaminate the flux measurements. For consistency we perform our analysis without IRAC flux measurements for any of the objects, but we note that for those with uncontaminated IRAC fluxes, our modeling results (see below) do not change significantly. That is, the available IRAC fluxes do not reveal an underlying, older population of stars. No such multi-wavelength photometry was available at the time of this publication (November 2013) for the six objects in the COSMOS field. For these objects we

Table 2.1. Summary of Near-IR Observations and Masses

ID	RA (deg)	Dec (deg)	Instrument	z_{spec}	EW$_{[OIII],5007}$ (Å)	$\sigma_{[OIII]}$ (km s^{-1})	M_{dyn} ($M_\odot$)	$M_\star$(MAGPHYS) ($M_\odot$)
COSMOS-15144	150.156769	2.360800	LUCI1	1.412	1130±247	43.3±8.9	9.11±0.34	$8.10^{+0.20}_{-0.26}$
COSMOS-13848	150.176987	2.345390	LUCI1	1.444	888±351	46.7±14.4	9.22±0.40	$8.58^{+0.14}_{-0.22}$
COSMOS-12807	150.159546	2.333301	LUCI1	1.583	628±152	38.2±10.0	8.88±0.37	$7.95^{+0.18}_{-0.24}$
UDS-7444	34.473888	-5.234233	X-SHOOTER	1.621	713±42	71.1±5.7	9.66±0.33	$8.78^{+0.07}_{-0.16}$
COSMOS-16207	150.183090	2.372948	LUCI1	1.649	536±20	47.7±9.5	9.40±0.34	$8.43^{+0.17}_{-0.12}$
UDS-3760	34.428570	-5.255318	X-SHOOTER	1.664	731±86	48.2±5.9	9.04±0.31	$7.98^{+0.11}_{-0.09}$
UDS-3646	34.426483	-5.255770	X-SHOOTER	1.687	701±95	54.7±6.1	9.47±0.33	$8.51^{+0.12}_{-0.13}$
GOODS-S-17892	53.171936	-27.759146	X-SHOOTER	1.687	693±47	52.3±5.7	9.05±0.30	$8.95^{+0.10}_{-0.11}$
GOODS-S-26816	53.071293	-27.705803	X-SHOOTER	1.738	861±66	54.4±4.5[a]	8.86±0.31	$8.53^{+0.09}_{-0.11}$
UDS-11484	34.431400	-5.212120	LUCI1	2.185	723±95	54.2±9.4	9.35±0.34	8.97^{+0}_{-0}
COSMOS-11212	150.124237	2.313672	LUCI1	2.199	598±189	40.3±8.9	8.78±0.36	$8.77^{+0.23}_{-0.26}$
COSMOS-8991	150.095352	2.287247	LUCI1	2.220	714±85	30.9±9.0	8.65±0.40	$9.05^{+0.21}_{-0.27}$
UDS-14655	34.391373	-5.195310	LUCI1	2.297	503±34	61.0±10.8	9.67±0.33	$9.37^{+0.11}_{-0.31}$
UDS-4501	34.390755	-5.250803	LUCI1	2.298	803±162	57.8±9.7	9.07±0.33	$8.32^{+0}_{-0.19}$

Note. — All IDs refer to the CANDELS catalog for that particular field (COSMOS, UDS, or GOODS-S), all equivalent widths are quoted in the restframe, and all masses are log quantities.

[a] Hα width.

use CANDELS 4-band HST photometry (F606W, F814W, F125W, and F160W).

Here we fit the broadband spectral energy distributions, including line fluxes measured from 3D-HST grism spectroscopy, of our galaxies using a custom version of the MAGPHYS code[3] (da Cunha et al. 2008) that includes nebular emission computed using the Pacifici et al. (2012) model (Pacifici et al. 2015). The stellar emission is computed using the latest version of the Bruzual & Charlot (2003) models using a Chabrier (2003) IMF, and the attenuation by dust is accounted for using the two-component prescription of Charlot & Fall (2000). The nebular emission is computed using the CLOUDY photoionization code (Ferland 1996), as described in Charlot & Longhetti (2001); Pacifici et al. (2012). MAGPHYS uses a Bayesian approach to compare the measured photometry of observed galaxies with an extensive library of 100,000 spectral energy distribution models spanning a wide range in star formation histories, ages, and metallicities. The standard MAGPHYS priors (calibrated using more massive galaxies at low redshift) are not optimized for this specific population of young ages and low metallicities, so we have modified the standard priors to include a larger fraction of low metallicities (between 0.025 and 1 $Z_\odot$), and younger ages by allowing both rising and declining star formation histories, all with superimposed random bursts of star formation. This method results in stellar masses in the range $\log(M/M_\odot) = 8.0 - 9.4$, which are listed in Table 2.1.

van der Wel et al. (2011) estimated stellar masses based on photometry alone, making simplistic assumptions for the star formation history, emission line properties, and the metallicity. In Figure 2.3 we compare our stellar mass estimates with those estimated using the photometric method. Our values are 1.1 times larger (median) with a scatter of 0.20 dex, consistent with no systematic offset. The MAGPHYS modeling results reinforce the notion that these galaxies are dominated, in terms of stellar mass, by a very young stellar population. While the MAGPHYS modeling uses much more information, the crucial elements in both mass estimates are the blue continuum and the strong emission lines, which strongly constrain any modeling approach.

Figure 2.4 compares the MAGPHYS stellar mass estimates with the dynamical es-

[3] http://www.iap.fr/magphys/magphys/MAGPHYS.html

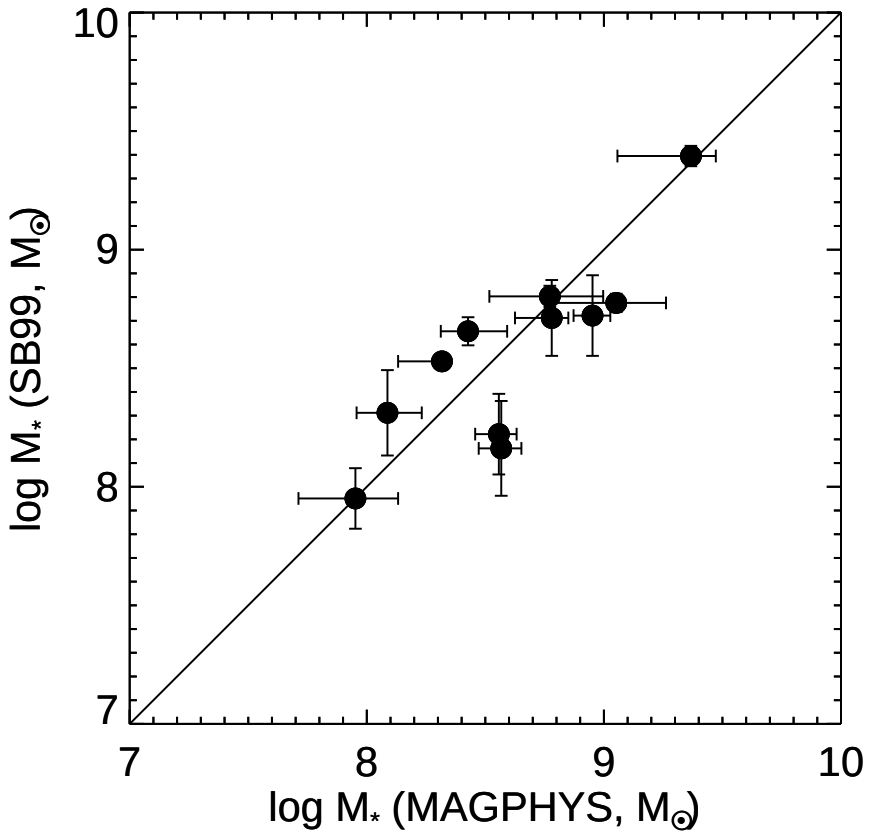

FIGURE 2.3: *Comparison of* `MAGPHYS`*- and* `SB99`*-derived stellar masses for our sample.* `SB99` *utilizes the equivalent width of Hβ (determined from photometry alone) to calculate the masses, while* `MAGPHYS` *utilizes the full photometric SED and the emission line fluxes.*

timates. $\log(M_{dyn}/M_{\star})$ = 0.57 (27% of the total mass is in stars) ± 0.21 (random) ± 0.34 (systematic) for the sample where the 0.34 dex systematic uncertainty is from the dynamical mass (see Section 2). The 0.21 dex random uncertainty contains the contributions from the measurement uncertainties and the limited sample size. The three points closest to the $M_{dyn} = M_{\star}$ line illustrate the challenges to any modeling approach. Two of them are the only $z \sim 2.2$ galaxies from the COSMOS sample, where the 4-band CANDELS photometry does not sample any continuum redward of [O III] (one of which is also severely contaminated by an OH skyline, making our line dispersion estimate more of a lower limit), and the third is an object with two distinct components in the WFC3 imaging, where the assumptions contained in the dynamical mass estimate may not accurately reflect the true conditions in the system.

The low dynamical masses confirm the low-mass nature of these systems directly and exclude the presence of large amounts of unseen stars, gas, dust, or dark matter that exceed the observed amount of stellar matter by more than a factor of five. Our implied maximal gas fractions do not exceed those for more massive galaxies at similar redshifts, which range from $\sim 30-80\%$ (Daddi et al. 2010b; Tacconi et al. 2013). As seen in Figure 2.4, our galaxies have similar $M_{dyn}/M_{\star}$ ratios to the starforming sample of Erb et al. (2006), albeit with EWs (and hence specific star formation rates) that are a factor of four higher.

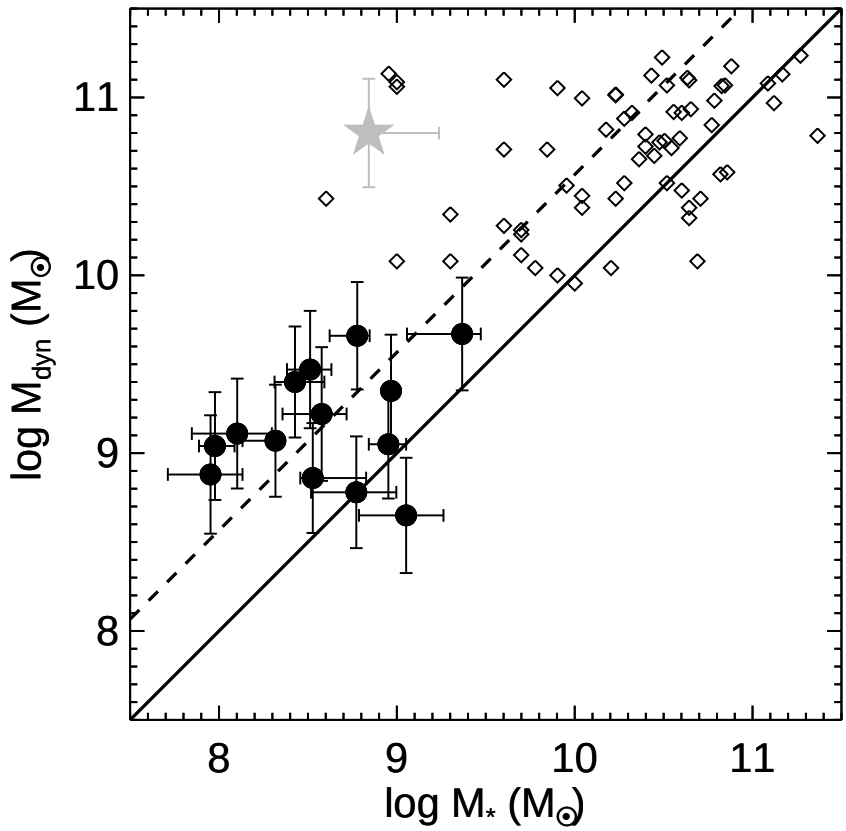

Figure 2.4: *Dynamical masses determined from the velocity width of the emission lines versus stellar masses from the MAGPHYS SED fits to the full optical/near-IR SEDs for our equivalent width-selected sample. The dashed line shows the average value of 27.1% of the total dynamical mass made up by stars. The gray point is COSMOS-10320, which is not considered in the analysis. Open diamonds are from Erb et al. (2006) for star-forming galaxies at $z \sim 2$. Although the M_{dyn} values were derived in different manners (see Sec 2.3.1), the relationship between M_{dyn} and $M_\star$ is similar for the two samples.*

2.4 Concluding Remarks

In this Chapter, we show kinematic line widths in the range $30 - 70$ km s^{-1} for a sample of 14 EELGs (with EW $>$ 500 Å) at redshifts $1.4 < z < 2.3$. This constitutes the first direct mass measurements for such galaxies at these epochs, with total masses $\sim 10^{9.1}$ $M_\odot$. SED modeling results in stellar masses $\sim 10^{8.5}$ $M_\odot$, ruling-out the presence of an evolved, massive stellar population. Therefore, we conclude that these nascent galaxies are undergoing intense starbursts, and the stars produced in the single burst contribute substantially to their total mass budget. This confirms that the abundant population of EELGs at $z > 1$ demonstrate a common starburst phase among low-mass galaxies at these epochs, the intensity of which has only recently been reproduced by hydrodynamical simulations Shen et al. (2014). While the contribution of such strong starbursts to the growth in stellar mass over cosmic time depends on their duty cycle, which is so far unconstrained observationally, their ubiquitous nature at these redshifts van der Wel et al. (2011) points towards the brief starburst phase as important in the mass build-up of most (if not all) dwarf galaxies.

Given the intensity of the starbursts and the shallow potential wells in which they occur, supernova-driven winds likely dominate the star formation history and subsequent evolution of these systems, as described in Section 1.2. Our current data set does not allow us to make stronger conclusions about the presence of feedback and winds via asymmetric or separate broad/narrow components in individual galaxies. However, with future spectroscopic studies of these objects, we will be able to search for such signals in stacked spectra.

In the present-day universe, such extreme starbursts are very rare (e.g. Cardamone et al. 2009), but at early epochs ($z > 4 - 6$) such events may well be the rule rather than the exception. It is becoming increasingly clear that strong emission lines affect the search for and interpretation of high-z galaxies. Strong emission line galaxies at moderate redshifts ($z \sim 2$) can masquerade as drop-out selected $z > 8$ candidates (see discussion in e.g., Atek et al. 2011; Coe et al. 2013; Bouwens et al. 2013; Ellis et al. 2013; Brammer et al. 2013). Furthermore, for true high-redshift galaxies these strong emission lines are likely omnipresent (Smit et al. 2014) and affect the broad-band SED, so they should therefore be included in the modeling as described here in Section 2.3.2 (also see Curtis-Lake et al. 2013; Schaerer et al. 2013). However, the results presented here are encouraging. We suggest that if strong emission lines are evident, then it is likely that the total stellar mass does not greatly exceed the mass of the young stellar population traced by the blue continuum.

Chapter 3

Kinematics and Metallicites of Extreme Emission Line Galaxies*

Bietet einerseits die Spektralanalyse, wie wir im Vorstehenden gezeigt zu haben glauben, ein Mittel von bewunderungswürdiger Einfachheit dar, die kleinsten Spuren gewisser Elemente in irdischen Körpern zu entdecken, so eröffnet sie andererseits der chemischen Forschung ein bisher völlig verschlossenes Gebiet, das weit über die Grenzen der Erde, ja selbst unseres Sonnensystems, hinausreicht.

G. Kirchhoff & R. Bunsen
Annalen der Physik und Chemie, Bd. 110 No. 6, 1860, S. 161–189

We present near-infrared spectroscopy of a sample of 22 Extreme Emission Line Galaxies at redshifts $1.3 < z < 2.3$, confirming that these are low-mass ($M_\star = 10^8 - 10^9 M_\odot$) galaxies undergoing intense starburst episodes ($M_\star/SFR \sim 10 - 100$ Myr). The sample is selected by [O III] or $H\alpha$ emission line flux and equivalent width using near-infrared grism spectroscopy from the 3D-HST survey. High-resolution NIR spectroscopy is obtained with LBT/LUCI1 and VLT/X-Shooter. The [O III]/$H\beta$ line ratio is high ($\gtrsim 5$) and [N II]/Hα is always significantly below unity, which suggests a low gas-phase metallicity. We are able to determine gas-phase metallicities for 7 of our objects using various strong-line methods, with values in the range $0.05 - 0.30\ Z_\odot$ and with a median of $0.15\ Z_\odot$; for three of these objects we detect [O III] λ4363 which allows for a direct constraint on the metallicity. The velocity dispersion, as measured from the nebular emission lines, is typically $\sim 50\ \mathrm{km\,s^{-1}}$. Combined with the observed star-forming activity, the Jeans and Toomre stability criteria imply that the gas fraction must

*Based on Maseda et al. (2014): "The Nature Of Extreme Emission Line Galaxies At $z = 1 - 2$: Kinematics And Metallicities From Near-Infrared Spectroscopy," ApJ, 791, 17.

be large ($f_{gas} \gtrsim 2/3$), consistent with the difference between our dynamical and stellar mass estimates. The implied gas depletion time scale (several hundred Myr) is substantially longer than the inferred mass-weighted ages (~50 Myr), which further supports the emerging picture that most stars in low-mass galaxies form in short, intense bursts of star formation.

3.1 CONTEXT

While we see that starbursts do not play an important role in the global star-formation at the present epoch (Lee et al. 2009), it is likely that the star formation histories of dwarf galaxies are complex and varied (Mateo 1998) and that their typical star-formation rates were higher in the past (e.g. Gallagher et al. 1984). That star formation in low-mass galaxies may be very burst-like is predicted by hydrodynamical simulations (e.g., Pelupessy et al. 2004; Stinson et al. 2007; Shen et al. 2014). The theoretical picture, in general, appears to be that star formation is regulated by stellar feedback in the form of supernovae and winds that heat and deplete the central reservoirs of cold gas required for continued star formation. In simulations of lower mass systems, feedback is predicted to eject gas out of the galaxy and into the halo, resulting in an episodic star formation history across the entire galaxy (Stinson et al. 2007).

In addition to the initial work by van der Wel et al. (2011), Straughn et al. (2011), and Atek et al. (2011), other objects with similarly low masses and metallicities at $z > 1$ have been discovered in Brammer et al. (2012b; $EW_{[OIII],rest}$=1499 Å) and van der Wel et al. (2013; $EW_{[OIII],rest}$=1200 Å) assisted by strong gravitational lensing, in Masters et al. (2014; $EW_{[OIII],rest}$=154 Å), in Erb et al. (2010; $EW_{[OIII],rest}$=285 Å), and in Chapter 2. All of these objects are emission-line dominated systems with low metallicities and high equivalent widths, the so-called EELGs.

These systems are likely the high-EW tail of the distribution of high-redshift dwarf galaxies, and resemble the class of blue compact dwarf galaxies (BCDs, Sargent & Searle 1970) observed locally in several ways: low masses, high SFRs relative to their mass, and strong emission lines. However, the EELGs are indeed "extreme," with sSFR values an order of magnitude higher than the BCDs, similar to the strong [O III] emitters ("green peas") discovered photometrically in the SDSS by Cardamone et al. (2009), as well as spectroscopically by Amorín et al. (2010) and Izotov et al. (2011). As suggested by those authors, the star-formation mode exhibited in the "green peas" is likely a relic of a mode that was much more prevalent in the earlier universe.

The implication of strong emission lines and an extremely faint continuum are that these systems have low masses and are undergoing an intense burst of star formation. Equivalent widths > 100 Å and stellar masses of $10^8 - 10^9\ M_\odot$ imply specific star formation rates (sSFR) in excess of 10 Gyr^{-1}, which is more than an order of magnitude higher than star-forming systems of equivalent masses at lower redshifts (Karim et al. 2011). These low stellar and dynamical masses are confirmed in Chapter 2, who also rule-out significant contributions to the total mass from older stellar populations for objects with restframe [O III] λ5007 equivalent widths > 500 Å and intimate that the bursts are intense and have low metallicities. The implied star formation rates and masses have only been reproduced recently in hydrodynamical simulations (e.g. in Shen et al. 2014).

Although these previous observational studies have placed constraints on various quantities, many uncertainties remain. In the case of Chapter 2 and van der Wel et al. (2011), all of the observed [O III], Hβ, and Hα emission is attributed to star formation and not AGN. In van der Wel et al. (2011), upper-limits are placed on the black hole masses from the UV-continuum slopes, but their starbursting nature is merely plausible given the lack of knowledge about low-metallicity AGN (Izotov & Thuan 2008; Kewley et al. 2013). Low metallicities are simply inferred from the consistency of the SED fits using low-Z (0.2 $Z_{\odot}$) templates with the observed photometry.

Some issues still remain in our understanding of such systems, such as stringent limits to the low masses and metallicities, including those with EWs < 500 Å, and the starburst origin of their strong emission lines. Here we combine both high- and low-resolution near-IR spectroscopy with broadband photometry. With the low-resolution spectra, we select candidates for follow-up high-resolution spectroscopy and obtain emission line fluxes. The high-resolution spectra constrain various emission line ratios, some of which are useful diagnostics of AGN activity, as well as line widths, which are themselves a probe of the dynamical masses of the systems. This provides strong evidence for their low masses and low metallicities, as well as confirming their starbursting nature. Sophisticated modeling of the broadband SEDs constrains the stellar masses and ages, as well as providing information on the dust content and metallicities. Together, this tells us about the strength and duration of the star-forming event.

The remainder of this Chapter is organized as follows. In Section 3.2 we describe the near-infrared spectroscopy and multi-band photometry used in the initial candidate selection process and the subsequent follow-up observations. Section 3.3 presents the results of the spectroscopic study, including emission-line widths, physical sizes, and masses. In Section 3.4 we confirm their low metallicities and rule out AGN as a significant source of contamination. Section 3.5 presents the implications of this work for the gas content of these systems, and Section 3.6 summarizes our findings and puts the results into the overall context of the formation history of dwarf galaxies.

3.2 DATA

3.2.1 CANDIDATE SELECTION

In order to search for and investigate these "starbursting dwarf galaxies," we take a multi-faceted approach similar to that presented in Section 2.2. Our preliminary search utilizes data from the 3D-HST survey, which uses the WFC3 $G141$ grism with an effective wavelength coverage of 1.1 to 1.65 μm.

The grism data allow us to select and confirm strong line emitters spectroscopically. Photometric cuts, such as the iJH cut of van der Wel et al. (2011) and a similar $ViJH$ selection (excess in H compared to a blue continuum, all from CANDELS), are used to preselect objects with strong features in their SEDs. The $G141$ grism data are reduced according to Brammer et al. (2012a) for the UDS, GOODS-S, and COSMOS fields, and are then used to confirm bright lines with little or no associated continuum. While we find numerous examples of these objects at $z > 1$ (see Chapter 4), we focus here on objects where the emission lines do not fall in the wavelength range between the J-,

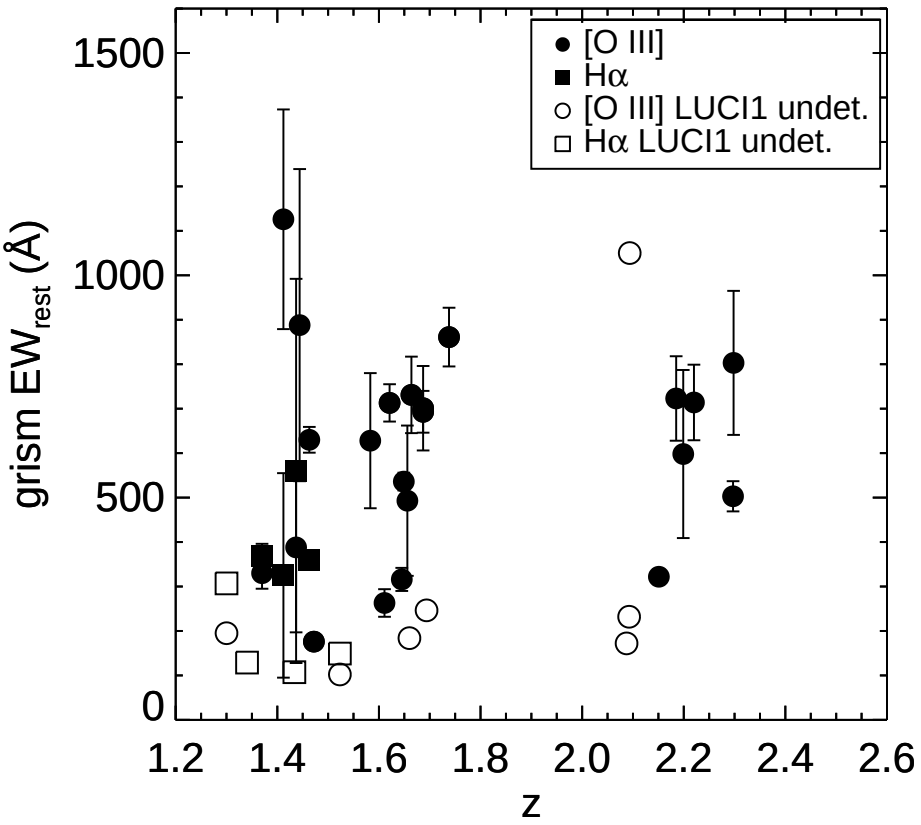

FIGURE 3.1: *Restframe equivalent widths as a function of redshift for our entire sample. Circles represent equivalent widths from [O III]$_{5007}$ and squares represent equivalent widths from Hα. The equivalent widths were determined from photometry and grism spectroscopy, see Section 3.2.1. For objects in which both [O III] and Hα are visible in the grism spectrum, both equivalent widths are plotted. Open symbols show objects without LUCI1 line detections, due to intrinsic faintness or skyline contamination. Our emission-line detection rate is close to 100% for objects with EW > 300 Å.*

H-, and *K*-bands, enhancing the chances for detectability from the ground. The low-resolution WFC3 grism data ($R \sim 130$) provide redshift information such that targets can be selected with [O III] in the redshift range $1.15 < z < 2.40$ and Hα in the redshift range $0.64 < z < 1.59$ to $\delta z/z \sim 0.005$. However, our photometric preselection relies on flux excesses such that we mostly see objects at $1.3 \lesssim z \lesssim 1.8$ and $2.1 \lesssim z \lesssim 2.3$. Note that we do not resolve the continuum in our ground-based observations (discussed presently), so all EW values are calculated from the grism spectra directly. In total, we select 31 objects for ground-based spectroscopic observations using this method. An additional five candidates are taken from the sample of van der Wel et al. (2011) and one from Straughn et al. (2011). Their equivalent widths as a function of redshift are shown in Figure 3.1. Non-detections are due to either intrinsic faintness in the lines (we are sensitive to line flux in our ground-based spectra, not EW) or contamination from OH-skylines.

3.2.2 LBT/LUCI1 SPECTROSCOPY

We observe a subset of our grism-selected sample with the LUCI1 multi-object spectrograph (Seifert et al. 2003) on the 8.4 m LBT. We use LUCI1 in multi-object mode, splitting our 31 candidates between four masks, during April 2012 (two masks in the COSMOS field), October 2012 (one mask in the UDS field), and March 2013 (an additional mask in the COSMOS field). Approximately two hours are spent observing in each of the J- and H-bands for the first two COSMOS masks (A and B) using 1″ slits, two hours in each of the H- and K-bands for the UDS mask (C) with 0.6″ slits, and three total hours on the final COSMOS mask (D) in the J- and H-bands using 0.6″ slits. All data are taken using the high-resolution 210_$zJHK$ grating ($R_J = 8460, R_H = 7838, R_K = 6687$). The exposures are dithered by 3″ and are of varying durations, depending on the band: J-band data using 600s exposures, H-band data with 300s exposures, and K-band data with 120s exposures. The shorter integrations in the H- and K-bands lead to lower signal-to-noise (S/N) due to additional readnoise, but are necessary so as not to saturate the detector in the regions with the brightest OH skylines. Seeing was generally good (between 0.5″ and 1″ in the optical) during the COSMOS observations, with good transparency. For the UDS observations, seeing was generally better than 1″. Table 3.1 details the observations of individual objects, including IDs (from the CANDELS catalogs, discussed in Section 3.3.1), coordinates, and the main line detections.

3.2.2.1 LUCI1 DATA REDUCTION

We first mask regions of the spectra that are affected by persistence due to the acquisition and alignment exposures. This effect is reduced with each readout, so we only mask the regions if they are 2σ higher than the background level. We then create flat-field images from lamp-illuminated exposures and remove cosmic rays using a median-stacking technique. The most important cosmetic step is the removal of bad pixels, which are identified in the lamp-illuminated exposures, and the hot pixels in the spectra, which are identified in dark exposures. Additionally, for an as-yet unknown reason, the first exposure of every series has small "halos" around the hot pixels. As such, we remove slightly larger regions around these hot pixels in the first exposure of every series. Our wavelength calibration is done using the OH skylines, with a code based on `XIDL` routines. We also use `XIDL` for the final sky subtraction, which uses a spline-fitting algorithm to measure and remove the lines. To maximize signal-to-noise (S/N), we do not use frame-frame subtraction and instead measure the sky from the individual frames, with the exception being some objects with particularly bad skyline contamination, where frame-frame subtraction better removes the skylines but adds noise to the spectrum. Dithering the exposures by 3″ ensures a decreased dependence on the pixel-to-pixel variations in the detector.

Since our objects of interest have virtually no visible continuum, one-dimensional spectral extraction must be done carefully. We must visually search for the lines in the stacked reduced spectra. Since we know the wavelengths of the brightest lines from the grism data, this exercise is straightforward. We isolate the line region according to a signal-to-noise cut, and then collapse that region in the wavelength direction to create a slice containing the spatial line profile. This profile is fit with a standard Gaussian function. The width of the distribution, σ, and the center, μ, are then used in the full spectral extraction: a Gaussian function with these same σ and μ values is fit for each pixel row

Table 3.1. Summary of Near-IR Observations

ID	RA (deg)	Dec (deg)	Mask	Observed Lines
GOODS-S-7892	53.17194	-27.75915	...	[O III], Hα
GOODS-S-43693	53.07129	-27.70580	...	Hα
GOODS-S-43928	53.05158	-27.70476	...	[O III]
UDS-6195	34.42648	-5.25577	...	[O III], Hα
UDS-6377	34.42857	-5.25532	...	[O III], Hα
UDS-7665	34.39076	-5.25080	C	[O III][a]
UDS-10138	34.42336	-5.24226	C	[O III][a]
UDS-12435	34.41087	-5.23481	C	Hα[a]
UDS-12539	34.47389	-5.23423	...	[O III], Hα
UDS-12920	34.39870	-5.23320	C	...
UDS-15319	34.40516	-5.22493	C	...
UDS-19167	34.43140	-5.21212	C	[O III]
UDS-24154	34.39137	-5.19531	C	[O III], Hα
COSMOS-8509	150.09837	2.26596	B	...
COSMOS-8700	150.09740	2.26848	B	...
COSMOS-10599	150.09535	2.28725	B	[O III]
COSMOS-11530	150.11931	2.29688	B	...
COSMOS-12102	150.09728	2.30252	B	[O III], Hα
COSMOS-13184	150.12424	2.31367	B	[O III]
COSMOS-14249	150.11011	2.32459	B	...
COSMOS-14435	150.16232	2.32602	D	...
COSMOS-15091	150.15955	2.33330	D	[O III]
COSMOS-16152	150.18762	2.34469	A	...
COSMOS-16286	150.17699	2.34539	D	[O III][b]
COSMOS-16566	150.17067	2.34830	D	[O III], Hα
COSMOS-17118	150.15114	2.35410	D	[O III]
COSMOS-17162	150.15134	2.35482	A	...
COSMOS-17295	150.18318	2.35537	D	...
COSMOS-17539	150.12814	2.35810	A	...
COSMOS-17839	150.15677	2.36080	A	[O III]
COSMOS-18299	150.17098	2.36536	A	...
COSMOS-18358	150.16719	2.36689	A	[O III]
COSMOS-18582	150.13281	2.36878	A	...
COSMOS-18777	150.18628	2.37054	A	...
COSMOS-19049	150.13886	2.37340	A	[O III][b] Hα
COSMOS-19077	150.18309	2.37295	A	[O III]
COSMOS-20589	150.18056	2.38822	D	...

Note. — All IDs refer to the CANDELS catalog for that particular field. Mask A was observed on 21 April 2012, mask B on 22 April 2012, mask C on 10 and 11 October 2012, and mask D on 12 March 2013, all at the LBT; *GOODS-S-7892* was observed on 15 December 2012, *GOODS-S-43693* on 1 October 2012, *GOODS-S-43928* on 15 October 2012, *UDS-6195* and *UDS-6377* on 27 August 2012, and *UDS-12539* on 2 and 27 August 2012 (120 minutes in the NIR), all at the VLT. Line detections are at least 1σ.

[a]Due to technical problems during the first night of observations, the total exposure time used for these line extractions is only 3600s in *H*.

[b]Only the [O III] λ5007 component.

in the spatial direction tracing a constant distance from the edge of the (curved) slit with the amplitude as the only free parameter, reflecting the electron counts at that particular wavelength. All sets of observations were reduced and analyzed separately and the resolution is incorporated into the calculation of the intrinsic line widths to remove systematics in the velocity dispersion measurements. Flux calibration is done by comparing the integrated counts from the LUCI1 spectrum to the integrated line flux from the 3D-HST grism spectrum when possible.

3.2.3 VLT/X-Shooter Spectroscopy

For an additional six sources, we obtained near-IR and visible spectra using the X-Shooter spectrograph (Vernet et al. 2011) on the 8.2 m VLT. We observed five of the objects initially found in van der Wel et al. (2011): three with previous grism-spectroscopic confirmation in Straughn et al. (2011) and Weiner et al. (in prep.), and the two remaining candidates with the largest photometrically inferred line fluxes. A sixth candidate was selected from the Straughn et al. (2011) sample. Observations were done in long-slit mode from August to December 2012 with 40 minute integrations using 1″/0.9″/0.9″ (UVB/VIS/NIR) slits and the 100k/1pt/hg/1×2 readout mode. See Table 3.1 for the targets and observing dates. The proximity of objects *UDS-6377* and *UDS-6195* allowed for them to be observed in the same slit.

Although the X-Shooter spectrograph also observes in the UV-Blue, four of our six objects were not observed during dark time, rendering the data unusable. The near-IR region of X-Shooter spans the combined $YJHK$ region from 1024−2048 nm, while the visible region spans 559.5−1024 nm. Reduction of the X-Shooter data is performed using version 2.0.0 of the ESO XSHOOTER pipeline, which provides merged, 2D near-IR and visible spectra. Extraction is performed in a similar manner to the LUCI1 data.

3.3 Dynamical and Stellar Masses

In order to confirm our hypothesis that these systems represent starbursting dwarf galaxies, we must confirm their low stellar masses, low metallicities, and high star formation rates. Stellar masses can be constrained through SED fits to broadband photometry, and metallicities can be constrained by observing emission-line ratios, such as [O III]/Hβ. Any star formation rate is contingent on the nature of the emission lines, since AGN can also produce very high excitations.

3.3.1 Methods and Results

In our near-IR spectra, the most prominent lines seen are [O III] λ5007 and Hα, along with their associated complexes ([O III] λ4959+Hβ, and [N II] $\lambda\lambda$6548,6584, respectively). With the exception of *COSMOS-12102*, the emission lines can be well-fit by a Gaussian function, as described in Section 2.2. *COSMOS-12102* has the broadest emission lines of the sample. In addition to their broadness, they display some degree of

Table 3.2. Sample of Emission Line Galaxies

ID	m_{F140W} (AB)	r_{eff}[a] (kpc)	$f_{H\alpha}$	$EW_{H\alpha}$ (Å)	$f_{[OIII]}$	$EW_{[OIII],5007}$ (Å)	z_{spec}	$\sigma_{H\alpha}$ (km s^{-1})	$\sigma_{[OIII]}$ (km s^{-1})
GOODS-S-33131	23.66±0.08	0.68±0.62	...	...	7.36±2.99	693±47	1.687	48.7±4.3	52.3±5.7
GOODS-S-43693	24.36±0.12	0.35±0.06	...	...	16.9±0.88	861±66	1.738	54.4±4.5	...
GOODS-S-43928	24.59±0.15	1.9±0.48	4.5±1.2[b]	199[b]	3.7±1.6[b]	176[b]	1.472	...	31.4±8.2
UDS-6195	24.26±0.13	1.4±0.42	...	...	...	701±95[c]	1.687	69.9±4.9	54.7±6.1
UDS-6377	24.53±0.17	0.67±0.04	...	...	...	731±86[c]	1.664	54.5±4.5	48.2±5.9
UDS-7665	25.40±0.14	0.51±0.08	...	...	13.7±2.76	803±162	2.298	...	57.8±9.7
UDS-10138	23.77±0.03	0.75±0.08	...	...	10.9±0.57	322±17	2.151	...	80.9±10.0
UDS-12435	23.42±0.03	1.0±0.06	...	...	12.2±0.94	263±31	1.611	65.2±11.3	...
UDS-12539	23.39±0.06	1.3±0.07	...	...	35.5±2.73	713±42	1.621	81.3±4.3	71.1±5.7
UDS-19167	23.99±0.04	1.1±0.20	...	...	21.5±2.82	723±95	2.185	...	54.2±9.4
UDS-24154	23.78±0.04	1.8±0.16	...	...	21.9±3.09	503±34	2.297	72.5±13.1	61.0±10.8
COSMOS-10599	24.47±0.26	0.67±0.16	...	...	11.8±0.89	714±85	2.220	...	30.9±9.0
COSMOS-12102	22.82±0.06	1.6±0.08	19.9±1.0	360±18	49.4±2.28	630±29	1.463	230.8±14.7	241.3±12.7
COSMOS-13184	23.91±0.16	0.53±0.10	...	...	11.5±2.94	598±189	2.199	...	40.3±8.9
COSMOS-15091	25.46±0.13	0.75±0.11	...	...	5.99±3.61	628±152	1.583	...	38.2±10.0
COSMOS-16286	24.64±0.11	1.1±0.13	0.39±3.32	41±345	8.76±3.46	888±351	1.444	...	46.7±14.4
COSMOS-16566	24.60±0.09	1.4±0.09	4.22±3.26	560±432	7.28±3.58	388±191	1.437	25.5±14.0	32.8±8.4
COSMOS-17118	24.16±0.13	4.8±0.33	...	...	12.3±4.22	493±169	1.656	...	46.5±8.8
COSMOS-17839	24.36±0.24	0.99±0.06	3.27±3.20	325±230	16.3±3.58	1126±247	1.412	...	43.3±8.9
COSMOS-18358	22.84±0.04	1.6±0.02	...	...	30.2±0.97	316±26	1.645	...	55.9±9.0
COSMOS-19049	22.93±0.05	2.3±0.06	16.4±1.2	368±28	20.9±2.20	330±35	1.370	81.9±50.2	122.0±11.0
COSMOS-19077	23.69±0.12	1.6±0.05	...	...	20.5±0.77	536±20	1.649	...	47.7±9.5

Note. — All fluxes are given in units of 10^{-17} erg s^{-1} cm^{-2}. Equivalent widths are quoted in the rest-frame. A description of the size measurements is given in Section 3.3.1.

[a] van der Wel et al. (2012)

[b] Straughn et al. (2011)

[c] van der Wel et al. (2011)

asymmetry and are thus not well-fit by Gaussian functions. The skewness could be caused by several processes, such as the presence of strong outflows. Such interpretations are beyond the scope of this Thesis and demand additional observations.

The best-fitting redshifts, velocity dispersions, and line ratios are given in Table 3.2.

As described in Section 2.3.1, velocity dispersions of the strong emission lines can be used to estimate the dynamical masses, assuming the line width comes entirely from gravitational motion in a virialized system such that

$$M_{dyn} = 3\frac{r_{\rm eff}\sigma^2}{G}. \tag{3.1}$$

Here, σ is the observed line width from our NIR spectrum and r_{eff} is the effective radius of the galaxy from the public CANDELS catalog released in van der Wel et al. (2012). Typical objects are 1.0±0.1 kpc in both the J_{F125W}- and H_{F160W}-bands.

These dynamical masses are listed in Table 3.3, ranging from $10^{8.39}$ to $10^{10.6}$ $M_\odot$, with a median mass of $10^{9.13}$ $M_\odot$. The uncertainty in the dynamical mass estimate comes primarily from the systematic uncertainty in the proportionality constant of 3, which relates the intrinsic velocity v to the observed velocity dispersion σ, which we assume to be the same factor of 33% as Rix et al. (1997), since in most cases our observed line widths and physical sizes are well-constrained. Further details can be found in Section 2.3.1. Amorín et al. (2012), in a study of "green peas," observe multiple star-forming regions and gas flows which is seen as asymmetries and broad, low-intensity wings. While we do not see such clear evidence for outflows via asymmetric line profiles (*COSMOS-12102* excepted) or broad wings, we can not currently rule-out contributions of non-gravitational motions to the observed line widths since we do not resolve the continuum and can only observe the bright, central line regions. Any such contributions would mean that the intrinsic dispersion is lower and that our dynamical mass

estimates are upper-limits.

Multi-band photometry is obtained from 3D-HST (Skelton et al. 2014), covering 0.3-24 μm for the GOODS-S (23 bands), UDS (17 bands), and COSMOS (31 bands) fields. Visual inspection of the *Spitzer*-IRAC frames show contamination from nearby objects in *UDS-7665*, *COSMOS-13184*, and *COSMOS-15091*, so their SEDs do not include the contaminated points. For the same reason, we do not include any the data from the 5.8 and 8 μm IRAC channels for this sample, even though it is available as part of the publicly-released catalogs. Only three objects have detections at 24 μm with *Spitzer*-MIPS (the photometric measurements use a deblending technique is described in Fumagalli et al. (2014), and an upper limit of 10 μJy is adopted for the remainder of the sample.

We fit the broadband spectral energy distributions of our galaxies in the same manner as Section 2.3.2 using a custom version of the `MAGPHYS` code (da Cunha et al. 2008), which computes the emission by stellar populations and the attenuation by dust in a two-component ISM, and includes nebular line emission computed self-consistently using the Pacifici et al. (2012) model (Charlot & Longhetti 2001; Pacifici et al. 2015). The broad-band fluxes computed with this model include the contamination by emission lines, so they can be directly and robustly compared with the observed fluxes that we know are likely emission-line contaminated for these galaxies (at these and higher redshifts, it has been shown that an improper treatment of nebular contamination to broadband magnitudes results in an overestimate of stellar masses and hence an underestimate in sSFRs, e.g. Atek et al. 2011; Curtis-Lake et al. 2013; Stark et al. 2013). `MAGPHYS` compares the input photometry to an extensive library of SED templates spanning a wide range in parameters such as star formation history, metallicity, age, and dust optical depth using a Bayesian method. As such, all results quoted are the medians of the posterior probability distributions for each parameter marginalized over the other parameters, with uncertainties corresponding to the 16^{th} and 84^{th} percentiles for the distribution. In cases where the output probabilities are not well constrained, typically due to the (potentially systematic) uncertainties in the photometry, we adopt an uncertainty of 0.3 dex in the relevant parameter: a formal error of 0 is indicative of the models not fitting the data well. 0.3 dex is the typical uncertainty in determining stellar masses from fits to broadband photometry (Conroy 2013). An example probability distribution for some of the various parameters is shown in Figure 3.13. Results of the SED fitting are given in Table 3.3, showing high sSFRs, low stellar masses, low metallicities, young ages, and low dust extinction. Since the NIR sizes represent the restframe optical and hence the stellar continuum at these redshifts, we are probing the same physical region in both mass estimates.

The median τ_V (V-band optical depth seen by young stars in the birth clouds) is 0.2, consistent with the very blue observed SEDs. Even with the lack of infrared data to directly probe the dust content of these systems, we can place a limit on the dust mass based on the total dust attenuation and luminosity inferred from the SED fits and a prior on the dust temperature as in da Cunha et al. (2013). Resulting limits are $\lesssim 10^7\ M_\odot$ and hence negligible compared to the stellar masses.

As mentioned before, the critical piece of additional information that we include to perform these fits is the line fluxes. We see a median SFR of $\sim$9 $M_\odot$ yr^{-1} which, combined with the low stellar masses, justifies our emission line criteria for the selection of starbursts. By separating the emission lines from the stellar continuum light, we are better able to trace the gas-phase metallicities. This results in metallicity estimates

Table 3.3. Derived Parameters

ID	log M_{dyn} ($M_\odot$)	log $M_\star$ ($M_\odot$)	log Age (yr)	Z ($Z_\odot$)	log SFR ($M_\odot$ yr^{-1})	τ_V
GOODS-S-33131	9.05±0.30	$8.91^{+0.050}_{-0.075}$	$7.78^{+0.190}_{-0.065}$	$0.321^{+0.180}_{-0.132}$	$0.892^{+0.030}_{-0.080}$	$0.242^{+0.030}_{-0.085}$
GOODS-S-43693	8.86±0.31	$8.28^{+0.195}_{-0.050}$	$7.50^{+0.240}_{-0.045}$	$0.147^{+0.160}_{-0.098}$	$0.557^{+0.090}_{-0.065}$	$0.137^{+0.050}_{-0.090}$
GOODS-S-43928	9.12±0.38	$8.83^{+0.070}_{-0.065}$	$8.39^{+0.175}_{-0.260}$	$0.169^{+0.272}_{-0.120}$	$0.262^{+0.190}_{-0.080}$	$0.327^{+0.505}_{-0.145}$
UDS-6195	9.47±0.33	$7.60^{+0.320}_{-0.300}$	$6.85^{+0.385}_{-0.300}$	$0.299^{+0.300}_{-0.130}$	$0.447^{+0.300}_{-0.065}$	$0.027^{+0.085}_{-0.300}$
UDS-6377	9.04±0.31	$8.32^{+0.140}_{-0.300}$	$6.96^{+0.735}_{-0.300}$	$0.081^{+0.096}_{-0.022}$	$1.08^{+0.300}_{-0.580}$	$1.12^{+0.025}_{-0.835}$
UDS-7665	9.07±0.33	$8.52^{+0.300}_{-0.300}$	$7.04^{+0.300}_{-0.300}$	$0.155^{+0.300}_{-0.300}$	$1.21^{+0.300}_{-0.300}$	$0.862^{+0.300}_{-0.300}$
UDS-10138	9.53±0.31	$8.43^{+0.270}_{-0.300}$	$7.10^{+0.430}_{-0.300}$	$0.177^{+0.010}_{-0.300}$	$1.05^{+0.300}_{-0.135}$	$0.112^{+0.300}_{-0.040}$
UDS-12435	9.47±0.33	$9.42^{+0.045}_{-0.055}$	$8.60^{+0.050}_{-0.130}$	$0.189^{+0.392}_{-0.138}$	$0.677^{+0.070}_{-0.030}$	$0.082^{+0.085}_{-0.040}$
UDS-12539	9.66±0.30	$8.67^{+0.300}_{-0.300}$	$7.05^{+0.300}_{-0.300}$	$0.581^{+0.300}_{-0.300}$	$1.29^{+0.300}_{-0.300}$	$0.667^{+0.300}_{-0.300}$
UDS-19167	9.35±0.34	$8.96^{+0.300}_{-0.300}$	$8.58^{+0.300}_{-0.300}$	$0.085^{+0.300}_{-0.300}$	$1.02^{+0.300}_{-0.300}$	$0.192^{+0.300}_{-0.300}$
UDS-24154	9.67±0.33	$9.10^{+0.100}_{-0.300}$	$7.49^{+0.165}_{-0.300}$	$0.531^{+0.300}_{-0.030}$	$1.38^{+0.300}_{-0.050}$	$0.462^{+0.105}_{-0.005}$
COSMOS-10599	8.65±0.40	$8.72^{+0.240}_{-0.300}$	$7.49^{+0.245}_{-0.300}$	$0.531^{+0.300}_{-0.362}$	$1.00^{+0.015}_{-0.020}$	$0.462^{+0.080}_{-0.300}$
COSMOS-12102	10.8±0.30	$9.57^{+0.300}_{-0.300}$	$8.40^{+0.300}_{-0.300}$	$0.155^{+0.300}_{-0.300}$	$1.63^{+0.300}_{-0.300}$	$1.77^{+0.300}_{-0.300}$
COSMOS-13184	8.78±0.36	$9.00^{+0.070}_{-0.220}$	$7.28^{+0.365}_{-0.095}$	$0.087^{+0.068}_{-0.040}$	$1.29^{+0.230}_{-0.120}$	$0.407^{+0.245}_{-0.110}$
COSMOS-15091	8.88±0.37	$7.92^{+0.280}_{-0.120}$	$7.61^{+0.965}_{-0.105}$	$0.169^{+0.042}_{-0.084}$	$0.062^{+0.200}_{-0.020}$	$0.077^{+0.115}_{-0.300}$
COSMOS-16286	9.22±0.40	$8.44^{+0.160}_{-0.125}$	$7.92^{+0.525}_{-0.650}$	$0.171^{+0.044}_{-0.054}$	$0.317^{+0.440}_{-0.325}$	$1.05^{+0.500}_{-0.850}$
COSMOS-16566	9.02±0.37	$8.60^{+0.040}_{-0.045}$	$8.29^{+0.065}_{-0.110}$	$0.137^{+0.324}_{-0.074}$	$0.147^{+0.035}_{-0.045}$	$0.037^{+0.050}_{-0.020}$
COSMOS-17118	9.86±0.33	$8.47^{+0.210}_{-0.315}$	$7.66^{+0.920}_{-0.425}$	$0.155^{+0.136}_{-0.070}$	$0.752^{+0.300}_{-0.085}$	$0.192^{+0.105}_{-0.010}$
COSMOS-17839	9.11±0.34	$8.19^{+0.135}_{-0.190}$	$7.43^{+0.335}_{-0.195}$	$0.091^{+0.300}_{-0.018}$	$0.392^{+0.105}_{-0.035}$	$0.037^{+0.005}_{-0.300}$
COSMOS-18358	9.54±0.32	$9.43^{+0.300}_{-0.300}$	$8.12^{+0.300}_{-0.300}$	$0.629^{+0.300}_{-0.300}$	$1.11^{+0.300}_{-0.300}$	$0.037^{+0.300}_{-0.300}$
COSMOS-19049	10.4±0.30	$9.85^{+0.168}_{-0.300}$	$8.36^{+0.165}_{-0.300}$	$0.081^{+0.046}_{-0.300}$	$1.31^{+0.120}_{-0.300}$	$1.72^{+0.200}_{-0.300}$
COSMOS-19077	9.40±0.34	$8.92^{+0.300}_{-0.225}$	$8.05^{+0.300}_{-0.555}$	$0.173^{+0.358}_{-0.300}$	$0.692^{+0.285}_{-0.300}$	$0.197^{+0.265}_{-0.300}$

Note. — Quoted values for $M_\star$, Age (mass-weighted), Z, SFR, and τ_V are the medians of the probability distributions from MAGPHYS with associated +/– 1σ values. Cases where we have an uncertainty of 0 occur when the data cannot be well-explained by the models and not when the models constrain the output parameters well, which manifests itself as a large χ^2 value. As such, we will adopt an uncertainty of 0.3 dex (the typical uncertainty for stellar masses obtained from fitting broadband photometry; Conroy 2013) in those cases to be used in the subsequent analysis.

consistent with direct probes of the oxygen abundance using emission-line ratios (see Section 3.4.2). In addition, it allows for better estimates of the extinction in the HII regions, which produce the aforementioned τ_V values.

Our model library of stellar population SEDs contains a broad range of complex SFHs, including bursts on top of extended SFHs with a variety of evolutionary trends (rising, falling, and constant). Despite these efforts, which far exceed the still common use of exclusively exponentially-declining SFHs, systematic uncertainties remain. In particular for galaxies with significant star formation activity in the past $\sim$ 50 Myr, as is the case here, red supergiants with individual luminosities of $\sim 10^5\ L_\odot$ can easily outshine more massive populations of stars with any age $>$ 50 Myr, especially in the near-infrared. Prior knowledge of the SFH is needed to address this issue, producing a degree of circularity in the problem of stellar mass determinations. Keeping this in mind, we proceed and note where necessary that for galaxies with estimated ages $\lesssim$ 50 Myr the mass (and age) estimates must be lower limits, as seen in tails to higher masses and mass-weighted ages, e.g. Figure 3.13.

Extracted near-IR spectra and SED fitting results for *GOODS-S-33131* are shown in Figure 3.2; all remaining objects in our sample are shown in Figures 3.3, 3.4, and 3.14. Telluric corrections are applied as needed.

As demonstrated in Section 2.3.2 and Figure 2.4, there is a tight, linear relation between the total dynamical and stellar mass estimates. Figure 3.5 may show that the stellar-to-dynamical mass ratio correlates with the (mass-weighted) age as well.

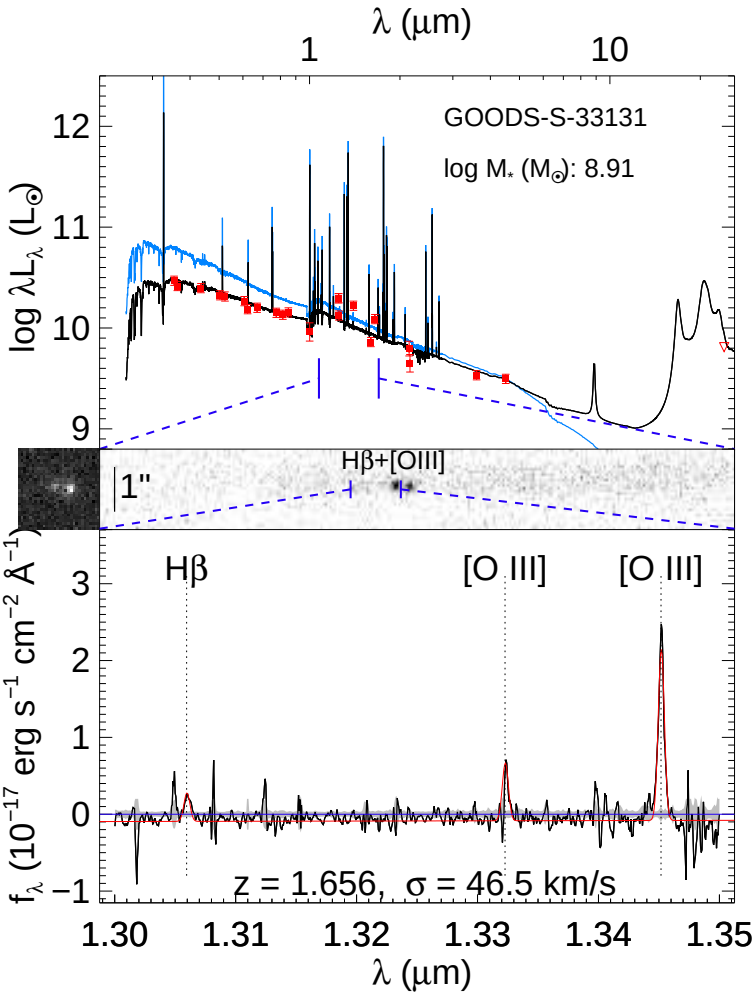

Figure 3.2: *Example of a broadband SED including best-fitting model (top), WFC3 grism image/spectrum (middle), and X-Shooter spectrum (bottom) for an object in our sample. The NIR spectra for the remaining objects can be seen in the Figures 3.3 for [O III] and 3.4 for Hα; the SEDs for the remaining objects can be seen in Figure 3.14. SED fits are performed as described in Section 3.3.1, with red points denoting the measured photometry (open points are upper limits), the blue curve denoting the non-attenuated SED, and the black curve denoting the observed SED including dust attenuation. The direct F140W image is shown on the left and the dispersed G*141 *grism image is shown to the right, with important spectral lines labeled and contamination subtracted as described in Momcheva & Brammer et al. (in prep.). The X-Shooter spectrum is smoothed by 3 pixels and is flux-calibrated according to the grism line flux. The shaded gray area represents the +/– 1σ flux uncertainties and the red curve shows the best-fitting model of the emission lines.*

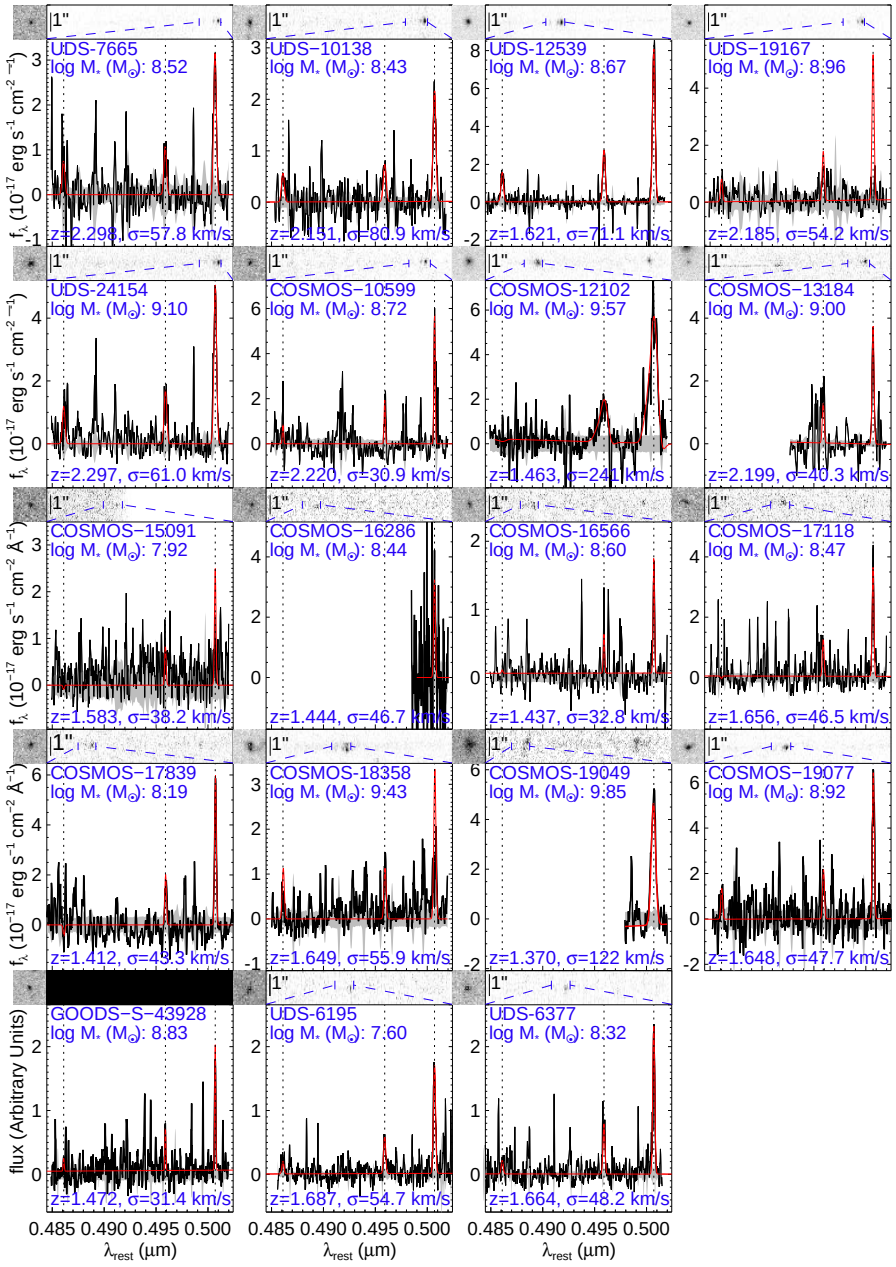

FIGURE 3.3: *WFC3 G*141 *grism and LUCI1 or X-Shooter spectrum. The spectra are smoothed by 3 pixels and are flux-calibrated according to the grism line fluxes. The shaded gray area represents the +/− 1σ flux uncertainties and the red curve shows the best-fitting model of the emission lines. The dotted lines show the position of the [O III] λλ5007,4959 and Hβ emission lines.*

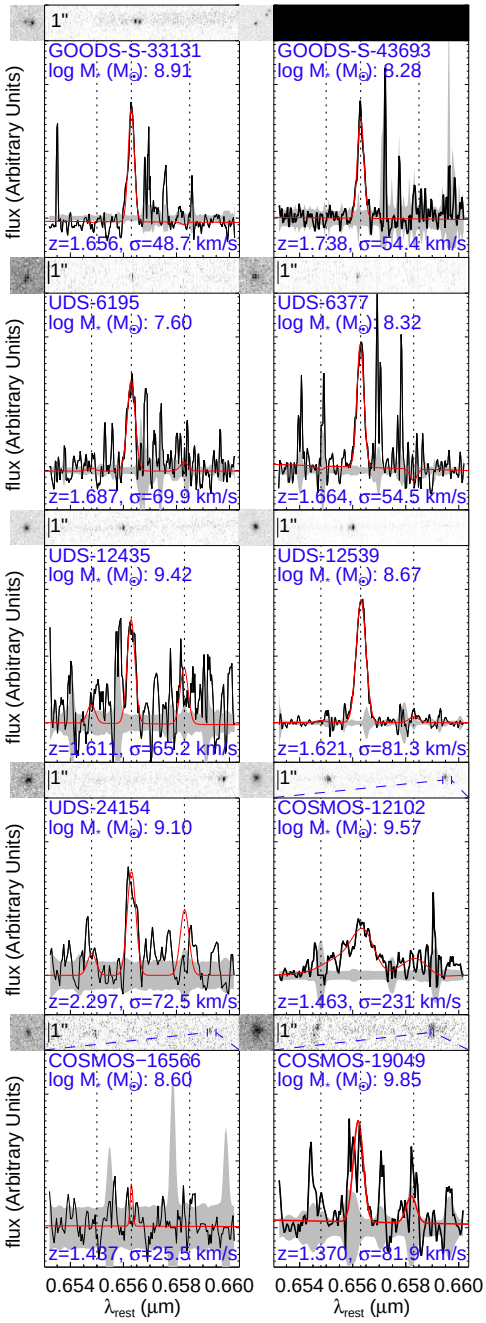

Figure 3.4: *WFC3 G*141 *grism and LUCI1 or X-Shooter spectrum, same as Figure 3.3 but for the detected Hα lines. The positions of the [N II] lines as well as the Hα line are denoted by the dotted lines.*

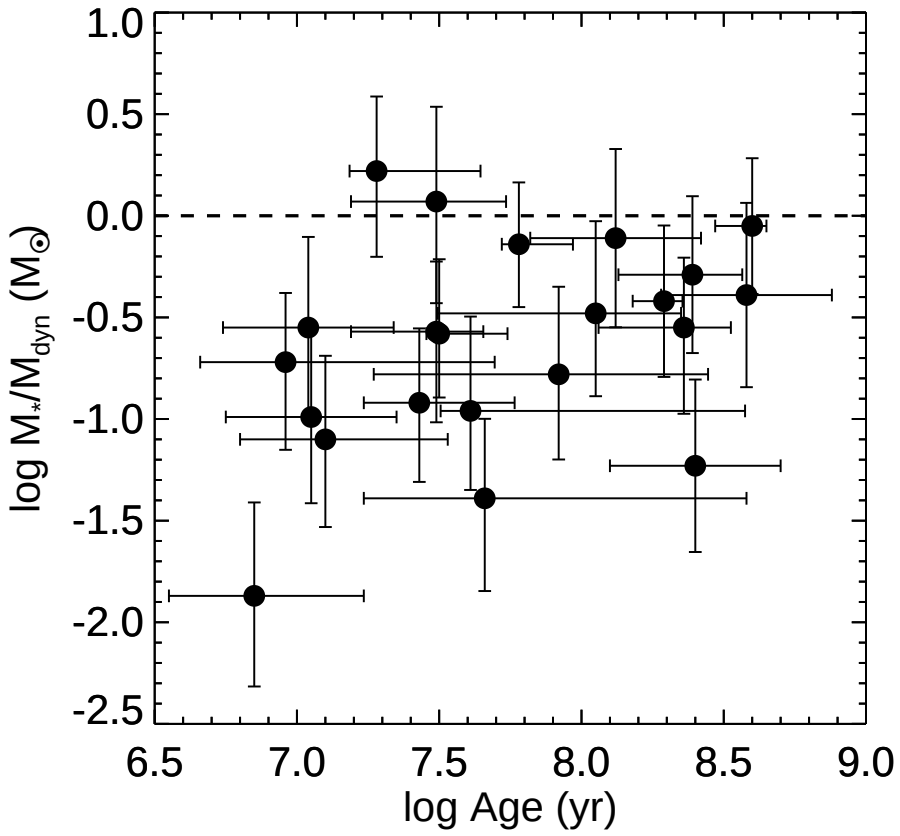

FIGURE 3.5: *Ratio of stellar mass to total dynamical mass versus age (mass-weighted) for the sample, with dynamical masses based on line measurements coming from the ground-based NIR spectra and stellar masses and ages from* MAGPHYS.

This qualitatively agrees with the model in which a non-replenished reservoir of gas is turned into stars, such that the older systems have formed a proportionally larger number of stars. For further discussion, see Section 3.5. To date, these systems represent the lowest dynamical masses ever measured at this epoch, and typically have lower stellar masses than those galaxies in similar star-forming spectroscopic surveys (e.g. Masters et al. 2014; see also Figure 3.6 and Section 3.3.2). Note that the systematic errors in M_{dyn} dominate the size of the error bar. *COSMOS-12102* shows a broad and asymmetric line profile for which the line width most likely does not trace the underlying gravitational potential. The lack of a clear trend in the relationship between the two main "observed" quantities, $M_\star$ and σ, can be seen in Figure 3.7, which suggests that any relationship between $M_\star$ and M_{dyn} must be driven by a relationship between the size of the galaxy and $M_\star$. Figure 3.8 shows this relationship, as our sample lies on or below the observed size-mass relation for late-type galaxies at $2 < z < 2.25$ as found in van der Wel et al. (2014) in 3D-HST and CANDELS.

The extreme nature of the star-formation in these systems is clearly seen in Figure 3.9. The stellar masses measured here are beginning to probe the same regime as van der Wel et al. (2011) and Brammer et al. (2012b), with similar sSFR values. Note that the sSFR values obtained from MAGPHYS are averaged over the last 10 Myr: given the ephemeral nature of the bursts, the current (s)SFR may not reflect the most vigorous

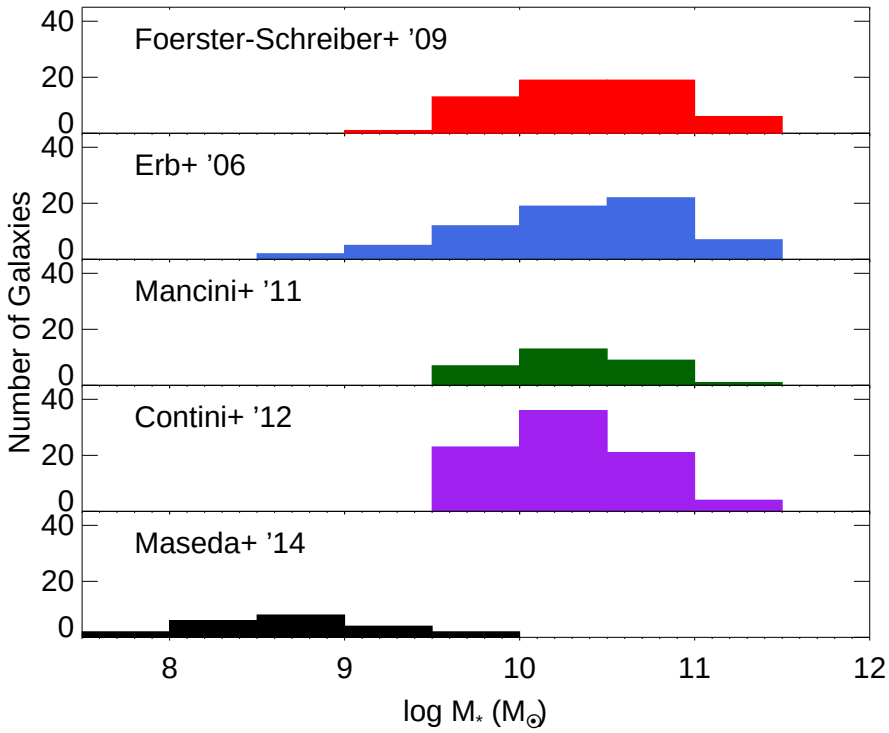

Figure 3.6: *Histograms of stellar mass for our sample compared to the larger Hα samples of Förster Schreiber et al. (2009), Erb et al. (2006), Mancini et al. (2011), and Contini et al. (2012) at $z > 1$. While variations in the stellar templates and the IMF used can alter stellar mass estimates by ∼0.3 dex, our sample still lies at considerably lower masses (up to 2 orders of magnitude lower) than the other samples.*

period of star formation in these systems. These are more than an order of magnitude in excess of the sSFR values characteristic of the star-forming population of massive galaxies at similar redshifts, measured in Hα from Fumagalli et al. (2012).

3.3.2 Comparison to Other Studies

At lower redshifts $0.11 \leq z \leq 0.93$, Amorín et al. (2014a,c) have isolated a sample of EELGs selected on [O III] flux that show remarkable similarities to our sample with sizes $r_{1/2} \sim 1.3$ kpc, masses $10^7 - 10^{10} M_\odot$, sSFR values $10^{-7} - 10^{-9}$ yr^{-1}, and metallicity estimates of $0.05 - 0.6\ Z_\odot$ (some determined "directly" using the [O III] λ4363 line as well, see Section 3.4.2). Deep HST-Advanced Camera for Surveys (ACS) *I*-band images reveal that most (80%) of their EELG sample show non-axisymmetric morphologies indicative of recent mergers or interactions. Only with samples that are complete over the redshift ranges in question will allow for a direct comparison between the two populations, which are currently only split artificially according to either optical or near-IR observations. However, caution must be taken in any interpretation: the much higher number density at $z \sim 1.7$ from van der Wel et al. (2011) than at very low-z from Cardamone et al. (2009) implies that there could be a very different mechanism involved to trigger the bursts. Connecting the two populations in a qualitative sense is the subject

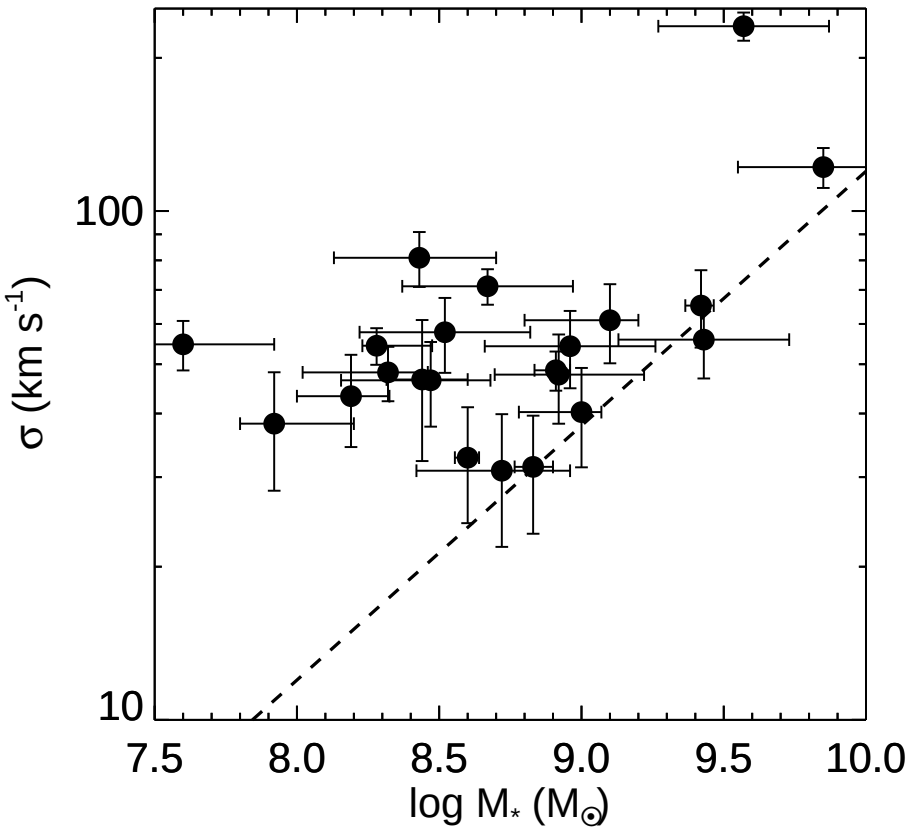

FIGURE 3.7: *Stellar mass versus observed line width for the sample. There is no clear trend of increasing line width with increasing stellar mass. The overplotted dashed line corresponds to* $M_\star \sim M_{virial}$ *for a fixed* $r_{\rm eff}$ *of 1 kpc.*

of ongoing work.

Our current observations do not allow us to make strong conclusions about the internal dynamics of individual systems. Currently, the only opportunities to study the internal dynamics of such small systems at high-redshift is with gravitational lensing: Jones et al. (2010) note that their $z \sim 2-3$ strongly-lensed galaxies would resemble mergers or dispersion-dominated systems without the additional spatial resolution provided by the lensing. Two objects similar to those presented here are *MACS J2135-0102* ($M_\star$=9.8 $M_\odot$, z=3, $r_{1/2}$=1.75 kpc, SFR=40 $M_\odot$ yr^{-1}, $\sigma_{H\alpha}$=54 km s^{-1}, V_c=67 km s^{-1}) from Jones et al. (2010) and *SHIZELS-10* ($M_\star$=9.4 $M_\odot$, z=1.45, $r_{1/2}$=2.3 kpc, SFR=10 $M_\odot$ yr^{-1}, $\sigma_{H\alpha}$=64 km s^{-1}, V_c=26 km s^{-1}) from Swinbank et al. (2012), which both appear to have a (relatively weak) rotational component to their dynamics. Further discussion of the dynamics of our present sample is deferred to Section 3.5.

Several other studies have begun to characterize the starforming properties of high-z EELGs using various techniques. The most obvious comparable study to this work is the WFC3 Infrared Spectroscopic Parallels survey (WISP, Atek et al. 2010), and specifically the study of Masters et al. (2014). As a similar WFC3 grism survey, they are also able to select galaxies based on emission lines instead of photometric techniques, and thus can isolate a sample of high-EW ELGs. Masters et al. (2014) present a sample

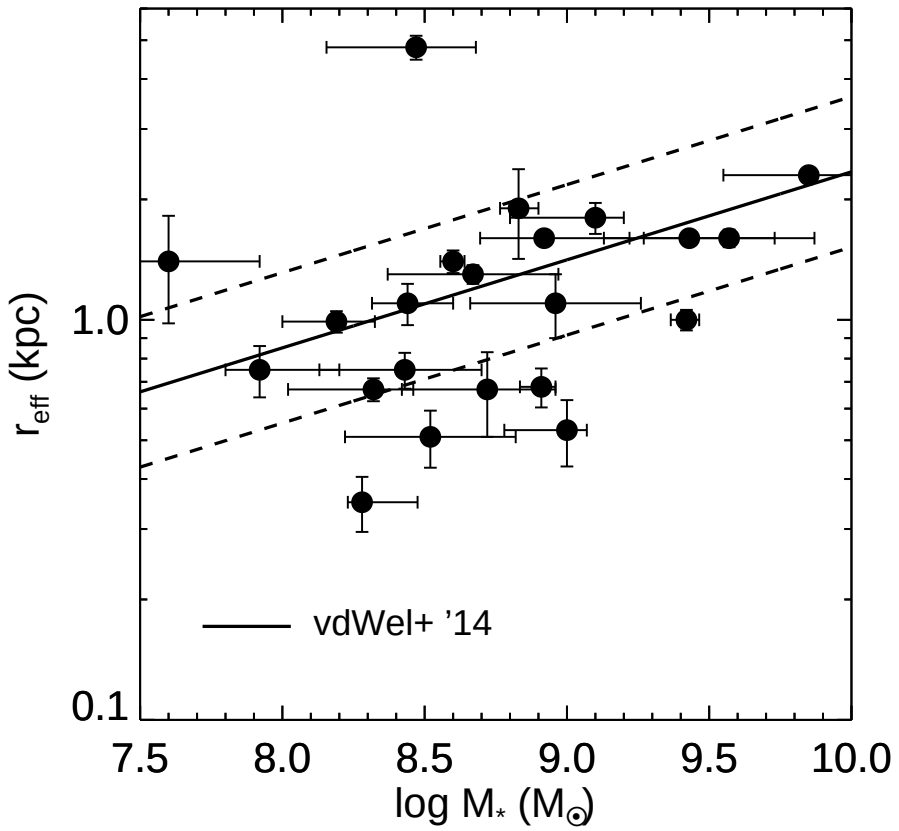

Figure 3.8: *Effective radius versus stellar mass for the sample. The overplotted lines are the low-mass extrapolation (and intrinsic scatter) to the relationship for star-forming galaxies at* $2 < z < 2.25$ *as found in van der Wel et al. (2014). The emission line galaxies in our sample fall on or somewhat below the size-mass relation for normal star-forming galaxies at similar redshifts.*

of 26 such ELGs with a median restframe [O III] EW of 154 Å (our median is 629 Å). These galaxies show similarly-low velocity dispersions (~ 70 km s^{-1}) and hence also have dynamical masses $\lesssim 10^{10} M_{\odot}$. They derive stellar masses using an assumed M/L ratio and star-formation history in a similar fashion to van der Wel et al. (2011), which have been shown to generally agree with SED-derived stellar masses (2), and have also begun to probe the $M_{\star} \lesssim 10^{9} M_{\odot}$ regime. Specific discussion of their metallicity estimates is deferred to Section 3.4.2.

In addition to WISP, narrowband studies have also begun to uncover the general starforming population of galaxies at $z > 1$, probing stellar masses below $10^{9.5} M_{\odot}$. Sobral et al. (2014) use data from the High-z Emission Line Survey (HiZELS) survey to study Hα emitters at redshifts $z = 0.84, 1.47$, and 2.23. The size of their survey area ($\sim$ 2 deg^2) and the depth of the imaging allows them to isolate large and pure samples of Hα emitters down to a restframe Hα+[NII] EW of 25 Å, constraining the stellar mass function of star-forming galaxies down to $10^{9.5} M_{\odot}$ at these redshifts. Indeed, their sample also includes a number of objects with restframe Hα+[NII] EW values in excess of 300 Å and with stellar masses from SED-fitting below $10^{9} M_{\odot}$. Their results for the characteristic sSFR (i.e. the typical SFR for a galaxy at a given mass and redshift divided by its mass) as a function of mass and redshift is shown in Figure 3.9. While some of

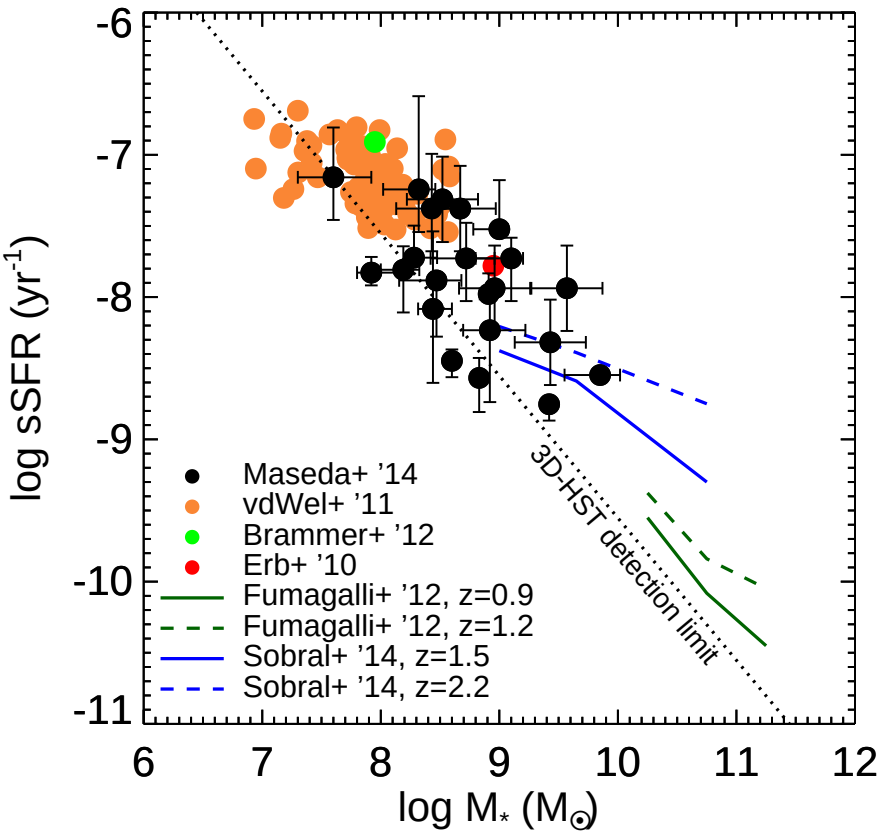

FIGURE 3.9: *sSFR versus stellar mass. Black points are the results from this study, orange points are the values from van der Wel et al. (2011), the red point is from Erb et al. (2010), the green point is from Brammer et al. (2012b), the blue lines are the results for the high/low-z bins of star-forming galaxies in Fumagalli et al. (2012), and the green lines are the results for the characteristic sSFR (SFR*/M$_\star$, see the text for details) for narrow-band selected star-forming galaxies in Sobral et al. (2014). The diagonal dotted line represents the nominal detection limit from the 3D-HST survey of 2.8 M$_\odot$ yr^{-1} at z ∼ 1.5 (cf. Chapter 4). The sSFRs are averaged over 10 Myr.*

our objects can be considered "normal" at these redshifts according to this determination, a majority of them still have higher sSFRs than expected, albeit typically within 1 dex. This reinforces the notion that these objects are the high-EW tail of the total distribution of star-forming galaxies at these redshifts and do not comprise a genuinely separate population (van der Wel et al. 2011).

3.4 EMISSION-LINE RATIOS

3.4.1 STARBURSTS OR AGN?

So far, the main caveat is that we have assumed that star formation is primarily responsible for the strong line emission. The most compelling evidence to support this

assumption is the relation between stellar mass and dynamical mass, and that the dynamical masses, with two exceptions, do not exceed 10^{10} $M_{\odot}$ (Section 2.3.2). Such a result would be entirely coincidental in the case that the emission lines are powered by AGN since the width of AGN emission lines is not coupled to the stellar mass of the host galaxy. In other words, we observe narrow emission lines in these small ($\sim$ 1 kpc) systems, while typical AGN narrow line regions have much larget emission-line widths $\sigma > 200\,\mathrm{km\,s^{-1}}$ (Osterbrock & Mathews 1986). However, it is useful to look for evidence of AGN contributions.

Although low-metallicity, low-mass AGN are exceedingly rare in the local universe (Izotov & Thuan 2008), there is some evidence that they may be more common at higher-z (Trump et al. 2011; Xue et al. 2012; Reines et al. 2013). Such AGN could cause large observed line fluxes. At $z > 1$, AGN identification with a simple diagnostic such a high [O III] λ5007/Hβ ratio becomes insufficient by itself, as shown by Trump et al. (2013). We thus utilize the "BPT" diagnostics of Baldwin et al. (1981) for the objects in our sample with measurements of [N II] and/or [S II] in addition to Hα. Given that these lines are typically quite weak in star forming galaxies and the strong influence of OH skylines in our NIR spectra, in some instances we can only place an upper-limit on the ratios of those lines with Hα. These two BPT diagrams are shown in the left and central panels of Figure 3.10 with contours showing galaxies from the SDSS MPA-JHU value-added DR7 catalog.

Most of our points plausibly lie on an extension of the starforming region of the BPT diagrams and not on the extension of the AGN region, or at least they lie far from the main locus of AGN-powered emission lines. However, low-metallicity AGN can lie in the starforming region as well (Groves et al. 2006; Kewley et al. 2013), preventing us from completely ruling out the contribution of AGN to our sample with these diagnostics. In some cases we observe higher [O III]/Hβ ratios compared to the other starforming galaxies, but this can be explained simply by higher ionizations and lower metallicities in these systems compared to the low-z sample of SDSS galaxies. Kewley et al. (2013) find that starforming galaxies at $z > 1$ are consistent with models that have more extreme ISM conditions than those in the local universe[1]. High electron temperatures (discussed in the next section) support such a hypothesis. This would be a further, unexplained coincidence if they are AGN in addition to the low dynamical masses described previously. While Trump et al. (2011) suggest that AGN are widespread in low-mass $1.3 < z < 2.4$ galaxies, the emission lines are not actually dominated by the AGN. This is most evident in the $L_{0.5-10\ keV}/L_{[OIII]}$ relationship: the [O III] lines have some AGN contribution, but (on average) less than 50%.

Additionally, we utilize the Mass-Excitation (MEx) diagnostic of Juneau et al. (2011), which combines the [O III] λ5007/Hβ ratio with the stellar mass. Trump et al. (2013) conclude that this diagnostic also gives a meaningful probabilistic constraint on the AGN/SF nature of galaxies at $z > 1$ using a combination of the BPT diagnostics and X-ray data. While this diagnostic is easily applicable to our data, we can not constrain the MEx AGN/starforming *probabilities* for most of our sample given that it is not properly calibrated for objects with such low metallicities and high sSFRs, AGN or otherwise: the five objects with a probability of star formation (P_{SF}, compared to the probability that they are AGN; *COSMOS-18358*, *COSMOS-13184*, *COSMOS-10599*, *UDS-24154*, and *UDS-12435*) have a median P_{SF} value of 0.940, firmly placing them in

[1] While beyond the scope of this Thesis, we would like to point out the large uncertainties in assumptions about the ISM conditions in galaxies at high redshift given the lack of knowledge about ionizing spectrum of hot stars at these early times and low metallicities.

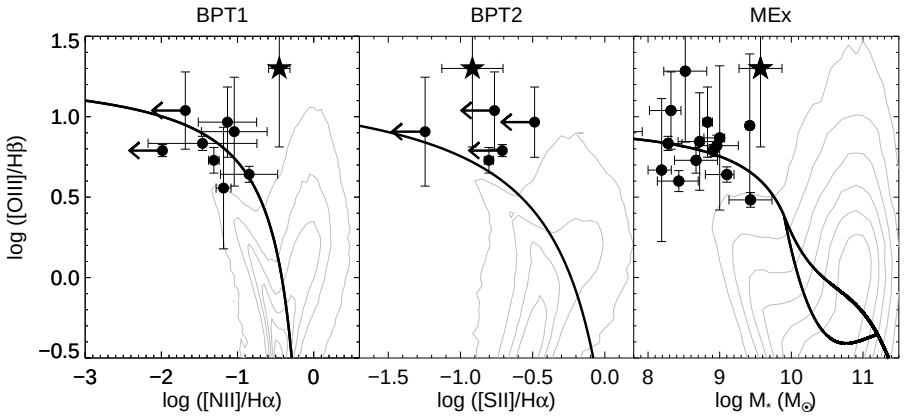

FIGURE 3.10: *AGN/SF emission line diagnostic plots. From left to right, the BPT1 diagnostic of [N II] λ6584/Hα, the BPT2 diagnostic of [S II] λλ6718,6731/Hα, and the MEx diagnostic (Juneau et al. 2011) of stellar mass. Divisions between the AGN and the star-forming regions in the BPT diagrams come from Kewley et al. (2006). In all cases, the gray contours represent data from the SDSS MPA-JHU value-added DR7 catalog: these emission line and stellar mass measurements are described by Tremonti et al. (2004) and Kauffmann et al. (2003). Arrows denote 3σ upper limits. Each of the diagnostics point to star formation as the ionizing source with at most mild AGN contribution, the possible exception being COSMOS-12102 (star symbol). The large uncertainties in [O III]/Hβ are caused by very low and uncertain Hβ fluxes, as [O III] is robustly detected in all of these cases; the true ratio could be even higher than the values plotted here.*

the starforming regime. The remaining objects, while probabilistically unconstrained, still lie far from the population of AGN in the MEx diagnostic plot, as shown in Figure 3.10.

We can place other constraints on the AGN nature of these systems in much the same way as van der Wel et al. (2011), i.e. independent of any measured emission line ratio(s). Most objects in our sample do not have strong 24 μm detections using *Spitzer*-MIPS: *COSMOS-18358* has a MIPS 24μm flux of 21.5±9.0 μJy and clearly appears to be a merger; *COSMOS-19049* has a flux of 14.1±8.6 μJy, is physically large with r_{eff} = 2.3 kpc, and also has broad lines with $\sigma_{[OIII]}$ = 122 km s^{-1}; *COSMOS-12102* has a flux of 55.3±8.7 μJy and is further discussed below. While none of our objects have X-ray detections, GOODS-S is also the only field with sufficient depth to find $z \sim 2$ AGN which are not quasars. That being said, it is possible to hide even a rapidly accreting X-ray AGN in a low mass galaxy (Aird et al. 2012). The consistent (and resolved) J_{F125W}- and H_{F160W}-sizes, as well as the sizes of the emission lines in the grism spectra, rule out the presence of a strong point source dominating the emission.

An exception could be *COSMOS-12102*, illustrated by the star in Figure 3.10, which is also has the largest line width in our sample. Reines et al. (2013) find active black holes in similar mass dwarf galaxies with broad Hα emission in the local universe with $M_{BH} \lesssim 10^6\ M_\odot$. Using their relation (Equation 5) of $L_{H\alpha}$ and FWHM$_{H\alpha}$ (full width at half maximum) to M_{BH}, *COSMOS-12102* has a black hole mass of $\sim 10^{6.2}\ M_\odot$, which is in their observed range. The mass determination is fraught with systematic uncertainties, such as variations in the geometry of the broad-line region and that at least some of the Hα luminosity comes from star formation, but we cannot conclusively rule-out some AGN contribution for this galaxy.

3.4.2 METALLICITY

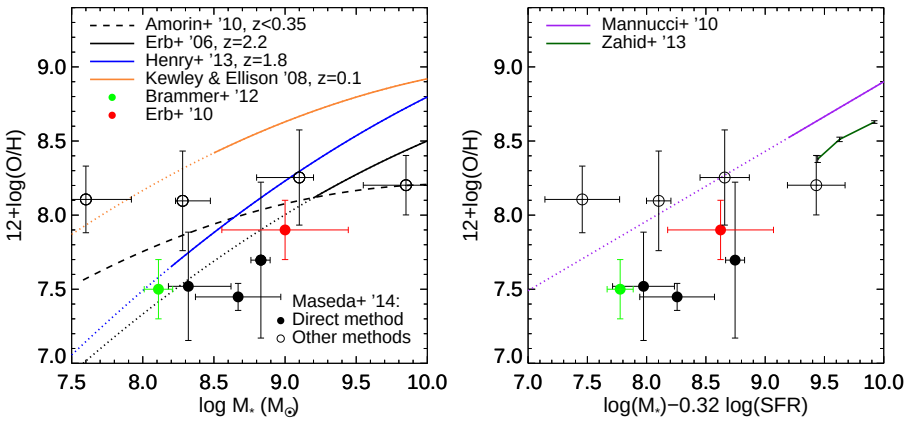

FIGURE 3.11: *Left panel: Oxygen abundances as a function of stellar mass. Overplotted are the mass-metallicity (MZ) relations of Kewley & Ellison (2008), Henry et al. (2013b), and Erb et al. (2006) with low-mass extensions given as the dotted lines, using the Maiolino et al. (2008) parameterization. The dashed line is the Amorín et al. (2010) relation for luminous compact "green pea" galaxies at* $0.11 < z < 0.35$. *Right panel: Oxygen abundances for our sample as a function of* μ_{32} *as defined in Mannucci et al. (2010), with the Fundamental Metallicity Relation (FMR) from Mannucci et al. (2010) and the high-SFR bin from Zahid et al. (2014) overplotted. In both panels, filled points denote abundances obtained from the "direct"* T_e *method and open points denote other methods. The red point shows the result from Erb et al. (2010) and the green point shows the result from Brammer et al. (2012b). Overall we observe that our objects lie on or below the low-mass/high-SFR extrapolations to these observed relationships at similar redshifts.*

In order to measure the gas-phase oxygen abundances of these galaxies as a proxy for the metallicity, we first implement the so-called "direct" or T_e method which requires a detection of the auroral [O III] λ4363 line as well as the [O III] $\lambda\lambda$4959,5007 and [O II] λ3727 lines. Some of these lines lie in the UV/Visible at these redshifts, so we can only apply this method to the X-Shooter sample. Using the calibrations outlined in Izotov et al. (2006), we convert the [O III] emission-line ratios into an electron temperature (with the electron density constrained by the ratio of [O II] λ3729 to λ3726 or [S II] λ6717 to λ6731) in the O^{++} region. The total oxygen abundance in the galaxy is O/H = $O^+/H^+ + O^{++}/H^+$, assuming $\log T_e(O^+) = 0.7 \log T_e(O^{++}) + 0.3$. Two objects, *UDS-12539* and *UDS-6377*, have detections of λ4363 and an upper limit can be obtained for a third, *GOODS-S-43928*. This object also lacks a detection of [O II] λ3727 due to skyline contamination, so the O^+/H^+ component cannot be constrained directly. The relative contribution of the O^+/H^+ component to the total oxygen abundance is 1.8% and 7.3% for the other two objects, so we neglect its contribution to the abundance of the third object. The N2 method of (Pettini & Pagel 2004; PP04), which uses the (log) ratio [N II] λ6584/Hα, verifies this result. All derived temperatures are in excess of 20,000 K.

For the remainder of the sample, we must resort to other methods, namely the aforementioned N2 method and also the O3N2 method, both from PP04; O3N2 is the (log) ratio [O III] $\lambda\lambda$4959,5007/Hβ/N2. For both methods, uncertainties include contributions from the error in the line ratios as well as the systematic scatter in the relations. If Hβ is not detected at more than 1σ in our LUCI1 or X-Shooter spectrum, we estimate the [O III]/Hβ ratio from the grism spectrum. Also note that in the two instances where the N2 method is used the Maiolino et al. (2008) calibration results in metallicities consistent with the PP04 values. Results are displayed in Table 3.4, with a median

Table 3.4. Metallicity Estimates

ID	12 + log(O/H)	Method
GOODS-S-43693	8.10±0.34	N2
GOODS-S-43928	7.70±0.53	T_e/N2
UDS-6195	8.11±0.23	O3N2
UDS-6377	7.52±0.37	T_e
UDS-12539	7.45±0.09	T_e
UDS-24154	8.25±0.32	O3N2
COSMOS-19049	8.20±0.20	N2

$12 + \log(O/H)$ value of 7.90 (0.15 $Z_\odot$). This value agrees well with the median MAGPHYS-derived metallicity of 0.17 $Z_\odot$ for the full sample.

Given the relatively small number of direct measurements of the oxygen abundance in high-z galaxies, this provides an important piece of information. Since the standard R23 diagnostic (Pagel et al. 1979) using [O III] $\lambda\lambda$5007,4959 + [O II] $\lambda\lambda$3726,3729 + Hβ is double-valued, it is important whether higher-z galaxies belong to the metal-rich upper branch or to the metal-poor lower branch. Henry et al. (2013a) argue in favor of the upper-branch for galaxies with $\log(M_\star/M_\odot) > 8.2$ at $z \sim 0.7$, and Henry et al. (2013b) favor the upper-branch for galaxies with $\log(M_\star/M_\odot) > 8.8$ at $1.3 < z < 2.3$. Our measurements suggest that these systems plausibly lie on the lower branch, even at $\log(M_\star/M_\odot) < 9.2$.

In the left panel of Figure 3.11 we show these results as well as those of Brammer et al. (2012b) and Erb et al. (2010) with the low-mass extrapolations to the mass-metallicity (MZ) relations from Kewley & Ellison (2008) for $z \sim 0.1$, Henry et al. (2013b) for emission line galaxies at $z \sim 1.8$, and Erb et al. (2006) for starforming galaxies at $z \sim 2.2$ utilizing the metallicity calibrations and functional parameterization of Maiolino et al. (2008), as well as the results from Amorín et al. (2010). The right panel of Figure 3.11 shows the same data plotted against the low-mass extrapolation of the "fundamental metallicity relation" (FMR) of Mannucci et al. (2010) and the relation for high-SFR galaxies at $z \sim 1.6$ from Zahid et al. (2014). Neither method is directly calibrated below $\sim 10^9\ M_\odot$, which is precisely the range we probe here.

In the case of the MZ relation, our results generally agree with the Erb et al. (2006) and Henry et al. (2013b) extrapolations and typically have lower metallicities than objects with similar masses and star formation rates at lower redshifts. We see good agreement with distribution in $12 + \log(O/H)$ with $M_\star$ from Amorín et al. (2010) as well. The slight overall trend observed where higher-mass objects have higher metallicities supports the idea that the lowest-mass objects are the youngest and therefore have formed less mass of heavy elements. The youngest objects should also have the highest sSFRs, which is known to drive much of the scatter in the MZ relation. Henry et al. (2013a) also explain that the steepness of the O/H versus $M_\star$ relation has a direct theoretical impact on the role of outflows in these systems.

In the FMR relation the solid points, denoting T_e-determined abundances, are considered more reliable at low metallicities (Maiolino et al. 2008) and lie somewhat below the FMR, perhaps more in line with an extrapolation to the $z \sim 1.6$ findings of

Zahid et al. (2014). Since Mannucci et al. (2010) do not see the higher-mass turnoff in the relation until $z > 2.5$, we may be observing the evolution of the FMR on the low-mass and/or high-SFR end, although we do not have the number statistics yet to quantify any offset. At the very least, we can conclusively rule-out that these objects lie above the FMR (cf. Stott et al. 2013 who claim this relation is driven by the higher average SFRs of the systems probed at higher redshifts).

3.5 Constraints on the Gas Fraction and the Star Formation Efficiency

In this section we use the observed velocity dispersions σ and sizes $r_{\rm eff}$, combined with dynamical stability criteria, to constrain the gas fraction and its implications. We assume that the systems consist entirely of stars and gas: we neglect the contribution of dark matter to the total dynamical mass as measured within the central kiloparsec. We also assume that these systems are isolated and not embedded in larger (gaseous) structures that exert pressure.

We do not know the geometry of the systems, and therefore consider two extreme cases: for the case of a sphere with uniform density we calculate the Jeans mass M_J; for the case of a thin rotating disk we calculate the Toomre parameter Q. In both cases we assume that the gaseous body has the same extent as the stellar body, and that the velocity width of the nebular lines traces the total gas kinematics.

For a uniform sphere the Jeans mass (Binney & Tremaine 2008) is given by

$$M_J = \frac{4\pi}{3}\rho_0\left(\frac{\pi\sigma^2}{4G\rho_0}\right)^{3/2}, \tag{3.2}$$

where we have equated the sound speed with observed velocity dispersion. This velocity represents the combined effect of all sources of pressure that act against collapse, which include thermal motions (associated with the physical sound speed) as well as turbulence and streaming motions.

ρ_0 is the density of the gas, which is given by the gas mass ($f_{gas} \times M_{dyn}$) and the size:

$$\rho_0 = \frac{f_{gas}M_{dyn}}{(4/3)\pi r_{eff}^3}, \tag{3.3}$$

where f_{gas} is the gas fraction. The total dynamical mass M_{dyn} is taken from Equation 3.1, with a value of 5 for the proportionality constant for consistency with the case under consideration here: that of a sphere with uniform density[2].

For typical values of r_{eff} (1 kpc) and σ (50 $\rm km\,s^{-1}$) we find that $M_J \simeq M_{gas}(\equiv f_{gas}M_{dyn})$ for $f_{gas} = 0.66$. Given that substantial star formation in these systems the gaseous body must be unstable: we conclude, assuming a homogeneous gaseous sphere, that $f_{gas} \gtrsim 0.66$.

In order to address the question to what extent this conclusion is affected by the chosen geometry, we now consider the other (opposite) case, and assume that these

[2]Elsewhere in this Thesis we use a value of 3, which corresponds to other, more realistic geometries such as inclined disks and radially-concentrated density profiles (e.g., isothermal).

systems are rotating disks, where instability can be described by the Toomre parameter Q (Toomre 1964; Binney & Tremaine 2008)

$$Q_{gas} = \frac{\sigma_z \kappa}{\pi G \Sigma_{gas}} \tag{3.4}$$

where σ_z is the velocity dispersion perpendicular to the disk, and Σ_{gas} is the average gas-mass surface density, given by

$$\Sigma_{gas} = \frac{M_{gas}}{2\pi r_{eff}^2} = \frac{M_{dyn} f_{gas}}{2\pi r_{eff}^2}, \tag{3.5}$$

where f_{gas} is the gas fraction. The epicyclic frequency, κ, in a rotating exponential disk is

$$\kappa = \sqrt{2}(v_t / r_{eff}), \tag{3.6}$$

where v_t is the circular velocity of the disk.

While σ_z and v_t are not observed directly, both contribute to the observed emission line width, σ. The contribution of rotation to σ, assuming an average inclination of 60 degrees and an exponential disk, is $\sim v_{rot}/\sqrt{2}$, such that we have

$$\sigma_{obs}^2 = \sigma_z^2 + v_t^2/2, \tag{3.7}$$

which is empirically supported (Kassin et al. 2007).

Combining the above, we solve for v_t as a function of σ_{obs}:

$$v_t^2 = \sigma_{obs}^2 \left(1 \pm \sqrt{1 - (9/4) f_{gas}^2 Q_{gas}^2}\right), \tag{3.8}$$

such that an unstable system ($Q < 1$) requires

$$f_{gas} > \frac{2}{3} \tag{3.9}$$

in order to produce a unique, physical solution.

Remarkably, regardless of whether we assume a homogeneous sphere or a rotating disk for the gas, we find that a high gas fraction is needed to explain the observed star formation activity. At the same time, the non-negligible contribution of the stellar mass to the total mass implies that f_{gas} cannot be arbitrarily close to unity and should be $\lesssim 0.9$ (see Figure 3.5).

A significant caveat is that the proportionality constants in Equations 3.2, 3.3, 3.1, 3.6, 3.7, and 3.8 depend on the details of the assumed geometry and dynamical structure; their variation can alter the threshold value of f_{gas}. In addition, we ignore the stabilizing effect of the stellar disk on the gas disk, however this increases the implied gas fraction further.

The median gas fraction in our sample is 72% (i.e. the y-axis in Figure 3.5 is a proxy for f_{gas}), in agreement with the theoretical calculation. While some objects are observed to have lower gas fractions, 18 out of our 22 objects are consistent with $f_{gas} > 2/3$ within 1σ.

In the following we assume f_{gas}=2/3 in order to constrain the star formation efficiency. In Figure 3.12 we show the star formation rate surface density, assuming

$\Sigma_{SFR} = SFR/(2\pi \times r_{eff})$, versus the gas surface mass density Σ_{gas} (from Equation 3.5). The implied gas depletion time scale ranges from $\tau_{depl} = 10^{7.5}$ to 10^9 yr, with a median of 3×10^8 yr.

Compared to normal present-day galaxies, gas is efficiently transformed into stars but, with the exception of a few objects, not as efficiently as observed in star-bursting regions in the Milky Way and starbursting galaxies in the present-day or high-redshift universe (i.e. Kennicutt et al. 2007; Daddi et al. 2010a). This mostly reflects the large gas fractions needed to produce systems that are unstable against star formation, rather than a modest level of star formation: the inverse sSFR (stellar mass growth time scale) of $1/sSFR = 5 \times 10^7$ yr is very short, among the fastest ever measured. Hence, the stellar mass grows at a dynamical time scale ($\tau_{dyn} \sim 3 \times 10^7$ yr).

The physical interpretation is that the star formation rate is not limited by availability of fuel but by the dynamical time scale. However, we have to keep in mind that we selected galaxies based on their sSFR: we are biased against objects that are older and/or have longer star formation time scales. Further empirical investigation of lower levels of star formation in similarly massive galaxies is needed to address this issue.

However, we propose that star formation will halt within $\sim$ 50 Myr, long before the gas reservoir is depleted. First, the stability arguments given above imply that the gas fraction only needs to be reduced by a small amount (from the assumed $f_{gas} = 2/3$ to, say, $f_{gas} < 0.5$). Given the observed SFR, this takes $\sim$50 Myr. Second, feedback should play an important role in these low-mass systems with small escape velocities (several 100 $\mathrm{km\,s^{-1}}$) and high SFR: gas is easily transported out of the galaxy, and perhaps even out of the halo, preventing recycling. This paradigm is supported by Law et al. (2009, 2012), who see that higher mass starforming galaxies at z $\sim$ 2 can support more extended rotationally-supported disks and are less efficient at driving outflows than their lower mass counterparts.

In the above we have ignored the infall of cold gas, which could continue to feed and maintain the starburst. Assuming that these galaxies reside in relatively low-mass halos ($\sim 10^{11} M_\odot$) the typical accretion rate onto the halo is several $M_\odot$/yr (McBride et al. 2009), somewhat lower than the SFR. The accretion rate onto the halo is not necessarily equal to the accretion rate onto the galaxy, and the latter is likely not constant. A period of above-average accretion for several 100 Myr could, in principle, sustain the starburst. However, above-average accretion events are more likely to be of short duration, such that one such event can ignite the observed starburst by pushing the gas mass surface density above the threshold for star formation or by disturbing the already-present gas, creating an instability. Hence, enhanced accretion could cause the star formation activity but not maintain it.

Based on the Jeans and Toomre instability arguments presented above, purely gaseous systems with velocity dispersions and sizes as observed become unstable once they reach a total mass of a few times 10^9 $M_\odot$, close to the observed masses of the objects in our sample.

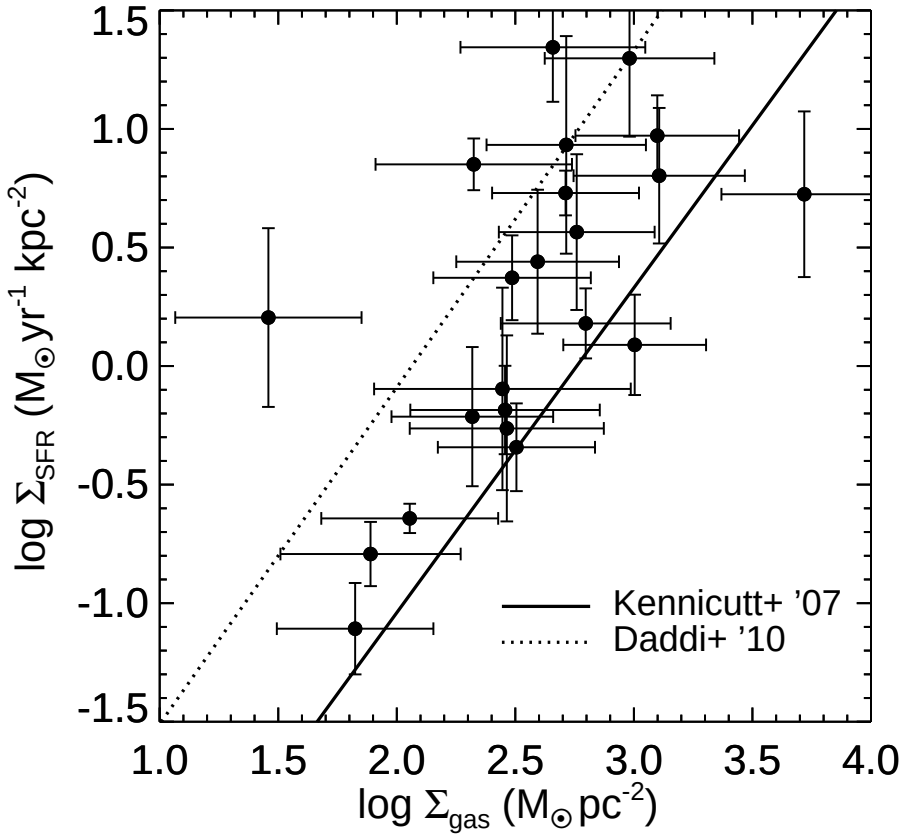

FIGURE 3.12: *SFR surface density versus gas-mass surface density. The gas masses are estimated according to* $M_{gas} = (2/3) \times M_{dyn}$*, which is inferred as a probable gas fraction given the star formation rates and* $M_\star/M_{dyn}$ *ratios (which imply* $0.5 \lesssim f_{gas} \lesssim 0.9$*) in these systems. The solid black line shows the relation for local spiral galaxies from Kennicutt et al. (2007) and the dotted line shows the result for local (U)LIRG and high-z SMGs/QSOs from Daddi et al. (2010a). The location of the points suggests that these objects spend at least some of the time forming stars more efficiently than the normal, present-day spiral galaxies. Our constraints are not stringent enough to confirm or rule out gas depletion timescales that are on par with or even shorter than more massive, starbursting systems.*

3.6 Concluding Remarks

We present near-infrared spectroscopy from the LBT/LUCI1 multi-object spectrograph and the VLT/X-Shooter wide band spectrograph for a sample of HST/WFC3 grism-selected emission line objects with restframe equivalent widths of $EW = 200-1100$ Å for [O III] λ5007 and/or Hα, and located in the redshift range $1.3 < z < 2.3$. The observed emission lines are narrow, with measured velocity dispersions down to $\sigma = 30$ km s^{-1}, implying low dynamical masses of $\sim 10^9\ M_\odot$, even for the lower-EW objects not included in Chapter 2. Using sophisticated `MAGPHYS` SED fitting to broadband magnitudes and the inclusion of line fluxes, we observe low stellar masses as well, $\sim 3 \times 10^8\ M_\odot$. Ratios of $M_\star$ to M_{dyn} range from 1/10 to 1, which makes AGN-dominated SEDs unlikely. Emission-line ratios and the narrow line widths also suggest that AGN do not significantly contribute to our sample, and therefore we conclude that the main ionizing source is hot, massive stars.

Direct probes of the oxygen abundances within these galaxies and [O III]/Hβ line ratios of typically $\gtrsim 5$ corroborate the expectation that these low mass systems have low metallicities, between 0.05 and 0.3 $Z_\odot$. They lie on or below the (extrapolated) mass-metallicity relationships for these redshifts (Henry et al. 2013b; Erb et al. 2006) which, combined with their young SED-derived ages, reinforces the notion that these are nascent galaxies undergoing their first major episode of star formation.

Measured sSFR values of $\sim 10^{-8}$ yr^{-1} for these galaxies are up to two orders of magnitude larger than those of typical $10^{10}\ M_\odot$ starforming galaxies at $z \gtrsim 1$ (Fumagalli et al. 2012), as well as comparable to or greater than the values from other high-EW systems as discovered in deep narrowband searches (Sobral et al. 2014) and in deep spectroscopic studies at both similar (Masters et al. 2014) and lower redshifts (Amorín et al. 2014a,c). Such high sSFR values have been difficult to reproduce in hydrodynamical simulations, but recently Shen et al. (2014) made significant progress by combining a high gas density threshold for star formation and a blastwave scheme for supernova feedback in their simulations of low-mass galaxies.

Such low mass systems, with observed velocity dispersions of $\sigma \sim 50$ km s^{-1} and sizes of ~ 1 kpc are only unstable against star formation if their gas fractions are high (above 2/3), in agreement with the observed $M_\star/M_{dyn}$ relation. The bursts are likely to be short-lived (~50 Myr), as, even in the absence of feedback, their intense star formation will rapidly build up stellar mass and lower their sSFR well before the gas depletion timescale (~100 Myr).

These results strengthen the conclusions from van der Wel et al. (2011), who argued that EELGs represent low-mass, starbursting galaxies. Additionally, the existence of (at least) two strong galaxy-galaxy lenses in the CANDELS/3D-HST fields where the background galaxy is an EELG at $z = 1.85$ and 3.42 (Brammer et al. 2012b; van der Wel et al. 2013respectively) suggests that this type of object is common. The ubiquity of EELGs may be even more pronounced at high redshifts (>6; Smit et al. 2014). Such systems at $z = 1 - 2$ thus may present an opportunity to study how star formation proceeded in the early universe before the advent of the next generation of observatories, such as the *James Webb Space Telescope* (JWST).

The new generation of submillimeter observatories, such as ALMA, can provide direct estimates of the gas masses. Searching for the presence of outflowing material would provide valuable clues about the feedback processes going on in these systems,

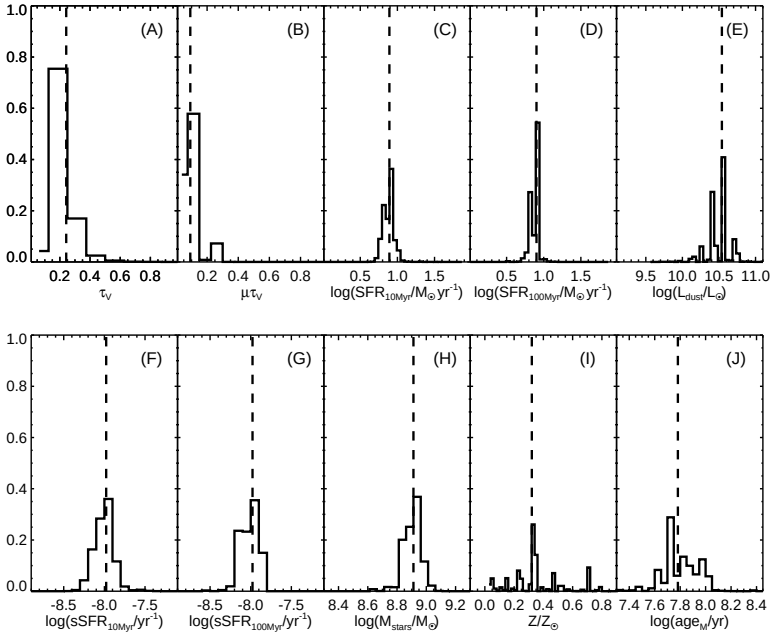

FIGURE 3.13: *Probability distributions from* MAGPHYS *for GOODS-S-33131. Vertical dashed lines denote the medians of the output probability distribution, which are quoted throughout this work. Panels denote the following: (A) V-band optical depth seen by young stars in the birth clouds; (B) V-band optical depth seen by stars in the diffuse ISM; (C) star formation rate averaged over the last 10 Myr; (D) total dust luminosity; (E) star formation rate averaged over the last 10 Myr divided by stellar mass; (F) stellar mass; (G) stellar metallicity (which we set equal to the gas-phase metallicity); (H) mass-weighted age.*

which is especially relevant to support the hypothesis that these bursts can create the cored dark matter profiles observed in local dwarf galaxies (e.g. Amorisco & Evans 2012).

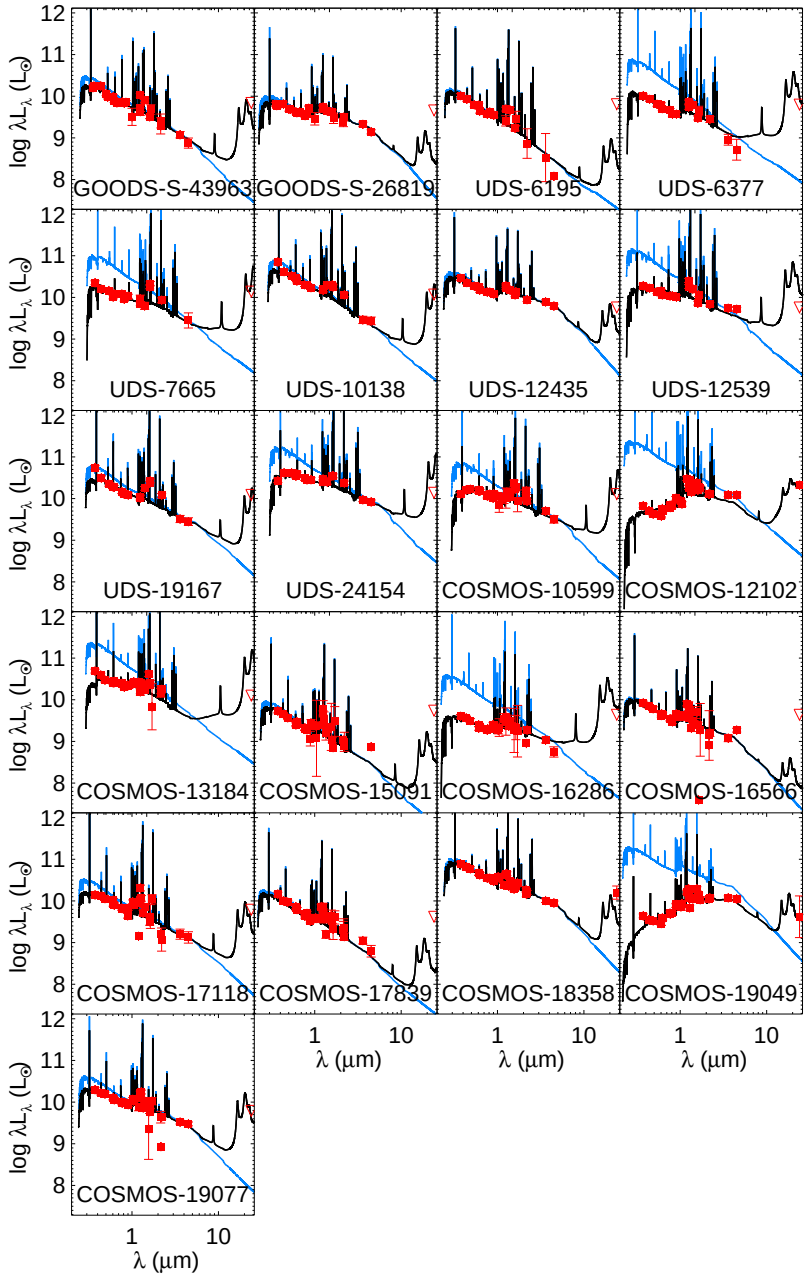

Figure 3.14: *Best-fit SEDs for the remaining objects in the sample. The fits are performed as described in Section 3.3.1, with red points denoting the measured photometry (open points are upper limits), the blue curve denoting the total non-attenuated SED, and the black curve denoting the observed SED including dust attenuation.*

Chapter 4

Statistical Detection of Emission Lines in 3D-HST

All the proofe of a pudding, is in the eating.

William Camden
Remaines of a Greater Worke, Concerning Britaine; 1605

The multiplexing capability of slitless spectroscopy is a powerful asset in creating large spectroscopic datasets, but issues such as spectral confusion make the interpretation of the data more challenging. Likewise, any systematic analysis is more difficult than in traditional spectroscopic datasets. Here we present a complete search for emission lines in the slitless grism spectroscopic data from the 3D-HST survey utilizing the Wide-Field Camera 3 on the *Hubble Space Telescope*. Using a novel statistical technique, we can detect compact (extended) emission lines at 90% completeness down to fluxes of 3.7 (7.4)$\times 10^{-18}$ erg s^{-1} cm^{-2}, close to the noise level of the grism exposures, for objects detected in the deep ancillary photometric data. Compared to previous methods, the Bayesian nature allows for probabilistic line identifications even in the absence of high signal-to-noise or secondary emission line detections. Detections of multiple strong emission lines or single lines combined with photometric redshift information lead to 373 Hα/[O III] redshift confirmations in GOODS-S, allowing us to trace the number density evolution of EELGs systematically.

4.1 CONTEXT

In recent years, combinations of deep imaging and spectroscopy with the HST have been used to tackle many of the outstanding questions in observational astronomy. This is particularly true in the near-IR with the WFC3, due to the lower sky background levels compared to ground-based observatories and the higher spatial resolution. One of the most successful uses of the WFC3 has been slitless grism spectroscopy, where all sources within the $\sim 2' \times 2'$ field of view have dispersed three-dimensional spectra, which are essentially a series of monochromatic two-dimensional images distributed according to their wavelength on the detector. Spatial as well as spectral information gives insight into e.g. the growth of disks and bulges at high-redshifts (Patel et al. 2013; van Dokkum et al. 2013), the spatial distribution of star formation (Nelson et al. 2012), the regulation star-formation in massive galaxies (Ferreras et al. 2012), and the role of environment and mergers in shaping the galaxy population (Schmidt et al. 2013). Additionally, these surveys are very efficient at covering large areas with a superior multiplexing capacity compared to even the most advanced multi-object spectrographs, allowing for large studies of rare objects such as cold brown dwarfs (Masters et al. 2012) or $4 < z < 7$ Lyman-break and Lyman-α-emitting galaxies (Pirzkal et al. 2004; Rhoads et al. 2009).

For all of its advantages, grism spectroscopic data is difficult to interpret. Contamination from unrelated spectra makes a detailed analysis of individual objects challenging, particularly in crowded fields, and often only sources detected via ancillary imaging are analyzed, somewhat limiting the potential for discovery. As emission lines contain so much astrophysically-interesting information and are the easiest spectral features to detect in faint sources, their detection tends to be the primary focus of grism surveys. Different methods for their discovery have been developed and tuned to the various strengths of the specific set of observations.

Meurer et al. (2007) outline two techniques for finding emission lines in a semi-automated fashion. The first method relies on the detection of sources in the direct image. Each source has its corresponding grism spectrum extracted and emission lines are detected after visual inspection. This is the preferred method of the WISP survey (Atek et al. 2010), a pure-parallel survey using WFC3. There, spectral extractions are performed using the `aXe` software (Kümmel et al. 2009) developed to analyze HST grism data. Most spectra are taken with both the $G102$ and $G141$ grisms, covering an effective wavelength range of $0.8 - 1.7\ \mu$m.

The second method involves searching for emission lines directly in the grism frames. This is done by smoothing the grism frame with a sausage-shaped filter, designed to match the spatial extent of dispersed first-order spectrum, and then subtracting this smoothed image from the original frame. This effectively removes continuum sources from the image while leaving compact features, which can be detected using a simple S/N cut. Undispersed zeroth order spectra from the brightest objects appear as point sources, but their position is well-known and they are easily masked. For each detected feature in this subtracted frame, a cutout of the direct image is inspected to determine which source could have produced the feature. This is the preferred method of the PEARS survey (Straughn et al. 2008; Pirzkal et al. 2013) using the $G800L$ grism of the ACS covering $0.5 - 1.1\ \mu$m. They have the added advantage of having multiple position angles (PAs), such that identification of the source of the emission line in the direct image is simply identifying the area where the different spectral traces for the

same feature overlap.

Both of these methods suffer from the same major issue: potential emission lines may be identified in a semi-automatic fashion, but they always rely on visual inspection for confirmation. In addition, redshifts are only determined in cases where multiple lines are detected. This introduces problems in the subjective nature of line identification as well as preferentially selecting objects in certain redshift ranges, typically where both Hα and [O III] $\lambda\lambda$4959,5007 are visible. Indeed, while the quoted flux limit for compact emission lines in WISP is 5×10^{-17} erg s^{-1} cm^{-2}, which is based on the WFC3 exposure time calculator, these lines are often only detected in objects that have a second, brighter line.

We present here a new method for statistically detecting emission features in grism spectroscopic data, using data from the 3D-HST survey. This program provides WFC3/IR primary and ACS/optical parallel imaging and grism spectroscopy over approximately three-quarters (625 square arcminutes) of the CANDELS fields. We focus here on the WFC3 grism data, which utilizes the $G141$ grism covering 1075 to 1700 nm; reduction and analysis of the ACS $G800L$ grism spectroscopy is the subject of future work.

3D-HST provides us with several advantages over other grism surveys. As the observations are dithered, the processed images offer additional robustness against the effect of hot and bad pixels that a pure-parallel survey cannot. This also provides us with higher spatial resolution and the ability to more easily identify point-like emission sources. We also have the ability to interlace the frames instead of drizzling them, where the pixels from the input images are alternately placed in the output image according to the position of the pixel centers in the original images: see Figure 3 of Brammer et al. (2012a). Interlacing the frames results in better noise characteristics, which is crucial to consider when pushing towards the faint limits of emission line sensitivity; the interlacing procedure will be described fully in Momcheva & Brammer et al. (in prep.).

The remainder of this Chapter is organized as follows. In Section 4.2 we discuss the specifics of the 3D-HST spectroscopic data set. In Section 4.3 we present a new statistical method for detecting emission lines, utilizing more information than traditional methods and resulting in line *probabilities*. In Section 4.4 we discuss the completeness of the sample in terms of the search method itself and the input data and present a sample of high-EW Hα and [O III] emitters in GOODS-S in Section 4.5 . Section 4.6 compares the spectroscopic method with photometric methods (such as the one used in van der Wel et al. 2011). Finally, in Section 4.7, we highlight the potential of this method and the importance of bursty star formation in low-mass galaxies at all redshifts $z \lesssim 3$.

4.2 DATA

The spectroscopic data comes from the aforementioned 3D-HST survey. By design, 3D-HST provides spectroscopy for the five well-studied CANDELS extragalactic fields: AEGIS, COSMOS, GOODS-N, GOODS-S, and UDS. Objects are detected in a combined CANDELS/3D-HST $F125W$+$F140W$+$F160W$ image and multiband photometry is obtained as part of the Skelton et al. (2014) photometric catalog. In the 3D-HST spectroscopic release (Momcheva & Brammer et al. in prep.), these objects have extracted 2D

grism spectra.

A model for the grism spectra of the entire field is created as follows. For a given object, we distribute the light (and consequently the extraction weight in the spatial direction) uniformly as a flat spectrum according to the profile of the object using the F160W "postage stamp" image of the object itself to ensure it has the correct extent and structure. Next, for bright objects we fit the slope of the continuum in the first iteration of the spectra and convolve the slope with the postage stamp image for the second iteration.

Creating a continuum model individually for all objects allows us to construct a model of the flux distribution for the entire field. This is useful because of spectral confusion due to overlapping unassociated spectra in the grism data. Since we create the full modeled spectra for each pointing, each extracted 2D spectrum has the modeled spectra from surrounding objects ("contamination") subtracted. As our primary interest is emission features, its own continuum ("model") is subtracted as well. For the brightest objects, the model does not always subtract cleanly and can lead to spurious detections in neighboring objects, so we also mask any "contamination" regions above a flux of 0.004 electrons s^{-1}: see Section 4.4.3.

4.3 SIMPLE MODEL FITTING OF EMISSION LINES IN 3D-HST

Every object in the Skelton et al. (2014) photometric catalog has a grism spectrum (S') and a direct $F125W$+$F140W$+$F160W$-combined postage stamp (I). As described above, each grism spectrum also has a flat continuum flux model and a flux model for all overlapping spectra. We therefore subtract these models from S' to obtain a spectrum S in which we search for residual emission features. In order to avoid correlating noise with noise, we apply a signal-to-noise cut to I of 2σ above the background level. If the image has fewer than 20 pixels above this threshold, then we instead use the HST $F140W$ PSF scaled to the same flux as the image: an area of 20 (interlaced) pixels is approximately the size of a native WFC3/IR pixel. We perform a cross correlation of I with S according to:

$$\ln \mathscr{L}(\{S\}|A, \Delta x) = -\frac{1}{2} \sum_{x=0}^{x_{max}} \sum_{y=0}^{y_{max}} \frac{(S_m(x, y|A) - S(x + \Delta x, y))^2}{\sigma_S^2(x + \Delta x, y)}, \tag{4.1}$$

where x_{max} and y_{max} are the dimensions of the postage stamp I and $S_m(x, y|A) = A \times I(x, y)$. The parameter A is a scaling factor, ranging from 0 to 1. At a given position, $A = 0$ implies that there is no signal present in the spectrum. Conversely, $A = 1$ corresponds to a position where the entire flux[1] of the galaxy is contained in a single emission feature with the same spatial extent as the direct image and is unresolved spectrally ($R_{G141} = 130$). As we are dealing with three-dimensional spectra, Δx is a pixel offset between I and S in the dispersion direction: both have the same extent in the y-direction, so Δx represents correlating I with different positions in S relative to the spectral dispersion

[1]The spectral range of the $F125W$+$F140W$+$F160W$ filter combination overlaps with the $G141$ grism such that those filters cover a slightly larger wavelength range than the grism.

direction, $\hat{x}$ in pixel space or $\hat{\lambda}$ in wavelength space. We calculate the likelihood at each integer value of Δx, noting that the FWHM of the WFC3 PSF is 1.1 pixels at 1.4 μm.

We do not know *a priori* if a given spectrum contains a spectral feature or not. We have no clear preference for position of any possible feature in a given spectrum (unless we have photometric redshift information, see Section 4.3.1). If we assume that each spectrum has a single emission line at a single position, the probability of that line being at a given position is $p_{prior}(\Delta x) = x_{max}/\Delta x_{max}$, corresponding to the area of the spectrum probed in each step. Therefore, the probability that there is *no* line at the position is $(1 - p_{prior}(\Delta x)) \times \delta(0)$ where $\delta(0)$ is the Kronecker delta function. Likewise, we assume no intrinsic knowledge of the distribution of relative line fluxes in the sample, so $p_{prior}(A)$ is flat in [0,1] and normalized such that:

$$\int_{-\infty}^{\infty} p_{prior}(A) dA = 1. \tag{4.2}$$

Combining the two priors on A and Δx together, we arrive at:

$$p_{prior}(A|\Delta x) = (1 - p_{prior}(\Delta x)) \times \delta(0) + p_{prior}(\Delta x) \times p_{prior}(A). \tag{4.3}$$

Bayes's Theorem states that

$$p_{posterior}(A|\{S\}, \Delta x) \propto p_L(\{S\}|A, \Delta x) \times p_{prior}(A|\Delta x), \tag{4.4}$$

where $p_{posterior}(A|\{S\}, \Delta x)$ is then the probability distribution of A at a single position Δx. Ultimately, we want to determine the probability that there is a line which has a significant detection at a given position. To do this, we marginalize $p_{posterior}$ over A according to:

$$p(A > 0|\{S\}, \Delta x) = \int_{>0}^{1} p_{posterior}(A|\{S\}, \Delta x) dA. \tag{4.5}$$

If there are no strong features, $p_{posterior}(A|\{S\}, \Delta x)$ is maximum at $A = 0$ for all spectral positions Δx. If no positions have $p(A > 0|\{S\}, \Delta x) > 0.997$ (i.e. a "3σ" detection assuming Gaussian statistics), then we conclude that there are no emission lines in the spectrum.

If a single position Δx meets the threshold, then we simply translate it into a wavelength λ, a single value of A which can be transformed into a line flux in physical units, and an uncertainty on that flux given the distribution of $p_{posterior}(A|\{S\}, \Delta x)$. However, given that we are dealing with three-dimensional spectra, a bright emission line in an object that is not a point source produces significant detections of A at positions near the intrinsic $\lambda_{central}$. Our best estimate of the central line position is the "significant" pixel responsible for the maximum peak in $p_{posterior}(A|\{S\})$. If the probability is maximized for a value A significantly greater than 1 (i.e. a "line" that is 3σ consistent with having a flux greater than the total flux of the galaxy), we consider the line to be a spurious contaminant and reject it (see Section 4.4.3).

4.3.1 Photometric Priors

Given the amount of ancillary photometry in the 3D-HST/CANDELS fields, spanning from X-ray to radio wavelengths, it is straightforward to estimate the redshifts photo-

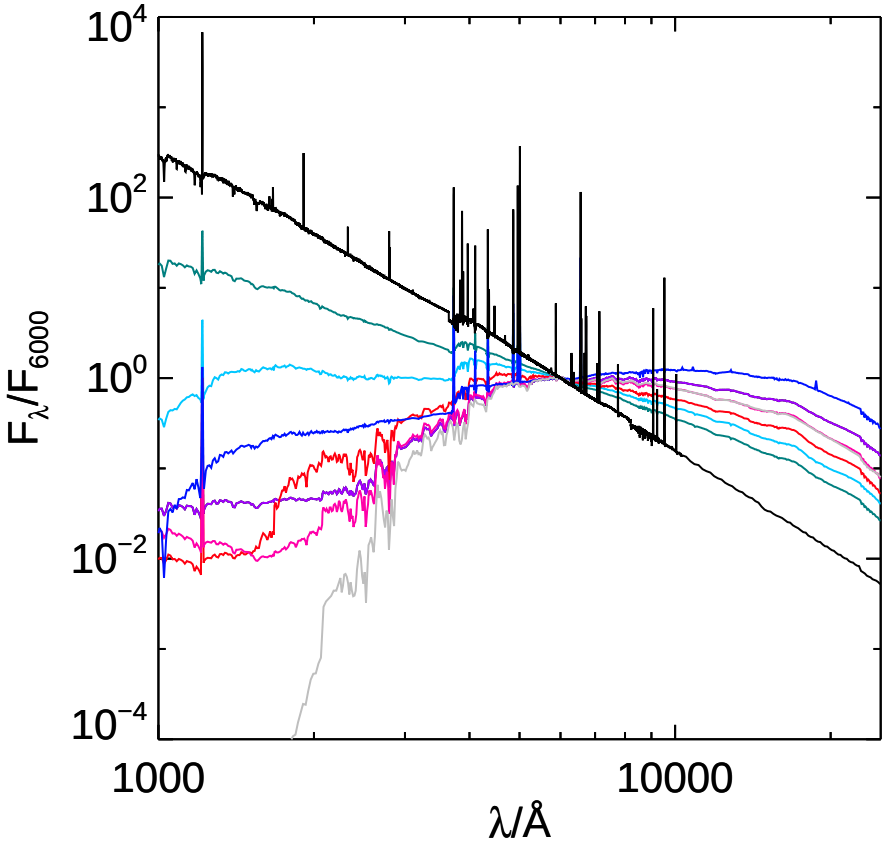

FIGURE 4.1: *Photometric templates used in our application of* `EAZY` *(Brammer et al. 2008) normalized at 6000 Å. The colored templates are the default* `EAZY` *set, created following the Blanton & Roweis (2007) algorithm with PÉGASE models (Fioc & Rocca-Volmerange 1997) and a calibration set of synthetic photometry derived from semi-analytic models, while the black and gray templates are an EELG (from Chapter 3) and a 1.5 Gyr Bruzual & Charlot (2003) SSP with* $A_V = 2.5$ *to fully reproduce the SEDs of the bluest and reddest objects in the sample. All galaxy SEDs are fit with linear combinations of these templates.*

metrically for the sample (a full description is given in Brammer et al. 2012a). Briefly, we calculate photometric redshifts by applying `EAZY` (Brammer et al. 2008), which calculates model fluxes by convolving linear combinations of high-resolution spectral templates with the filter transmission curves, to the broadband SEDs in order to estimate a probability distribution for the redshift, $P(z)$ (see the top panel of Figure 4.2). Here we use the default `EAZY` template sets plus an additional dusty starforming template (a Bruzual & Charlot 2003 SSP of 1.5 Gyr and $A_V = 2.5$) and an EELG template (the highest sSFR galaxy from Chapter 3: UDS-6195), as shown in Figure 4.1. We choose to use this $P(z)$ distribution in cases when the minimum reduced-χ^2 value is less than 5, which happens in ~90% of the cases, otherwise we adopt a flat $P(z)$ prior.

For a line detection in a given spectrum, we do not know which restframe emission feature it corresponds to. The strongest (blended) emission line complexes we expect to typically observe are Paβ λ12820, He I λ10830, [S III] λ9530, Hα λ6563, [O III] $\lambda\lambda$5007,4861, [O II] $\lambda\lambda$3727,3729, and Mg II λ2800. This implies that we are only search-

ing for sources with $z \lesssim 5.1$[2]. We convolve the redshift prior $P(z)$ with the restframe wavelengths of these emission lines to determine a prior probability of a line detection as a function of observed wavelength. At each wavelength within the $G141$ grism coverage, we determine the probability of a line being present at that wavelength $P(\lambda)$ as the combined value of the individual line probability distributions at that position. Examples are shown in Figure 4.2 and 4.3. As noted in Skelton et al. (2014), there are indeed some cases in which the photometric redshift for a given object varies greatly from its spectroscopic redshift. This (small) percentage varies from field to field and is likely a function of magnitude, so we adopt a floor in our probability distribution such that only 98% of the total probability is allocated according to the photometric prior and distribute the remaining 2% uniformly across all observed wavelengths.

4.3.2 Redshifts

The main quantity of interest is the restframe equivalent width of the emission lines. As such, for every measured emission line, we must determine the redshift of the galaxy. The 3D-HST photometric catalog contains ground-based spectroscopic redshifts for 6,141 objects from a variety of sources (see Section 5.1 in Skelton et al. 2014). In the case that an object with a detected line has a corresponding spectroscopic redshift and no detected emission line in the grism, we utilize the ground-based measurement.

We iteratively assume that the strongest detected line in the grism is Paβ, He I, [S III], Hα, [O III], [O II], and Mg II and look for significant detections at the predicted positions of the other emission lines. If we have a significant detection(s) at the predicted position(s), then we have a secure redshift determination. In the case where we do not find a significant additional emission line, we identify the detected line according to the highest probability for a given line species at that wavelength position according to the photometric redshift information. In cases where we have no photometric redshift prior or do not use one because of a large reduced-χ^2 value, we exclude the line from the final sample.

As a final check, we visually inspect all detected lines to verify that the detection is not caused by severe contamination or artifacts at the very edges of the detector[3]: see Section 4.4.3. Only lines with unambiguous determinations via multiple line detections or single line detections that agree with the photometric redshift prior are considered further. In Figure 4.4, we compare some of our redshifts with published ground-based spectroscopic redshifts as described in (Skelton et al. 2014). A vast majority of the objects have consistent redshifts between the two methods, with the differences primarily caused by differing line identifications. We would like to point out that ground-based spectroscopic redshifts are not always reliable, given that they suffer from similar issues with line identification in the case where only a single line is detected. As we include photometric priors and therefore *probabilistically* identify the line, we argue that our method produces reliable redshifts.

[2]This is the redshift where we lose Mg II from the grism coverage. For the photometric redshifts, `EAZY` is run with $z < 6$. A search for higher redshift restframe-UV emission lines in this grism data is the subject of ongoing work.

[3]We do not intend to visually verify the existence of the line or not. Visual searches for emission lines are highly subjective and run counter to the main aim of applying the Bayesian framework.

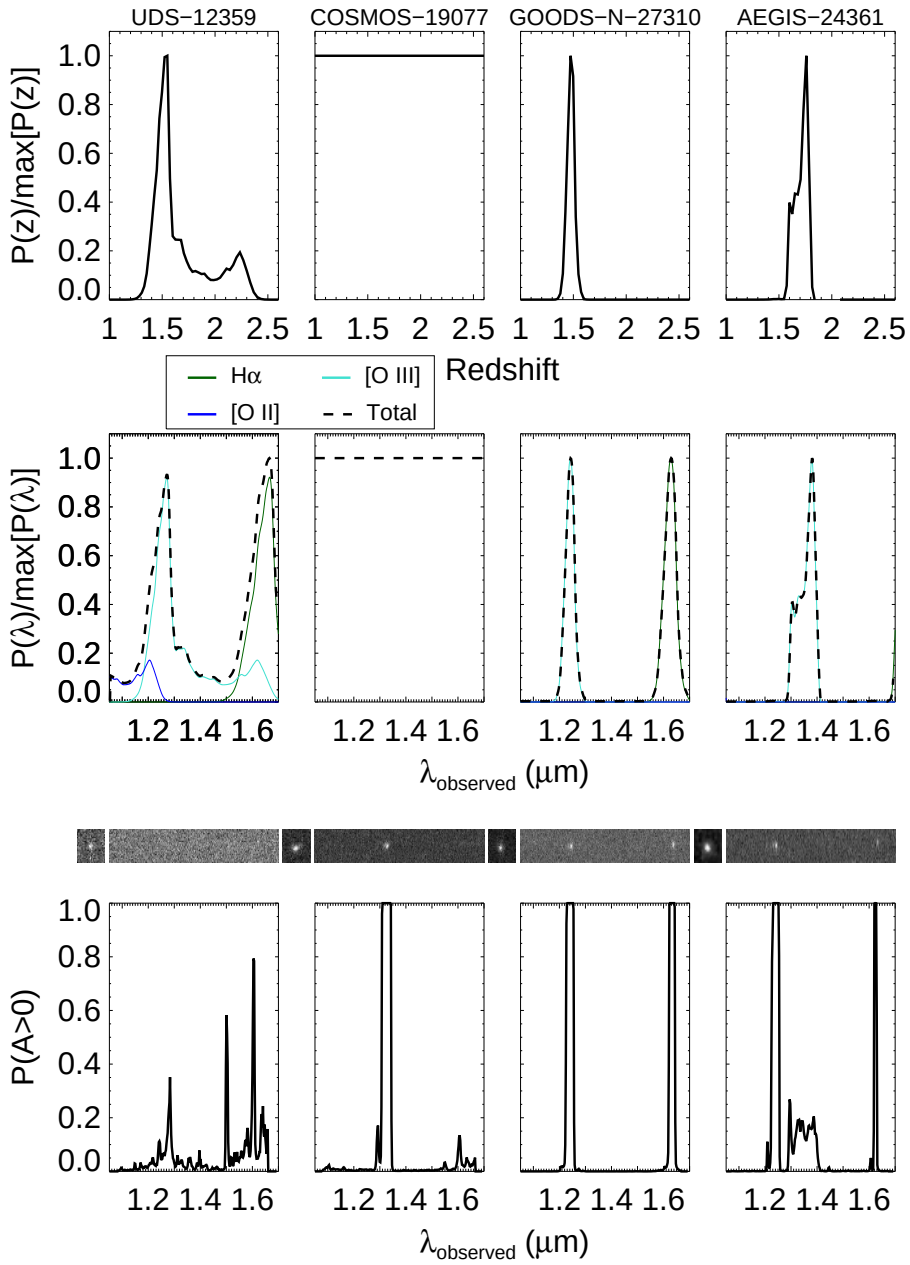

FIGURE 4.2: *Illustration of the line search process for (left to right) UDS-12359, COSMOS-19077, GOODS-N-27310, and AEGIS-24361. From top to bottom: photometric redshift probability distribution from* `EAZY` *($P(z)$; Brammer et al. 2008), the prior on line positions $P(\lambda)$ derived from $P(z)$ for lines in the correct observed wavelength range, the direct (undispersed) and grism images for the objects, and the output probability at each wavelength position Δx that A is nonzero. The colored curves denote the expected positions of Hα λ6563, [O III] λλ5007,4959 given $P(z)$, while the black curve denotes the overall $P(\lambda)$ for all emission lines that could fall in the grism coverage. Note that in this case Mg II, [O II], [S III], He I, and Paβ do not appreciably contribute any probability for these objects in this observed wavelength range. In the case of UDS-12359, no significant ($> 3\sigma$) line detections are found. For COSMOS-19077 (one of the objects studied in Chapters 2 and 3), a strong line is discovered despite assuming a flat $P(\lambda)$ due to a high-χ^2* `EAZY` *fit; this object's redshift cannot be reliably determined and is therefore excluded. For GOODS-N-27310, the $P(z)$ correctly predicts the positions of the emission lines. For AEGIS-24361, the lines are slightly offset from the predicted position (although we detect and identify them regardless).*

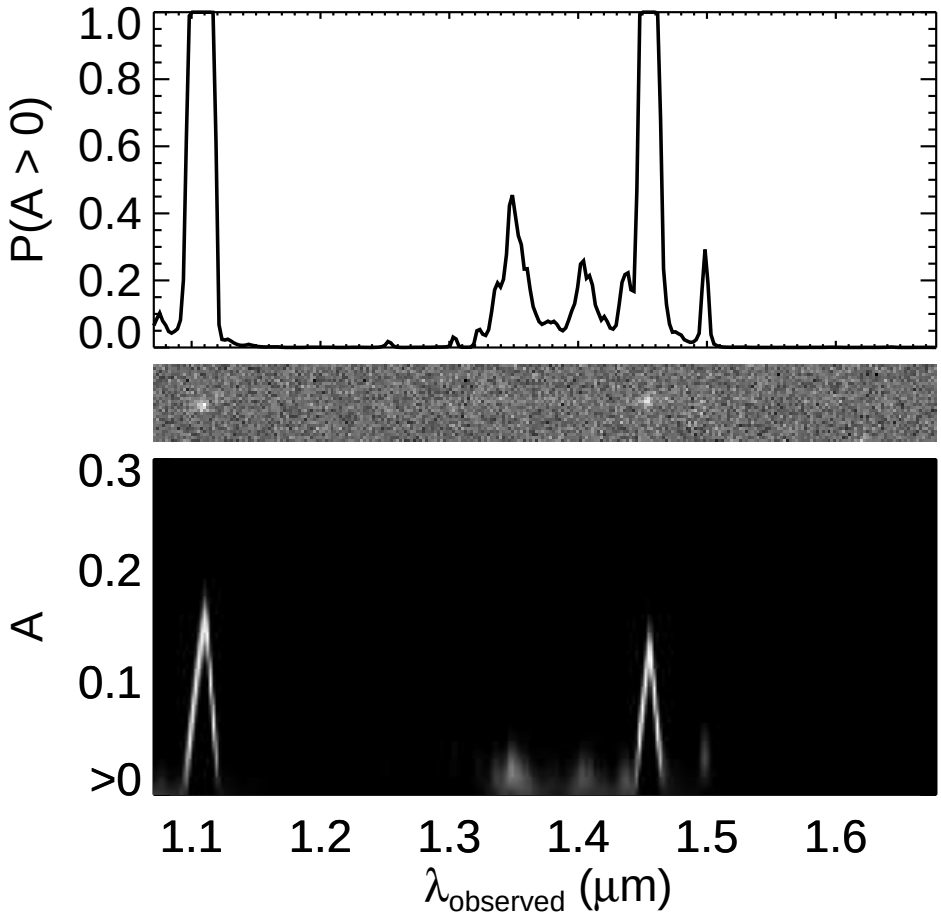

FIGURE 4.3: *Illustration of Equation 4.5 for GOODS-S-38590. The bottom panel illustrates the two-dimensional probability array* $p_{posterior}(A|\{S\},\Delta x)$ *with the color coding ranging from black (zero probability) to white (high probability). By marginalizing this probability distribution over all nonzero values of A, we arrive at the top panel, which is the same as the bottom set of panels in Figure 4.2. The object's G*141 *spectrum is shown in the middle panel.*

4.4 COMPLETENESS OF THE SAMPLE

While grism spectroscopy hypothetically allows us to search for emission lines in an unbiased manner, several important issues affect our search completeness.

4.4.1 LINE DETECTION LIMITS

The primary test of the efficacy of this method is to insert fake emission lines into spectra and attempt to recover them. In order to do this, we identify a control sample of 1425 "blank" spectra representing a variety of galaxy sizes and morphologies, where our search method does not return any pixel positions with a significant detection. We

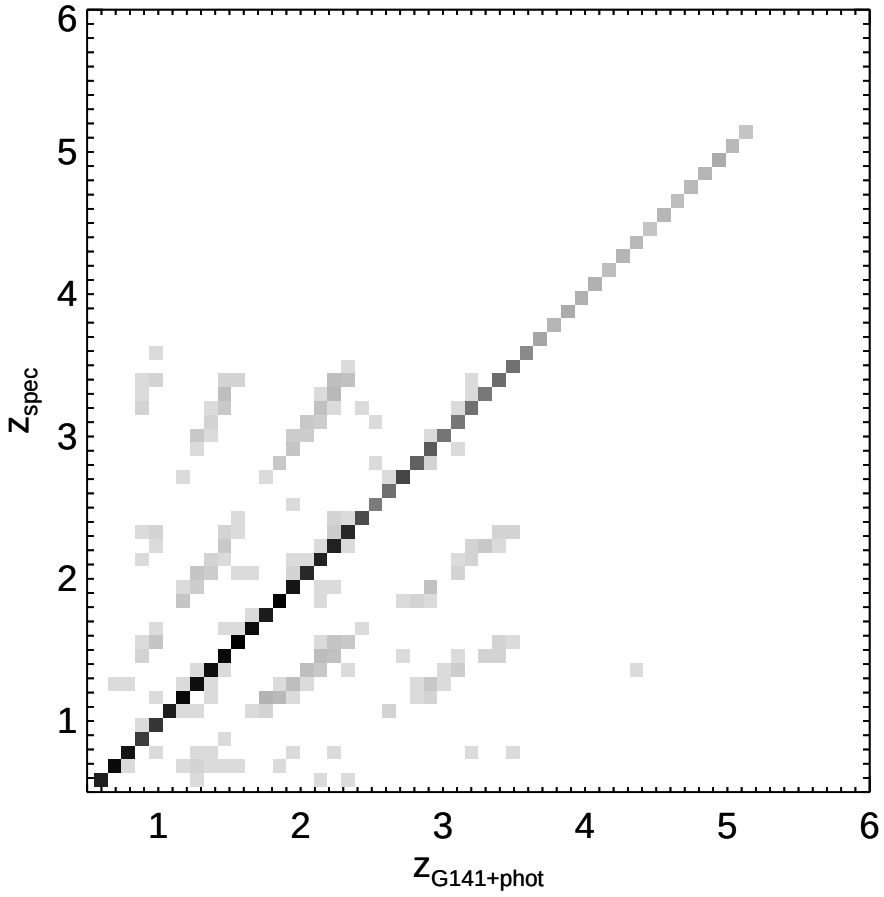

FIGURE 4.4: *Comparison of our redshift determination to ground-based spectroscopic measurements as described in (Skelton et al. 2014). The color of the bin denotes the relative number of objects within the bin, and the scale has been stretched for clarity. There is very good one-to-one agreement for most objects. Outlying points are typically due to a difference in line identification (the linear structures visible above and below the 1:1 line), with assistance in this sample contributed by photometric redshift information.*

insert a fake emission line at 1.4 μm which is simply the direct image of the object scaled to a given flux value. We then run our search algorithm, focusing on a ± 7 pixel region around 1.4 μm (roughly the average physical extent of a galaxy in this sample) to see how many lines are recovered as a function of the scaled flux value. In addition, previous work from 3D-HST has shown that typical starforming galaxies have star formation (as traced by Hα emission) out to ~ 30% larger radii than the rest-frame *R*-band stellar continuum (Nelson et al. 2012). We also repeat this test making the artificial emission line 30% larger at the same integrated flux value.

The results of this test are shown in Figure 4.5. At 90% completeness, we find a flux limit of 7.4×10^{-18} erg s^{-1} cm^{-2} for the compact line case and 1.1×10^{-17} erg s^{-1} cm^{-2} for the extended line case. When we insert an artificial line with the spatial extent of the F140W PSF we obtain a detection limit of 3.7×10^{-18} erg s^{-1} cm^{-2}. The 3σ completeness limit for this PSF test is 3.4×10^{-17} erg s^{-1} cm^{-2}, which is comparable to the theoretical point-source calculation for this pointing (*GOODS-S-34*) with t_{exp} = 1103 *s* and an aperture radius of 3 pixels (0.39″) of 3.1×10^{-17} erg s^{-1} cm^{-2} (Brammer et al.

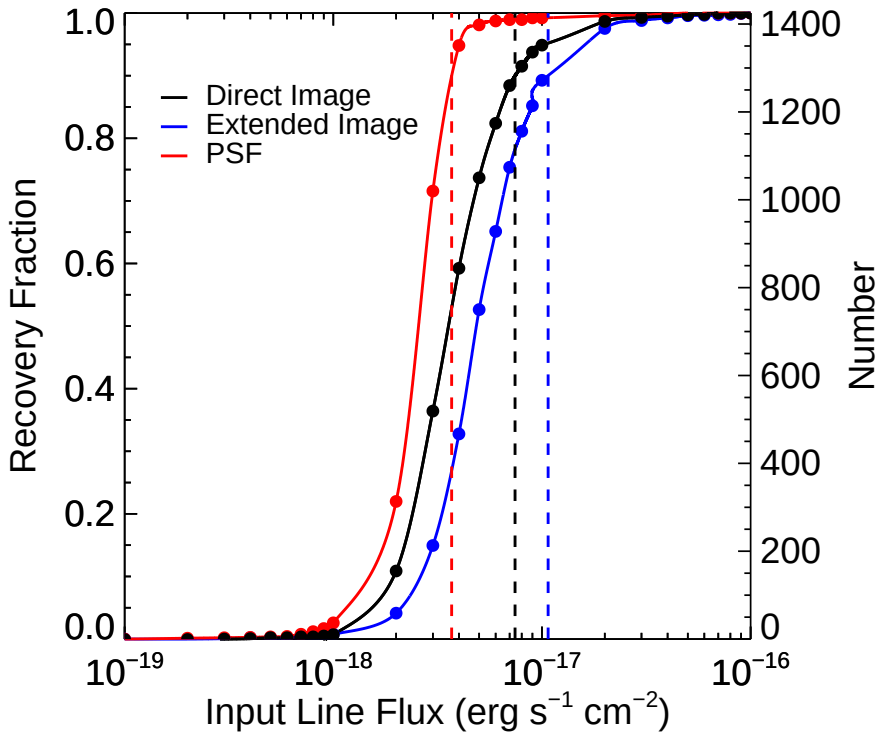

FIGURE 4.5: *Completeness of line recovery test as a function of the fake emission line flux, inserted at 1.4 μm. Black denotes an emission line with the same profile as the direct image, blue denote an emission line that is 1.3 times larger (Nelson et al. 2012), and red denotes an emission line the size of the F140W PSF. At 90% completeness, we find flux limits of 7.4×10^{-18} erg s^{-1} cm^{-2}, 1.1×10^{-17} erg s^{-1} cm^{-2}, and 3.7×10^{-18} erg s^{-1} cm^{-2}, with vertical dashed lines denoting these limits.*

2012a). Grism line searches such as these are primarily sensitive to surface brightness. When we enlarge *all* emission lines by 30%, we decrease the surface brightness of all galaxies at a given flux and hence we become less sensitive.

Line sensitivity will also vary by wavelength, according to the throughput of the grism. We have performed all of these tests at 1.4 μm, close to the center of the *G*141 grism. The true sensitivity of our method at a given wavelength, then, is the above-quoted line sensitivity scaled according the ratio of the 1.4 μm throughput to the throughput at the observed wavelength, see Figure 4.6.

4.4.2 FALSE POSITIVES

While the above test determines the flux limit at which an emission line is likely to be recovered, it does not inform us how often a noise peak or artifact would be detected significantly. In order to investigate this, we isolate regions of the grism pointing that do not have any flux from the continuum model for each field and create artificial 2D extractions, each 284×11 pixels in size. As these regions are unlikely to contain real spectral information, any peaks represent noise, unmodeled contamination, or detector

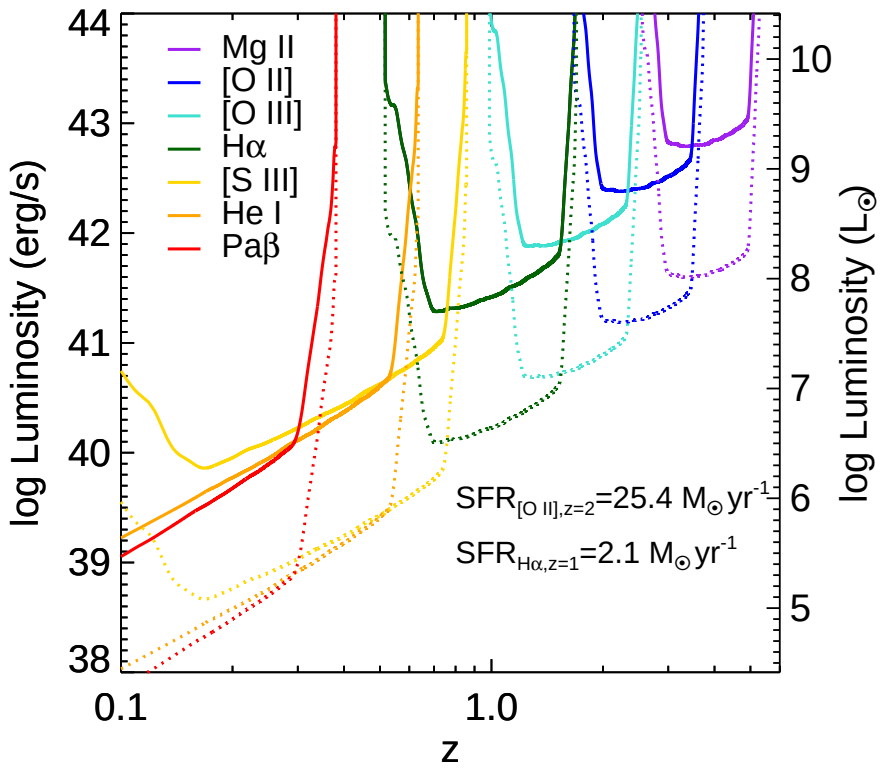

FIGURE 4.6: *Line luminosity at our 3σ completeness limit as a function of line species and redshift (dashed lines denote the luminosities at the 50% completeness limit). SFRs come from the calibrations of Kennicutt (1998).*

artifacts. We search for point source "false positives" by performing our standard cross-correlation analysis with an image of the F140W PSF. Each spectrum is assigned 100 random photometric redshift priors, drawn from the full set of real redshift priors for each field, and the search is performed 100 times. Any detections are visually classified in the same way as the real spectra such that obvious cases of un-modeled continuum or individual hot pixels[4] are rejected.

Overall, 1,195 artificial spectra across all five fields are created and fit in this way. Of the 119,500 individual realizations, 7,882 (6.6%) yielded plausible $> 3\sigma$ detections (see Figure 4.7) for all line species and line fluxes. The number of false positives varies as a function of line flux, as not all cosmetic features and noise peaks are of the same magnitude. There tend to be more bright sources of contamination than faint sources as this also incorporates the same flux completeness as shown in Figure 4.5. As this number is higher than for purely Gaussian noise, we conclude that the grism exposures contain significant amounts of correlated noise and artifacts that mimic emission features, also due to un-modeled or under-predicted spectral contamination. Many of our sources are not point-like but extended, particularly in bright sources that have bright emission lines, and thus the chances of correlated noise contributing to a significant detection are actually less than this. Such a test, then, represents the maximal contamination to the sample for the faintest objects. Additional criteria are applied to

[4] A single bright pixel in the interlaced frame corresponds to a single bright pixel in a single exposure and therefore cannot be caused by an emission line, which should appear in all four raw exposures.

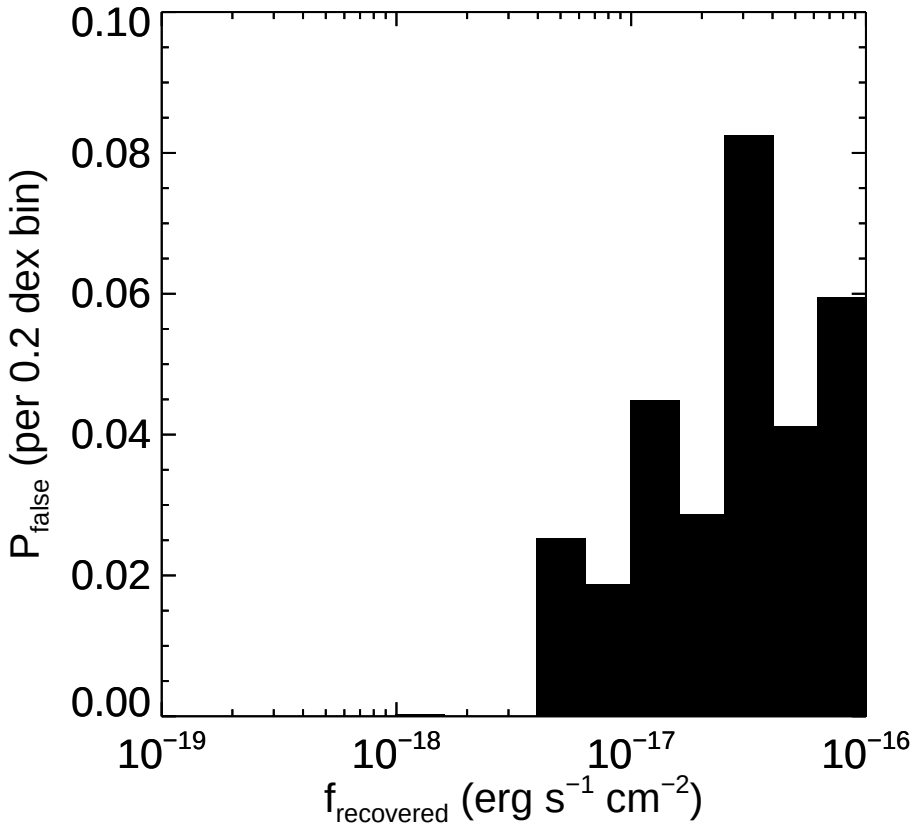

FIGURE 4.7: *Histogram of recovered line fluxes for "blank" spectra as part of the search for false positives. In 0.2 dex wide bins of recovered line flux, we plot the probability that a line with a measured flux is due to a spurious feature. For the full range in fluxes, redshifts, and equivalent widths, this corresponds to 6.6%. As noted in the text, a majority of real sources have more spatial information that this, as the test was performed using the PSF, and thus the true P_{false} should be lower than this for all fluxes. The lack of false detections below $3{\times}10^{-18}$ erg s^{-1} cm^{-2} is due to the additional line completeness limits shown in Figure 4.5. Overall, the contribution of false positives to the emission line sample is low but not negligible.*

create useful samples (e.g. a cut on EW as in Section 4.5), and thus true contamination levels are even lower than this.

4.4.3 CONTAMINATION

Due to the slitless nature of grism spectroscopy, some sources are strongly contaminated by overlapping spectra from brighter sources. Chance alignment of sources in the direct image could result in both having "detections" of the same emission line in the grism data, especially if both sources are spatially small. There is no automated way to account for such events, so we must resort to visual inspection: for all objects with detected emission lines, we search for all other objects with detected emission lines that lie in a rectangular aperture with an extent corresponding to the *G*141 dispersion size (284 interlaced pixels). If multiple sources "produce" the same emission line, we assign the line to a single source based on the overlap with the expected trace of the source

(a direct overlap as opposed to a glancing one), the $F140W$ morphology of the sources, and the plausibility of the implied EW for each source.

As described in Section 4.2 and Momcheva & Brammer et al. (in prep), we have a sophisticated flux model for each object in a pointing. The modeled flux for neighboring sources is subtracted when searching for emission lines in an object's spectrum to avoid potential false detections. Each object's own flux distribution is also subtracted: the flat flux distribution represents the continuum level of an object, which needs to be subtracted in order to discover residual emission lines.

The model, however, occasionally does not subtract perfectly and we are left with residual flux. This typically scales with the actual flux level, such that brighter regions tend to have larger residuals. Regions of positive residual ($S'-Model$) appear like spectral features in that they are areas of "real" flux above the background level. These regions are identified as emission features, both in the (bright) object that created the original spectrum and in spectra of objects that happen to overlap with them. In order to avoid this, we set a flux level in the model and mask any pixels above it. We seek to strike a balance between masking as few pixels as possible, maximizing our search area, and minimizing the chance of contamination leading to false detections. We select this masking level by studying the differential number of faint lines detected with increasing masking level. The number of detections below $2.5{\times}10^{-18}$ erg s^{-1} cm^{-2} is nearly zero for increasing masking levels until 0.004 e$^-$ s^{-1}, where we see $3{\times}10^{-7}$ pixel^{-1}. This threshold thus results in the largest usable area while still detecting some lines where we should be ~10% complete.

The primary issue for contamination from overlapping spectra, then, comes from the limited area in which we search for lines after applying this masking. The total unusable area depends on the specific pointing in question, but is equal to 18% when averaged over the whole survey area with a standard deviation of 4.1%. There are some specific cases in which the model fails to account for a particularly bright spectrum, typically in higher-orders for bright stars, and we are left with "uncontaminated" regions of residual flux. These cases are obvious to identify and are the reason why all objects with detections are visually inspected.

4.4.4 COMPLETENESS OF THE PHOTOMETRIC CATALOG

This starting point of this search is the photometric catalog of Skelton et al. (2014). Therefore we do not analyze spectra for sources that are not in the input photometric catalog.

In the left panel of Figure 4.8, we show the completeness fraction of the photometric catalog as a function of line flux and equivalent width, assuming a single emission line is placed in the H_{F160W} filter. This is the emission line version of Figure 14 in Skelton et al. (2014). The 90% catalog completeness limit is $H_{F160W} = 25.1$, which corresponds to an emission line flux of $\sim 10^{-16}$ erg s^{-1} cm^{-2} if entirely concentrated in a single line of infinite equivalent width. Note that for a given line flux we are more likely to have the object in the photometric catalog if it has a *lower* equivalent width, as that implies the continuum level is higher.

The requirement that an object must be in the photometric catalog is the single

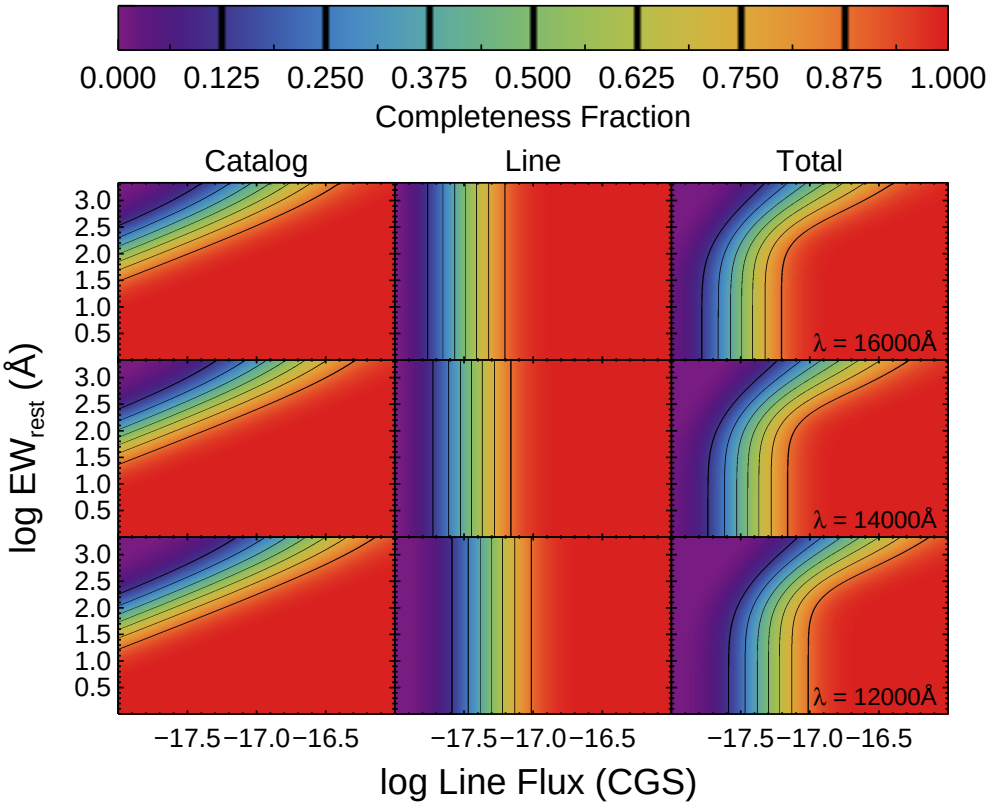

FIGURE 4.8: *Completeness fraction as a function of line flux and equivalent width at fixed line positions (12,000 Å, 14,000 Å, and 16,000 Å). The left panels show the completeness of the Skelton et al. (2014) photometric catalog for objects of a given flux and equivalent width (i.e. continuum magnitude), the central panels show the flux completeness of our line search from Figure 4.5 and the G141 sensitivity at that position, and the right panels show the combination of these two completeness functions. These wavelengths correspond to Hα at z = 0.83, 1.1, and 1.4 or [O III] at z = 1.4, 1.8, and 2.2.*

strongest prior we apply to our data. If an emission line source is not in that catalog, by definition we will not be able to detect the line. In the range of fluxes where we can still robustly detect lines, our catalog completeness is approximately 60% for high-EW sources.

4.5 Hα AND [O III] EMITTERS IN GOODS-S

A full catalog of emission lines for 3D-HST galaxies will be presented in the future, utilizing a deeper photometric catalog to overcome the issues mentioned in Section 4.4.4. Here, we focus on the subsample of EELGs from $0.7 < z < 2.3$ in GOODS-S with restframe-optical emission line EWs in excess of 250 Å. This redshift range represents a span of more than 4 Gyr of cosmic time, and hence we must be careful to isolate galaxies in similar evolutionary phases. GOODS-S is chosen here as it has the deepest overall near-IR imaging and therefore suffers the least from catalog completeness issues.

For a given observed line flux, we observe an intrinsically more luminous source at higher redshifts. In order to make a fair comparison between [O III] emitters and Hα emitters at different redshifts, we apply a luminosity limit corresponding to the luminosity of a line at the 90% flux completeness of the search located at the maximum redshift in the bin. This is done for two bins in Hα redshift and two bins in [O III]. As a result, we have 175 Hα emitters and 198 [O III] emitters above our EW limit in GOODS-S, shown in Figure 4.9, each split into two redshift bins. Using the results from Section 4.4.2 and applying the same criteria that $EW_{H\alpha/[OIII]} > 250$ Å, we estimate an upper limit on the contamination of 1.4%. Again, this contamination fraction is an upper limit given the additional spatial information for many of the objects in this sample.

In order to interpret the evolution in the number density, we need to identify a sample at lower redshifts as well. Narrow-band imaging surveys, where fluxes between overlapping narrow-band and broad-band filters are compared to determine a flux excess at a specific wavelength position, can also be used to isolate high-EW sources. One such survey is HiZELS, the High-redshift(Z) Emission Line Survey (Geach et al. 2008; Sobral et al. 2009). HiZELS primarily targets Hα at z =0.40, 0.84, 1.47, and 2.23 via narrow-band filters at 0.921, 1.21, 1.62, and 2.12 μm (*NB921, NBJ, NBH,* and *NBK*), since Hα traces star formation activity and is well calibrated at these redshifts (Sobral et al. 2012, 2013). However, the depth of the imaging varies by band and is typically much shallower in terms of observed line luminosities than the CANDELS imaging. The only observations that are deep enough to be a useful comparison, then, are the *NB*921 observations of Hα at $z = 0.40$. Similarly, the aforementioned PEARS survey uses the ACS *G*800*L* grism covering 0.5 – 1.1 μm or [O III] at $z < 1$ and Hα at $z < 0.7$. PEARS uses the same HST/ACS optical photometry as CANDELS, and thus we can use the catalogs from Pirzkal et al. (2013) directly.

The resulting comoving number density evolution is shown in Figure 4.9. Clearly the number density of high-EW sources increases with increasing redshift. Compared to the $z \sim 0.3$ data from PEARS, high-EW [O III] emitters are more than an order of magnitude more common at $z \sim 2.1$. This is in line with the claim made in van der Wel et al. (2011) compared to "green peas" and here we also see agreement with their resulting number density of $3.7{\times}10^{-4}$ Mpc^{-3} for $EW_{[OIII]} \gtrsim 500$ Å at $z \sim 1.7$. We also note that the number densities from PEARS are even higher than those in the very local universe, which is not probed as a part of that survey. Interestingly, the shape of the evolution matches the shape in the cosmic star formation rate density evolution (Karim et al. 2011), even though that is mostly affected by more massive $L^\star$ galaxies. This implies a consistency between EELGs and typical star forming galaxies at these epochs, namely galaxies on the aforementioned main sequence of star formation. There, the scatter in the relationship is too small to to be described by major merger evens, with too large of an enhancement in a galaxy's SFR over too short of a period of time (e.g. Lotz et al. 2010). Thus, the matching evolution intimates that EELGs are also not closely related with major merging events, but rather are "normal" episodes in the star formation histories of low-mass galaxies at these redshifts.

4.6 FIDELITY OF PHOTOMETRIC SEARCHES

The photometric selection technique of van der Wel et al. (2011) utilizes the I_{F814W}-, J_{F125W}-, and H_{F160W}-bands to preferentially select systems dominated by strong emis-

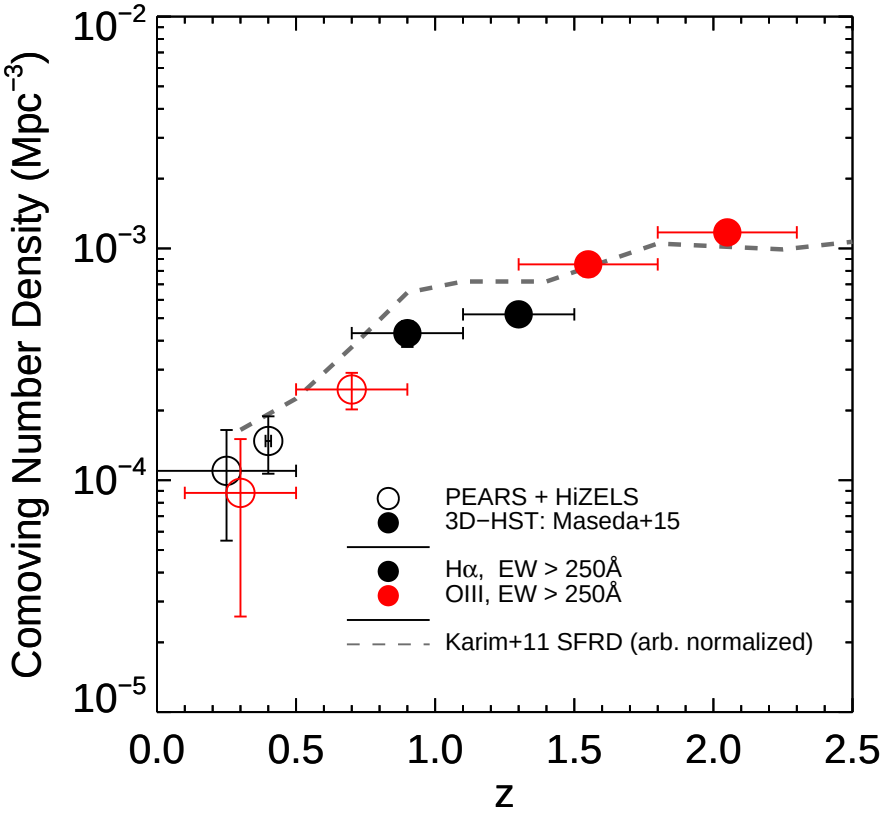

Figure 4.9: *Comoving number densities as a function of redshift for objects in GOODS-S with restframe [O III] (red) and/or Hα (black) EWs in excess of 250 Å from HiZELS (Geach et al. 2008; Sobral et al. 2009), PEARS (Pirzkal et al. 2013), and this study. Error bars in redshift represent the actual redshift range in each bin and not uncertainties in the redshift determination; see Section 4.3.2 for more information about the redshift determination in this study. The evolution in this number density roughly follows the evolution in the cosmic star formation rate density as determined by Karim et al. (2011), underlining the importance of this mode of star formation.*

sion lines. By looking for a flux excess in J compared to the continuum as measured in I and H, they claim to select [O III] emitters at $1.6 < z < 1.8$, with perhaps minor contamination by Hα emitters at z~1. We now have complete CANDELS photometry and 3D-HST grism spectroscopy for the full van der Wel et al. (2011) sample. Of the 69 objects, we confirm here that 61 of them are indeed high-EW line emitters. Of the remaining eight objects, four have contaminated spectra and thus we cannot reliably determine their redshifts and four are confirmed to not have an emission line in the wavelength range, with contaminated photometry causing the sources to have an erroneous J-band excess.

Another photometric selection is given in Cardamone et al. (2009) for lower-redshift emission line galaxies, the so-called "green pea" galaxies. While the same selections could yield a sizable sample in our data set, we would not detect the strongest emission lines (Hα or [O III]) in the NIR for them given their low redshifts.

Overall, then, we conclude that photometric searches can yield relatively pure samples of EELGs, albeit in limited redshift windows. In fact, the $i - J$ and $J - H$ colors

of an EELG (for a typical EELG like *GOODS-S-30308*, this difference is 0.9 magnitudes) are the furthest apart at $z \sim 1.7$ than any other HST-based colors at $1 < z < 3$, with the added advantage of low contamination from other sources. Such a photometric cut will be crucial in future EELG studies given the large areas of imaging (all of these bands are also available from the ground, with minimal effects on the colors) and the relative lack of spectroscopy in many areas of the sky.

4.7 CONCLUDING REMARKS

This method, while specifically applied to HST grism spectroscopy, is more generally applicable to any spectroscopy with spatial as well as spectral information. The additional information reduces the number of false positives, resulting in a purer sample. The statistical nature of the method results in probabilities of any given position containing an emission feature, incorporating additional information than a traditional S/N selection would. By applying this method to large data sets, we can obtain large numbers of robust emission line strengths and redshifts, particularly when incorporating photometric redshift priors.

The method is applied to the 3D-HST coverage of the GOODS-S field to mitigate potential effects from incompleteness in the input photometric catalog, and a complete sample of Hα and [O III] emitters is presented. The comoving number density evolution is measured at these redshifts and compared to more local samples. *EELGs, which represent bursty star formation in dwarf galaxies (see Chapters 2 and 3), are determined to be a crucial channel in the buildup of stellar mass in today's dwarf galaxies.* As the evolution mimics that in the cosmic star formation rate density (Karim et al. 2011), we have a tantalizing hint that the EELGs show a mode of star formation consistent with that of normal $L^\star$ galaxies, namely that the EELGs are also not triggered by major mergers. They must therefore represent a common phase in the stellar mass buildup of dwarf galaxies at these redshifts. It remains to be seen, though, if this process continues at even higher redshifts ($z \gtrsim 3$), where low-mass galaxies must also deal with stronger ionizing radiation from the cosmic UV-background (Babul & Rees 1992; Babul & Ferguson 1996). Future observations and detailed simulations will be able to discern if this bursty mode of star formation is important in the early histories of galaxies in the early universe.

This methodology will be extended to the full 3D-HST data set in the future to better constrain the number density evolution. Such a large sample will be invaluable in future studies of EELGs, having the potential to show correlations in various properties that are concerned with the specific star formation processes and will help to constrain the duty cycle of these bursts at high-z.

CHAPTER 5

CONCLUSIONS AND PROSPECTS

Whish! A gull. Gulls. Far calls. Coming, far! End here. Us then. Finn, again! Take. Bussoftlhee, mememormee! Till thousendsthee. Lps. The keys to. Given! A way a lone a last a loved a long the

James Joyce
Finnegans Wake, 1939

5.1 PRIMARY RESULTS OF THIS THESIS

The main purpose of this Thesis is to study how low-mass galaxies form their stars at $z > 1$. As discussed in van der Wel et al. (2011) and Atek et al. (2011), high-EW emission lines could plausibly trace starbursts in low-mass galaxies. To that end, we identify a sample of these EELGs using multiwavelength photometry and low-resolution grism spectroscopy for additional observations in the near-IR, which traces the rest-frame optical emission from these galaxies. Sophisticated SED modeling, which includes the contribution of the nebular emission to the broadband photometry, demonstrates that these galaxies have low stellar masses and young ages. LBT/LUCI1 and VLT/X-Shooter spectra show that galaxies selected only on the basis of high-EW emission lines typically have very narrow [O III] and/or Hα lines, which is indicative of low total dynamical masses. Likewise, various emission line ratios constrain the source of the ionizing radiation, plausibly identifying strong star formation instead of AGN activity, as well as indicating very low gas-phase metallicities. Together, then, these high-EW galaxies can be classified as starbursting dwarf galaxies, with sSFRs amongst the highest ever measured in these epochs. Constraints on the gas fraction lead us to believe that the lifetime of the burst is not constrained by the total reservoir of gas, but rather by dynamics: the galaxies will become stable against self-collapse and hence star formation on the order of 50 Myr or less. Such an episode is consistent with the predictions from current hydrodynamical situations, allowing for multiple starbursting events per galaxy in order to build-up the stellar mass.

While this confirmation is encouraging, it is not sufficient proof that this is indeed a common way for dwarf galaxies to build up their stellar mass. Duty cycle arguments can be made (as in van der Wel et al. 2011), but the most direct way to test this hypothesis is to measure the (evolution in the) comoving number density of such bursts. To do this, we use 3D-HST grism spectroscopy and a novel method to systematically search for emission lines. After carefully accounting for the completeness of such a search due to limits in sensitivity and continuum magnitude, we see that these bursts are more than an order of magnitude more common at $z \sim 2$ than at lower redshifts, particularly in the local universe where such systems are extremely rare. That the evolution in the number density with redshift matches the evolution in the cosmic star formation rate density is a tantalizing clue that these galaxies build-up their stellar mass via the same mechanisms as more typical galaxies, i.e. not due to merger events.

Overall, then, we conclude that many or most of the stars in local dwarf galaxies formed in a small number of these events at high-redshift, in line with the picture derived from resolved stellar populations of local dwarf galaxies (e.g. Weisz et al. 2011). *This represents the first comprehensive study of dwarf galaxies at z >1.* Several questions remain, however. Primarily, we have seen how strong feedback from supernovae in low-mass galaxies has been claimed, via various simulations, to address several of the primary issues with the ΛCDM cosmological model. Our observed bursts can even satisfy the energy input requirements to create dark matter cores (Amorisco et al. 2014). While in principle our existing observations have the potential to confirm this directly (e.g. via asymmetric emission profiles indicative of multiple dynamical components), and the results from the dynamical arguments support a fast-feedback scenario consistent with Pontzen & Governato (2012), we can not yet make any strong claims about the outflow properties of these systems. Further work, outlined below, is needed to do so.

5.2 PROSPECTS FOR EELG SCIENCE

Here we outline some of the direct extensions to the young field of EELG science, including some work that is already under-way.

5.2.1 OUTFLOWS

While these observations have supported the paradigm first mentioned in Section 1.2, where strong outflows in low-mass systems can change the halo's central dark matter distribution, no direct evidence has been found. Outflows are typically identified via absorption features such as Mg II $\lambda\lambda$2796, 2803, C IV λ1505, Si II λ1526, Al II λ1670, or Fe II λ1608 that are shifted from the systemic redshift of the galaxy (Rubin et al. 2010) or visible in the spectrum of a bright background source due to transverse absorption (like a quasar; Chen et al. 2010). In both cases, the systemic redshift of the galaxy must be determined precisely from strong emission lines. The outflow velocity will determine whether the material will enrich the halo, and make the material available for future star formation, or whether it will escape from the halo, halting star formation for long periods of time and enriching the IGM. While the covering fractions of these systems are unknown, they should be even larger than for more massive, lower-redshift galaxies

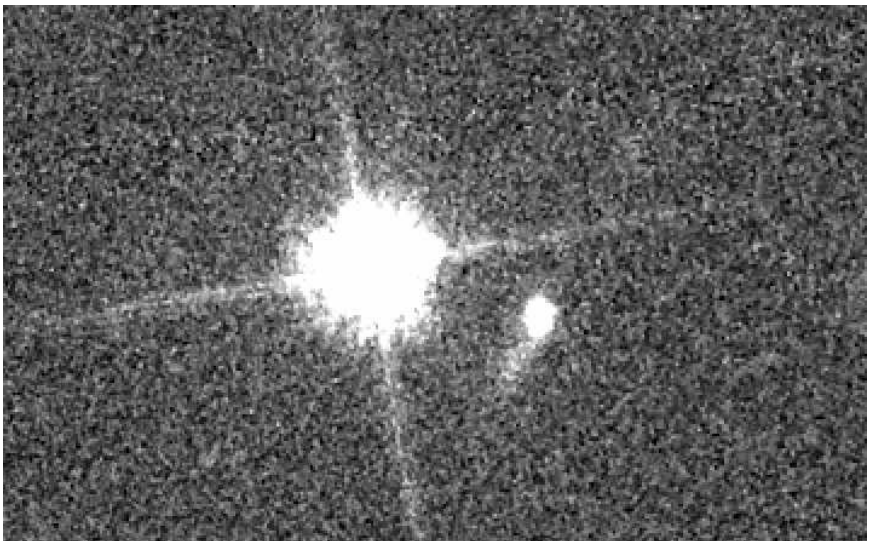

Figure 5.1: *HST/ACS i-band image showing a bright ($R = 18$; left) quasar at $z \sim 2$ which is 2″ away from a foreground $z = 0.8$ EELG (right) first cataloged in Amorín et al. (2014c). The sightline of the background quasar probes the gas around the EELG at a physical distance of 15 kpc.*

(where outflows are detected 2/3 of the time) or for more intensely starforming galaxies (Rubin et al. 2014).

We have attempted to identify the absorption features in the spectra of individual EELGs already, using optical LBT/MODS1 spectroscopy. Such observations are difficult, as they require detections of the ultraviolet continuum (the typical EELG has $m_{UV} \gtrsim 25$). Even with 8 hours of integration (in moderate to poor observing conditions, however), the continuum is not detected for even the brighter targets. Without the detected continuum or moderately strong emission features, data reduction and spectral extraction becomes extremely challenging. Some redshifts, though, are confirmed via detections of [O II] or C III] λ1909 (discussed further in Section 5.2.2), or via previous LBT/LUCI1 spectroscopy. With confirmed systemic redshifts, stacks of the spectra could potentially yield information about the requisite absorption features.

The other method for studying outflows from these low-mass systems is perhaps more promising, although the number density of close e.g. quasar-EELG pairs is very low. Given the rarity of bright $z \gtrsim 2$ quasars, the probability of having an EELG close to such a sightline is $\lesssim 10^{-4}$ at a physical distance of 100 kpc (which at $z = 1.7$ corresponds to 11″; using the quasar statistics from Richards et al. 2006). Thus, a very large sample of EELGs is needed to build up a sample of sightlines. Photometric searches can reach very high fidelities in selecting EELGs in large surveys and will be useful for this task. Multiple sightlines like this at various impact parameters and sSFRs will provide insight to the strength and duration of outflowing events.

We recently identified one such source (shown in Figure 5.1) where an $M_\star = 10^{8.6}\ M_\odot$ (derived using `SB99`, as outlined in van der Wel et al. 2011) EELG at $z \sim 0.8$ is visible via transverse absorption features caused by circumgalactic gas at a distance of 15 kpc in the exquisite Keck/HIRES spectrum of a bright background quasar (shown in Figure 5.2). This represents the first opportunity to study if such low mass galaxies

can drive large-scale outflows (M. Maseda, K. Rubin, N. Crighton et al., in prep.). One tantalizing piece of evidence in this particular case is that there are marginal detections of rare ions in transverse systems, such as Mn II $\lambda\lambda$2576,2594 and Cr II $\lambda\lambda$2056, 2062. This implies an enriched circumgalactic medium (CGM) on the scale of 15 kpc around an EELG. Also intriguing is the dynamical structure of the strong absorption features in Figure 5.1: the quiescent kinematics and simple dynamical structure suggest the gas is not arising in an ongoing outflow, in spite of the extreme starburst activity in the nearby galaxy (cf. the complex dynamics of a 0.2 $L^{\star}$, Lyα emitting galaxy at z=2.5 in Crighton et al. 2015). This in turn suggests the gas was enriched by another galaxy or previous star formation activity from this EELG (the latter case is predicted by e.g. Shen et al. 2014). However, it remains to be determined if the burst is simply too young to have driven an outflow on this scale. If the gas remains cold, it will most likely end up falling into the galaxy eventually, providing fuel for future starbursts. More work is required to obtain an estimate of the mass of metals and dust in the CGM to constrain the metal content of gas fueling the current starburst and put it into the context of Damped Lyman-α absorption line systems at these redshifts. This particularly fortuitous system may be one of the best opportunities to directly test the outflow paradigm in low-mass galaxies.

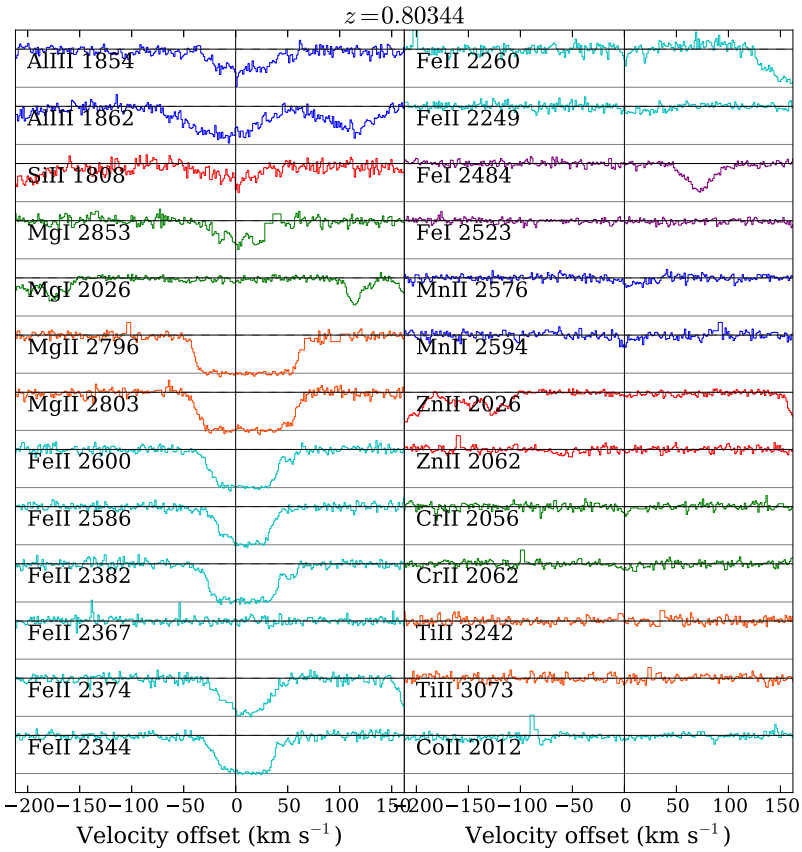

FIGURE 5.2: *Archival Keck/HIRES spectrum (PI: Wolfe) of the quasar shown in Figure 5.1. Absorption features such as Fe II and Mg II at the redshift of the EELG are clearly detected, as well as many other metal transitions. The relatively simple dynamical structure of the strongest absorption features may imply quiescent kinematics in the CGM.*

5.2.2 HIGH-Z SCIENCE AND THE FIRST GALAXIES

By combining deep ground- and space-based optical and near-IR imaging with mid- to far-IR from the *Spitzer Space Telescope*, surveys have recently yielded large samples of galaxies at $z \gtrsim 7$ (e.g. Bouwens et al. 2011; Oesch et al. 2012, 2014; Schenker et al. 2013). These high-redshift galaxies may be detected via the photometric dropout or "Lyman break" technique. Essentially, galaxies do not emit significant amounts of radiation bluewards of 912 Å (restframe), corresponding to the ionization energy of Hydrogen, due to this radiation being almost completely absorbed by neutral Hydrogen around the star-forming regions of galaxies[1]. As such, one can select objects that emit in redder filters with non-detections in bluer ones, thereby isolating a sample of objects whose spectral break has been redshifted to a wavelength corresponding to the bluest detected filter.

One of the major scientific goals of the next generation of space-based and ground-based large telescopes (such as JWST and the E-ELT) will be to address the epoch of Reionization and understand the nature of the ionizing sources. Star-forming dwarf galaxies, AGNs, and Population III (i.e. metal-free) stars are among the proposed candidates. These high redshift (z > 7 - 8) objects will be identified based on the Lyman-break feature in the UV continuum, with detections to highest redshifts aided by the magnification offered by lensing in galaxy cluster fields (e.g. Coe et al. 2013). However, most high-z galaxies discovered in this fashion are quite luminous and therefore a full census of the galaxy population at these redshifts is challenging. For example, the current $z \sim 8$ UV luminosity function (e.g. Schenker et al. 2013) does not extend to galaxies fainter than $M_{UV} \sim -18$, yet observations at $z \sim 2$ assisted by gravitational lensing show no turnover in the UV luminosity function of galaxies down to $M_{UV} \sim -13$ (Alavi et al. 2014): low-luminosity (and presumably low-mass) galaxies are much more common than higher-luminosity galaxies. Most importantly, these low-luminosity star-forming (i.e. UV-bright) galaxies are now thought to have been the primary driver of reionization in the universe (Robertson et al. 2010).

Without spectroscopic confirmations, the inferred high redshifts for these objects will remain questionable, as a variety of lower-z sources could potentially be selected this way (including $z \sim 2$ EELGs: see the discussion in Coe et al. 2013). One of the strongest UV emission lines that will be redshifted to observable wavelengths is the Lyman-α line, but this becomes increasingly difficult to use at $z > 6$ since its visibility is hindered by the fact that most Lyman-α photons do not manage to escape without being absorbed by the predominantly neutral IGM (e.g. Stark et al. 2011; Treu et al. 2013; Dijkstra et al. 2014) during the epoch of Reionization.

The semi-forbidden C III] λ1909 emission line, which is significantly strong (almost 10-15% of the Lyα emission in flux) and has been observed in gravitationally-lensed, star-forming galaxies at $z > 6$, is emerging as a good alternative redshift indicator (Stark et al. 2014a). The C III] line is also frequently observed at $z = 2 - 3$ in EELGs with hard ionizing spectra, and found to have equivalent widths of 10-30 Å (e.g. Erb et al. 2010; Stark et al. 2014b). The composite restframe UV spectra of Lyman-break galaxies at z < 3 also reveal the C III] nebular lines (Shapley et al. 2003). While C III] and other UV emission features (such as C IV λ1550 and O III] λ1663) look very promising to measure redshifts and physical properties of z > 6 galaxies, there are only a handful

[1] This is known as the "Lyman limit." In practice, above $z \sim 6$, there is essentially no observed flux bluewards of 1216 Å due to Lyman-α absorption in the intervening intergalactic medium, known as the "Lyman break."

of cases (mostly lensed) at $z > 1$ where these lines have been measured. Attempts have been made to understand the dependence of the C III] emission on the ionizing flux and the carbon abundance (C/O ratio). The photoionization modeling and SED fitting suggest low metallicity and large [O III]+Hβ equivalent widths (> 700 Å, also implying extremely high sSFRs) for the C III] emitters, placing them firmly in the category of EELGs. However, this has been confirmed spectroscopically only in 4/16 cases where the redshifted oxygen lines are free from the forest of night-sky lines in the near-IR (Stark et al. 2014b). As C III] is predicted to arise due to a high electron temperature in the gas and a hard ionizing spectrum from the low-metallicity stellar populations, it is natural to study this line in EELGs which have such physical conditions. Therefore, $z < 3$ EELGs, which are readily observed with current facilities, give us the ideal chance to prepare for observations of the first galaxies using the next generation of instrumentation.

Likewise, the search method for emission lines outlined in Chapter 4 can easily be extended to search for higher-z emission lines, such as C III] and Lyman-α. While this is straightforward in principle, it is notoriously difficult to obtain proper photometric redshift priors for high-z sources due to very uncertain priors: the expected number of $z \sim 8$ galaxies compared to $z \sim 2$ galaxies is unconstrained observationally and is very model-dependent. As such, the relative probabilistic weighting given to a higher-z solution compared to a lower-z one is somewhat subjective. Additionally, many of these priors do not tend to account for objects such as EELGs, which we show are commonly observed at $z \lesssim 2$ and can potentially masquerade as high-z sources. Further work, then, is needed to create more sensible priors to be used in searching for high-z emission lines in grism spectroscopic data sets. The power of grism spectroscopy here lies in the "multiplexing" capabilities, as many high-z candidates can be observed in wide-area surveys such as 3D-HST. This is crucial given that a fortuitous configuration of the CGM/IGM is required to observe e.g. Lyman-α emission.

5.2.3 CLUSTERING

A careful analysis of the clustering of EELGs will provide information on what type of processes can produce these bursts. This study would require a control sample of non-bursting galaxies, meaning a deep spectroscopic (to confirm redshifts) sample is required to observe faint emission lines in otherwise quiescent, low-mass systems. A full catalog of emission lines from 3D-HST, down to the luminosities discussed in Section 4.4, should suffice for such a study. A control sample can be selected via a cut in specific star formation rate to separate bursts from non-bursts in a given mass range. The first step is to calculate the autocorrelation functions for both samples. The correlation length is the largest scale on which the correlation signal is still detectable, so a small correlation length implies the galaxies live in isolation. Comparing the correlation lengths of bursts/non-bursts will show if the bursts are preferentially clustered, i.e. if bursts have a larger correlation length. Such a case would be indicative of a relationship between the bursts and more massive galaxies, which live in more massive dark matter halos and are also strongly clustered, namely that EELGs are otherwise low-mass systems infalling into more massive halos. A similar test using the two-point correlation function of all low-mass galaxies would determine if the bursts are more likely caused by interactions among low-mass galaxies. In that case, we would expect to see an excess at small scales above the usual two-point function for bursty galaxies (see Robaina

et al. 2009 for such an analysis in the context of $M_* > 10^{10}\ M_\odot$ galaxies). Such a test was performed with quasars by Hennawi et al. (2006), who were able to show that quasar activity is more likely in dense environments due to dissipative interaction events.

This goes to the heart of the question of galaxy formation, asking what actually makes a galaxy "turn on" and start to form stars in the first place. A complete census of the age distribution of EELGs will also constrain the duty cycle of the bursts, quantifying the amount of stellar mass that is likely to build up in these bursts: if the bursts end due to dynamical stability as proposed in Section 3.5 and not because of a limited gas supply, and if the bursts are episodic in nature, then perhaps these systems at z~2 represent the progenitors of today's Milky Way-like galaxies.

5.2.4 Gravitational Lensing and Detailed Properties of the ISM

Strong gravitational lensing can give us the opportunity to look inside these tiny systems, which are barely resolved even in HST imaging. Two lensed EELGs have been discovered in the 3D-HST footprint, at $z = 1.8$ (Tu et al. 2009; Brammer et al. 2012b) and at $z = 3.4$ (the highest redshift galaxy-galaxy lens ever discovered, with the lens at $z = 1.5$; van der Wel et al. 2013). These two systems provide the unique opportunity, due to the boost in spatial resolution caused by the lensing, to probe extremely small ISM scales, on the order of 100 pc. Likewise, the magnification can lead to detections of faint emission lines that would be otherwise undetectable in reasonable observations (cf. Erb et al. 2010).

The intrinsically faint, but greatly magnified (40×) background EELG in the van der Wel et al. (2013) system is among the least massive and most metal-poor high-redshift galaxies discovered to date, with a stellar mass of only $10^8\ M_\odot$ and a gas-phase metallicity upper limit of only $< 5\%\ Z_\odot$ (Amorín et al. 2014b). The EELG is amongst the most intense yet discovered, with an $sSFR = 10^{-7.3}$ yr^{-1} and $EW_{[O\ III],rest} = 1000$ Å. The extreme ionization parameter ($log\ q_{ion} > 8.5$ cm s^{-1}) is comparable only to the most extreme H II galaxies ever observed (e.g. The Lynx arc; Fosbury et al. 2003).

We have begun to obtain a spectrum for this system with VLT/X-Shooter. One particularly intriguing goal is to detect He II λ1640 emission, which could be related with infalling pristine gas (Yang et al. 2006; Cassata et al. 2013). Moreover, the simultaneous detection of He II and Lyman-α would provide an additional footprint of both Population III star formation regions and gas cooling during gravitational accretion (Schaerer 2003). Deep observations of the nebular emission lines will be able to constrain the number of distinct dynamical components present; multiple dynamical components would indicate a clumpy structure in the starforming regions and rapid gas flows as a result of mergers or feedback (Amorín et al. 2012). While the total number of these lensed systems is low, the exquisite detail they present will be crucial in understanding the small-scale physical processes occurring in EELGs.

But, as they say, "One thesis at a time..."

Finis.

APPENDIX A

COMPLETE LIST OF NEAR-IR OBSERVATIONS

Tables 2.1 and 3.2 describe the samples used in Maseda et al. (2013) and Maseda et al. (2014), respectively. As much of the CANDELS photometric work was in-progress during the publication stages of these papers, the same objects were sometimes given different ID numbers. Presented here is a complete list of the objects observed with LBT/LUCI1 or VLT/X-Shooter that had detected emission lines (cf. Table 3.1), complete with the Skelton et al. (2014) ID numbers and any other samples the objects were included in.

Table A.1. Combined Summary of Near-IR Observations and Masses

ID Skelton et al. (2014)	RA (deg)	Dec (deg)	Instrument	z_{spec}	$\sigma_{[OIII]}$ (km s^{-1})	Reference	Other IDs
COSMOS-8165	150.14384	2.26336	LUCI1	1.492	46.2±2.2	This thesis	
COSMOS-8283	150.15233	2.26413	LUCI1	1.597	50.8±8.0	This thesis	
COSMOS-9459	150.10477	2.27602	LUCI1	1.465	76.7±0.9	This thesis	
COSMOS-10599	150.09535	2.28725	LUCI1	2.220	30.9±9.0	Maseda et al. (2013)	8991 (M13), 10599 (M14)
COSMOS-12102	150.09728	2.30252	LUCI1	1.463	241.3±12.7	Maseda et al. (2014)	12102 (M14)
COSMOS-13184	150.12424	2.31367	LUCI1	2.199	40.3±8.9	Maseda et al. (2013)	11212 (M13), 13184 (M14)
COSMOS-15091	150.15955	2.33330	LUCI1	1.583	38.2±10.0	Maseda et al. (2013)	12807(M13), 15091 (M14)
COSMOS-16286	150.17699	2.34539	LUCI1	1.444	46.7±14.4	Maseda et al. (2013)	13848 (M13), 16286 (M14)
COSMOS-16566	150.17067	2.34830	LUCI1	1.437	32.8±8.4	Maseda et al. (2014)	16566 (M14)
COSMOS-17118	150.15114	2.35410	LUCI1	1.656	46.5±8.8	Maseda et al. (2014)	17118 (M14)
COSMOS-17839	150.15677	2.36080	LUCI1	1.412	43.3±8.9	Maseda et al. (2013)	15144 (M13), 17839 (M14)
COSMOS-18358	150.16719	2.36689	LUCI1	1.645	55.9±9.0	Maseda et al. (2014)	18358 (M14)
COSMOS-19049	150.13886	2.37340	LUCI1	1.370	122.0±11.0	Maseda et al. (2014)	19049 (M14)
COSMOS-19077	150.18309	2.37295	LUCI1	1.649	47.7±9.5	Maseda et al. (2013)	16207 (M13), 19077 (M14)
GOODS-S-33131	53.17194	-27.75915	X-SHOOTER	1.687	52.3±5.7	Maseda et al. (2013)	8 (vdW11), 17892 (M13), 7892 (M14)
GOODS-S-43693	53.07129	-27.70580	X-SHOOTER	1.738	54.4±4.5[a]	Straughn et al. (2011)	402 (S11), 18 (vdW11), 26816 (M13), 43693 (M14)
GOODS-S-43928	53.05158	-27.70476	X-SHOOTER	1.472	31.4±8.2	Straughn et al. (2011)	499 (S11), 43928 (M14)
UDS-6195	34.42648	-5.25577	X-SHOOTER	1.687	54.7±6.1	van der Wel et al. (2011)	5 (vdW11), 3646 (M13), 6195 (M14)
UDS-6377	34.42857	-5.25532	X-SHOOTER	1.664	48.2±5.9	van der Wel et al. (2011)	6 (vdW11), 3760 (M13), 6377 (M14)
UDS-7665	34.39076	-5.25080	LUCI1	2.298	57.8±9.7	Maseda et al. (2013)	4501 (M13), 7665 (M14)
UDS-10138	34.42336	-5.24226	LUCI1	2.151	80.9±10.0	Maseda et al. (2014)	10138 (M14)
UDS-12435	34.41087	-5.23481	LUCI1	1.611	65.2±11.3[a]	Maseda et al. (2014)	12435 (M14)
UDS-12539	34.47389	-5.23423	X-SHOOTER	1.621	71.1±5.7	Maseda et al. (2013)	12 (vdW11), 7444 (M13), 12539 (M14)
UDS-19167	34.43140	-5.21212	LUCI1	2.185	54.2±9.4	Maseda et al. (2013)	11484 (M13), 19167 (M14)
UDS-24154	34.39137	-5.19531	LUCI1	2.297	61.0±10.8	Maseda et al. (2013)	14655 (M13), 24154 (M14)

Note. — M13: Maseda et al. (2013); M14: Maseda et al. (2014); S11: Straughn et al. (2011); vdW11: van der Wel et al. (2011)

[a]Hα width.

APPENDIX B

NEBULAR EMISSION*

This Appendix is meant to give a brief overview of the origin of nebular emission, which is the theoretical backbone to the entire spectroscopic study of EELGs. In particular, the cases of Hα and [O III] will be outlined here (mostly for my own personal edification). This is not meant to be a comprehensive description, but rather a simplification; a basic knowledge of atomic physics is assumed. The Bohr (1913) model suffices for the purposes here, where atoms absorb radiation according to:

$$\Delta E = E_2 - E_1 = h\nu, \tag{B.1}$$

where E_2 is the new energy level of the system, E_1 was the original level, h is Planck's constant, and ν is the frequency of the incident photon. If the photon γ is energetic enough, namely if its energy exceeds the binding energy of an electron to the nucleus, it can ionize the atom. Likewise, if a nucleus captures an electron, it will emit a photon with an energy corresponding to the binding energy. In the case of Hydrogen:

$$H + \gamma \leftrightarrow p^+ + e^-. \tag{B.2}$$

B.1 THE BALMER SERIES: Hα

Let's consider a region of Hydrogen gas (a nebula) surrounding a central ionizing source (such as a star). The individual atoms will either be in the ground state (neutral) or in an excited state (ionized). UV photons emitted by the central source may encounter one of these atoms on their outward journey, particularly if the nebula is dense and/or large. When a photon with an energy above 13.6 eV (the ionization energy for neutral Hydrogen; these photons are termed "Lyman continuum" photons) reaches an atom, it becomes absorbed and thus ionizes the atom. The electron, now freed from the proton, travels until it encounters another proton and becomes absorbed. There are two subsequent cases: either the electron falls directly to the ground level (n=0) of the atom or it falls into a higher energy level. In the first case, another UV photon is emitted and the process repeats. In the second case, the electron cascades down in the energy levels of the atom, subsequently emitting photons of various energies (Rosseland 1926). If

*Based heavily on Gurzadyan (1970).

the electron falls into the second energy level (n=1), then it decays to the ground state by emitting a single Lyman-α photon (1→0 + Lyα). However, the Hydrogen gas in the nebula is opaque to photons of this energy and it will be absorbed by a neutral atom before traveling far. This process is repeated many times for Lyman-α photons, known as "fluorescence" and hence they will experience many scattering events before escaping the nebular region. If the electron falls into the third energy level (n=2), then it can either emit a Balmer Hα photon followed by a Lyman-α photon (2→1 + Hα, 1→0 + Lyα) or go directly to the ground state by emitting a Lyman-β photon (2→0 + Lyβ). The Lyman photons will not easily escape the nebular region, whereas the Hα photons, which are not energetic enough to ionize the neutral Hydrogen, easily escape the region. This same process occurs at higher energy levels as well, including photons in the Paschen, Brackett, Pfund, etc. series. Overall, then, every Lyman continuum photon emitted will result in the emission of at least one Lyα and one Hα photon (Zanstra 1927).

B.2 "FORBIDDEN" LINES: [O III]

As previously mentioned (i.e. in Section 1.4), the "forbidden" [O III] $\lambda\lambda$5007,4959 doublet is one of the primary emission features in the spectrum of nebular regions. The term "forbidden" simply means that the transitions do not occur in laboratory conditions, only in regions of extremely low densities. Previous studies attributed this emission to a completely new element, *nebulium* (Huggins & Miller 1864; Nicholson 1911). It was not until Bowen (1927) that these emission features, which are extremely bright in observations of planetary nebulae, could be attributed to doubly-ionized Oxygen. This requires, of course, that the gas cannot be primordial and must contain at least some Oxygen, which was not created in the Big Bang. These transitions are forbidden by the standard Hund selection rules, but, as quadrupole transitions, they are simply rare: the transition probability for the $^3P_2 - {}^1D_2$ λ5007 line is 1.8×10^{-2} s^{-1} (Baluja & Doyle 1981), which is $\sim 3 \times 10^{-11}$ times as likely as the $^2S - {}^2P^o$ Lyman-α line (Baker 2008). That the rare [O III] transitions are as bright as or brighter than some of the Hydrogen transitions in these regions implies that the energy level from which they originate, now known to be within the doubly-ionized O III ion, must only decay to the ground state via these forbidden transitions. Such a state is known as "metastable." Given the rarity of the transition, the mean lifetime of the metastable state should be large, on the order of one second. For this to be the case, the density of the gas should be low so as to avoid collisions which would transfer the radiation energy into kinetic energy and the density of photons should also be low since there should not be significant energy absorbed by the atom to transform it from the metastable state.

The primary excitation mechanism to put the O III ions in the metastable state cannot simply be photoionization, since their observed brightness far exceeds the number of ionizing photons emitted by the stellar sources in nebulae. They are instead excited due to inelastic collisions with free electrons, where much of the kinetic energy of the electron is transferred to the O III ion. The density of free electrons in the gas should be low, given that further collisions once the ion is in the metastable state would prevent the forbidden emission, but it should still be high enough for such transitions to occur. The difference in timescales is illustrative here: a free O III ion can last between 3 hours and 17 weeks between collisions in the low-densities of nebular regions (Bowen 1927), whereas it emits the forbidden photons from its metastable state after only a few seconds. This collisional excitation is why the ratio of [O III] λ4363 to [O III] $\lambda\lambda$5007,4959 is

a useful diagnostic of the electron temperature of the nebular region (see Section 3.4.1): λ4363 arises from an energy level (^1S) above that of $\lambda\lambda$5007,4959 (^1D), and any λ4363 emission will also produce an intermediate λ5007 or λ4959 photon. Since the relative populations of ions in the ^1S and ^1D levels is due to the kinetic energy imparted by the free electrons to the ions, the ratio of emission is a sensitive probe of the electron temperature (itself a measure of the kinetic energy in the ensemble of electrons) in the nebular region.

ACRONYMS

ΛCDM	Cold dark matter model with a cosmological constant (Λ)
ACS	Advanced Camera for Surveys
AEGIS	All-wavelength Extended Groth Strip International Survey
AGN	Active galactic nuclei
ALMA	Atacama Large Millimeter Array
AMR	Adaptive Mesh Refinement
BCD	Blue compact dwarf
BPT	Baldwin, Phillips, & Terlevich (1981)
CANDELS	Cosmic Assembly Near-infrared Deep Extragalactic Legacy Survey
CDM	Cold dark matter
CGM	Circumgalactic medium
CMB	Cosmic microwave background
CMD	Color-magnitude diagram
COBE	Cosmic Background Explorer
COSMOS	Cosmic Evolution Survey
EAZY	Easy and Accurate z_{phot} from Yale
EELG	Extreme emission line galaxy
EELT	European Extremely Large Telescope
ELG	Emission line galaxy
ESO	European Southern Observatory
EW	Equivalent width
FMR	Fundamental metallicity relation
FWHM	Full width at half maximum
GOODS-N	Great Observatories Origins Deep Survey - North
GOODS-S	Great Observatories Origins Deep Survey - South
HIRES	High Resolution Echelle Spectrometer
HiZELS	High-z Emission Line Survey
HST	Hubble Space Telescope
HR	Hertzsprung-Russell
HWHM	Half width at half maximum
IGM	Intergalactic medium
IMF	Initial mass function
IR	Infrared
IRAC	Infrared Array Camera
ISM	Interstellar medium
JWST	James Webb Space Telescope
LBT	Large Binocular Telescope

LUCI1	LBT NIR Spectrograph Utility with Camera and Integral-Field Unit for Extragalactic Research 1
MAGPHYS	Multi-wavelength Analysis of Galaxy Physical Properties
MEx	Mass Excitation (diagram)
MIPS	Multiband Imaging Photometer for Spitzer
M/L	Mass-to-light (ratio)
MODS1	Multi Object Double Spectrograph 1
MZ	Mass-metallicity (relation)
NICMOS	Near Infrared Camera Multi-Object Spectrometer
NIR	Near-infrared
PA	Position angle
PEARS	Probing Evolution And Reionization Spectroscopically
PÉGASE	Projet d'Étude des Galaxies par Synthèse Évolutive
PP04	Pettini & Pagel (2004)
PSF	Point spread function
QSO	Quasi-stellar object
SB99	Starburst99 (Leitherer et al. 1999)
SDSS	Sloan Digital Sky Survey
SED	Spectral energy distribution
SF	Star-forming/star-formation
SFH	Star formation history
SFR	Star formation rate
SHM	Stellar mass-halo mass (ratio)
SMBH	Super-massive black hole
SMG	Submillimeter galaxy
S/N	Signal-to-noise
SPH	Smoothed Particle Hydrodynamics
sSFR	Specific star formation rate (star formation rate per stellar mass)
SSP	Simple stellar population
UDS	United Kingdom Infrared Telescope Deep Sky Survey: Ultra Deep Survey
ULIRG	Ultra-luminous infrared galaxy
UV	Ultraviolet
UVB	Ultraviolet-blue
VIS	Visible
VLT	Very Large Telescope
WFC3	Wide Field Camera 3
WISP	WFC3 Infrared Spectroscopic Parallels
WMAP	Wilkinson Microwave Anisotropy Probe

Bibliography

Aird, J., Coil, A. L., Moustakas, J., et al. 2012, The Astrophysical Journal, 746, 90
Alavi, A., Siana, B., Richard, J., et al. 2014, The Astrophysical Journal, 780, 143
Alcock, C., Allsman, R. A., Alves, D. R., et al. 2000, The Astrophysical Journal, 542, 281
Amorín, R., Pérez-Montero, E., & Vílchez, J. M. 2010, The Astrophysical Journal Letters, 715, L128
Amorín, R., Vílchez, J. M., Hägele, G. F., et al. 2012, The Astrophysical Journal Letters, 754, L22
Amorín, R., Sommariva, V., Castellano, M., et al. 2014a, Astronomy & Astrophysics, 568, L8
Amorín, R., Grazian, A., Castellano, M., et al. 2014b, The Astrophysical Journal Letters, 788, L4
Amorín, R., Pérez-Montero, E., Contini, T., et al. 2014c, arXiv:1403.3441
Amorisco, N. C., & Evans, N. W. 2012, Monthly Notices of the Royal Astronomical Society, 419, 184
Amorisco, N. C., Zavala, J., & de Boer, T. J. L. 2014, The Astrophysical Journal Letters, 782, L39
Atek, H., Malkan, M., McCarthy, P., et al. 2010, The Astrophysical Journal, 723, 104
Atek, H., Siana, B., Scarlata, C., et al. 2011, The Astrophysical Journal, 743, 121
Babul, A., & Ferguson, H. C. 1996, The Astrophysical Journal, 458, 100
Babul, A., & Rees, M. J. 1992, Monthly Notices of the Royal Astronomical Society, 255, 346
Baker, J. 2008, Transition probabilities for one electron atoms, Technical note, Natl. Inst. Stand. Technol., Washington, DC
Baldwin, J. A., Phillips, M. M., & Terlevich, R. 1981, Publications of the Astronomical Society of the Pacific, 93, 5
Baluja, K. L., & Doyle, J. G. 1981, Journal of Physics B, 14, p. L11
Balzano, V. A. 1983, The Astrophysical Journal, 268, 602
Barton, E. J., & van Zee, L. 2001, The Astrophysical Journal Letters, 550, L35
Belokurov, V., Zucker, D. B., Evans, N. W., et al. 2006, The Astrophysical Journal Letters, 647, L111
Bennett, C. L., Banday, A. J., Gorski, K. M., et al. 1996, The Astrophysical Journal Letters, 464, L1
Bennett, C. L., Bay, M., Halpern, M., et al. 2003, The Astrophysical Journal, 583, 1
Benson, A. J., Baugh, C. M., Cole, S., Frenk, C. S., & Lacey, C. G. 2000a, Monthly Notices of the Royal Astronomical Society, 316, 107
Benson, A. J., Cole, S., Frenk, C. S., Baugh, C. M., & Lacey, C. G. 2000b, Monthly Notices of the Royal Astronomical Society, 311, 793
Binney, J., & Tremaine, S. 2008, Galactic Dynamics: Second Edition (Princeton University Press)
Blanton, M. R., & Roweis, S. 2007, The Astronomical Journal, 133, 734
Blumenthal, G. R., Faber, S. M., Primack, J. R., & Rees, M. J. 1984, Nature, 311, 517
Boggess, N. W., Mather, J. C., Weiss, R., et al. 1992, The Astrophysical Journal, 397, 420
Bohr, N. 1913, Philosophical Magazine Series 6, 26, 1

Borgani, S., Murante, G., Springel, V., et al. 2004, Monthly Notices of the Royal Astronomical Society, 348, 1078
Bouwens, R. J., Illingworth, G. D., Franx, M., & Ford, H. 2007, The Astrophysical Journal, 670, 928
Bouwens, R. J., Illingworth, G. D., Oesch, P. A., et al. 2011, The Astrophysical Journal, 737, 90
Bouwens, R. J., Oesch, P. A., Illingworth, G. D., et al. 2013, The Astrophysical Journal Letters, 765, L16
Bowen, I. S. 1927, Publications of the Astronomical Society of the Pacific, 39, 295
Boylan-Kolchin, M., Bullock, J. S., & Kaplinghat, M. 2011, Monthly Notices of the Royal Astronomical Society, 415, L40
Boyle, B. J., Shanks, T., Croom, S. M., et al. 2000, Monthly Notices of the Royal Astronomical Society, 317, 1014
Brammer, G. B., van Dokkum, P. G., & Coppi, P. 2008, The Astrophysical Journal, 686, 1503
Brammer, G. B., van Dokkum, P. G., Illingworth, G. D., et al. 2013, The Astrophysical Journal Letters, 765, L2
Brammer, G. B., van Dokkum, P. G., Franx, M., et al. 2012a, The Astrophysical Journal Supplements, 200, 13
Brammer, G. B., Sánchez-Janssen, R., Labbé, I., et al. 2012b, The Astrophysical Journal Letters, 758, L17
Bruzual, G., & Charlot, S. 2003, Monthly Notices of the Royal Astronomical Society, 344, 1000
Cardamone, C., Schawinski, K., Sarzi, M., et al. 2009, Monthly Notices of the Royal Astronomical Society, 399, 1191
Cassata, P., Le Fèvre, O., Charlot, S., et al. 2013, Astronomy & Astrophysics, 556, A68
Chabrier, G. 2003, Publications of the Astronomical Society of the Pacific, 115, 763
Charlot, S., & Fall, S. M. 2000, The Astrophysical Journal, 539, 718
Charlot, S., & Longhetti, M. 2001, Monthly Notices of the Royal Astronomical Society, 323, 887
Chen, H.-W., Helsby, J. E., Gauthier, J.-R., et al. 2010, The Astrophysical Journal, 714, 1521
Coe, D., Zitrin, A., Carrasco, M., et al. 2013, The Astrophysical Journal, 762, 32
Conroy, C. 2013, Annual Reviews of Astronomy & Astrophysics, 51, 393
Contini, T., Garilli, B., Le Fèvre, O., et al. 2012, Astronomy & Astrophysics, 539, A91
Crighton, N. H. M., Hennawi, J. F., Simcoe, R. A., et al. 2015, Monthly Notices of the Royal Astronomical Society, 446, 18
Curtis-Lake, E., McLure, R. J., Dunlop, J. S., et al. 2013, Monthly Notices of the Royal Astronomical Society, 429, 302
da Cunha, E., Charlot, S., & Elbaz, D. 2008, Monthly Notices of the Royal Astronomical Society, 388, 1595
da Cunha, E., Walter, F., Decarli, R., et al. 2013, The Astrophysical Journal, 765, 9
Daddi, E., Cimatti, A., Renzini, A., et al. 2004, The Astrophysical Journal, 617, 746
Daddi, E., Elbaz, D., Walter, F., et al. 2010a, The Astrophysical Journal Letters, 714, L118
Daddi, E., Bournaud, F., Walter, F., et al. 2010b, The Astrophysical Journal, 713, 686
de Blok, W. J. G. 2010, Advances in Astronomy, 2010, 5
Dekel, A., & Silk, J. 1986, The Astrophysical Journal, 303, 39
Dicke, R. H., Peebles, P. J. E., Roll, P. G., & Wilkinson, D. T. 1965, The Astrophysical Journal, 142, 414
Dijkstra, M., Wyithe, S., Haiman, Z., Mesinger, A., & Pentericci, L. 2014, Monthly Notices of the Royal Astronomical Society, 440, 3309
Dolphin, A. E. 2002, Monthly Notices of the Royal Astronomical Society, 332, 91
—. 2012, The Astrophysical Journal, 751, 60
—. 2013, The Astrophysical Journal, 775, 76
Ellis, R. S., McLure, R. J., Dunlop, J. S., et al. 2013, The Astrophysical Journal Letters, 763, L7
Elmegreen, D. M., Elmegreen, B. G., Ravindranath, S., & Coe, D. A. 2007, The Astrophysical Journal, 658, 763
Erb, D. K., Pettini, M., Shapley, A. E., et al. 2010, The Astrophysical Journal, 719, 1168
Erb, D. K., Steidel, C. C., Shapley, A. E., et al. 2006, The Astrophysical Journal, 646, 107

Ewen, H. I., & Purcell, E. M. 1951, Nature, 168, 356
Ferland, G. J. 1996, Hazy, A Brief Introduction to Cloudy 90
Ferreras, I., Pasquali, A., Khochfar, S., et al. 2012, The Astronomical Journal, 144, 47
Fioc, M., & Rocca-Volmerange, B. 1997, Astronomy & Astrophysics, 326, 950
Fixsen, D. J. 2009, The Astrophysical Journal, 707, 916
Fixsen, D. J., Cheng, E. S., Gales, J. M., et al. 1996, The Astrophysical Journal, 473, 576
Flores, R. A., & Primack, J. R. 1994, The Astrophysical Journal Letters, 427, L1
Förster Schreiber, N. M., Genzel, R., Bouché, N., et al. 2009, The Astrophysical Journal, 706, 1364
Fosbury, R. A. E., Villar-Martín, M., Humphrey, A., et al. 2003, The Astrophysical Journal, 596, 797
Franx, M., Labbé, I., Rudnick, G., et al. 2003, The Astrophysical Journal Letters, 587, L79
Fumagalli, M., Patel, S. G., Franx, M., et al. 2012, The Astrophysical Journal Letters, 757, L22
Fumagalli, M., Labbé, I., Patel, S. G., et al. 2014, The Astrophysical Journal, 796, 35
Galametz, A., Grazian, A., Fontana, A., et al. 2013, The Astrophysical Journal Supplements, 206, 10
Gallagher, III, J. S., Hunter, D. A., & Tutukov, A. V. 1984, The Astrophysical Journal, 284, 544
Geach, J. E., Smail, I., Best, P. N., et al. 2008, Monthly Notices of the Royal Astronomical Society, 388, 1473
Gnedin, O. Y., & Zhao, H. 2002, Monthly Notices of the Royal Astronomical Society, 333, 299
Governato, F., Willman, B., Mayer, L., et al. 2007, Monthly Notices of the Royal Astronomical Society, 374, 1479
Governato, F., Zolotov, A., Pontzen, A., et al. 2012, Monthly Notices of the Royal Astronomical Society, 422, 1231
Grebel, E. K. 1997, in Reviews in Modern Astronomy, Vol. 10, Reviews in Modern Astronomy, ed. R. E. Schielicke, 29–60
Grogin, N. A., Kocevski, D. D., Faber, S. M., et al. 2011, The Astrophysical Journal Supplements, 197, 35
Groves, B. A., Heckman, T. M., & Kauffmann, G. 2006, Monthly Notices of the Royal Astronomical Society, 371, 1559
Guo, Q., White, S., Boylan-Kolchin, M., et al. 2011, Monthly Notices of the Royal Astronomical Society, 413, 101
Guo, Y., Ferguson, H. C., Giavalisco, M., et al. 2013, The Astrophysical Journal Supplements, 207, 24
Gurzadyan, G. A. 1970, Planetary nebulae
Gush, H. P., Halpern, M., & Wishnow, E. H. 1990, Physical Review Letters, 65, 537
Häring, N., & Rix, H.-W. 2004, The Astrophysical Journal Letters, 604, L89
Hennawi, J. F., Strauss, M. A., Oguri, M., et al. 2006, The Astronomical Journal, 131, 1
Henry, A., Martin, C. L., Finlator, K., & Dressler, A. 2013a, The Astrophysical Journal, 769, 148
Henry, A., Scarlata, C., Domínguez, A., et al. 2013b, The Astrophysical Journal Letters, 776, L27
Herschel, W. 1800, Philosophical Transactions of the Royal Society of London, 90, 284
Hodge, P. W. 1971, Annual Reviews of Astronomy & Astrophysics, 9, 35
Holmberg, E. 1941, The Astrophysical Journal, 94, 385
Hopkins, A. M., & Beacom, J. F. 2006, The Astrophysical Journal, 651, 142
Hubble, E. P. 1926, The Astrophysical Journal, 64, 321
—. 1929, The Astrophysical Journal, 69, 103
Huggins, W., & Miller, W. A. 1864, Royal Society of London Philosophical Transactions Series I, 154, 437
Izotov, Y. I., Guseva, N. G., & Thuan, T. X. 2011, The Astrophysical Journal, 728, 161
Izotov, Y. I., Stasińska, G., Meynet, G., Guseva, N. G., & Thuan, T. X. 2006, Astronomy & Astrophysics, 448, 955
Izotov, Y. I., & Thuan, T. X. 2008, The Astrophysical Journal, 687, 133
Johnson, D. G., & Wilkinson, D. T. 1987, The Astrophysical Journal Letters, 313, L1
Jones, T. A., Swinbank, A. M., Ellis, R. S., Richard, J., & Stark, D. P. 2010, Monthly Notices of the Royal Astronomical Society, 404, 1247
Juneau, S., Dickinson, M., Alexander, D. M., & Salim, S. 2011, The Astrophysical Journal, 736, 104

Karachentsev, I. D., Karachentseva, V. E., Huchtmeier, W. K., & Makarov, D. I. 2004, The Astronomical Journal, 127, 2031
Karim, A., Schinnerer, E., Martínez-Sansigre, A., et al. 2011, The Astrophysical Journal, 730, 61
Kassin, S. A., Weiner, B. J., Faber, S. M., et al. 2007, The Astrophysical Journal Letters, 660, L35
Kauffmann, G., White, S. D. M., & Guiderdoni, B. 1993, Monthly Notices of the Royal Astronomical Society, 264, 201
Kauffmann, G., Heckman, T. M., White, S. D. M., et al. 2003, Monthly Notices of the Royal Astronomical Society, 341, 33
Kennicutt, Jr., R. C. 1998, Annual Reviews of Astronomy & Astrophysics, 36, 189
Kennicutt, Jr., R. C., Calzetti, D., Walter, F., et al. 2007, The Astrophysical Journal, 671, 333
Kewley, L. J., & Ellison, S. L. 2008, The Astrophysical Journal, 681, 1183
Kewley, L. J., Groves, B., Kauffmann, G., & Heckman, T. 2006, Monthly Notices of the Royal Astronomical Society, 372, 961
Kewley, L. J., Maier, C., Yabe, K., et al. 2013, The Astrophysical Journal Letters, 774, L10
Klypin, A., Kravtsov, A. V., Valenzuela, O., & Prada, F. 1999, The Astrophysical Journal, 522, 82
Koekemoer, A. M., Faber, S. M., Ferguson, H. C., et al. 2011, The Astrophysical Journal Supplements, 197, 36
Kümmel, M., Walsh, J. R., Pirzkal, N., Kuntschner, H., & Pasquali, A. 2009, Publications of the Astronomical Society of the Pacific, 121, 59
Larson, R. B. 1974, Monthly Notices of the Royal Astronomical Society, 169, 229
Law, D. R., Steidel, C. C., Erb, D. K., et al. 2009, The Astrophysical Journal, 697, 2057
Law, D. R., Steidel, C. C., Shapley, A. E., et al. 2012, The Astrophysical Journal, 759, 29
Lee, J. C., Kennicutt, Jr., R. C., Funes, S. J. J. G., Sakai, S., & Akiyama, S. 2009, The Astrophysical Journal, 692, 1305
Leitherer, C., Schaerer, D., Goldader, J. D., et al. 1999, The Astrophysical Journal Supplements, 123, 3
Lemaître, G. 1927, Annales de la Société Scientifique de Bruxelles, 47, 49
Lotz, J. M., Jonsson, P., Cox, T. J., & Primack, J. R. 2010, Monthly Notices of the Royal Astronomical Society, 404, 590
Lundmark, K. 1925, Monthly Notices of the Royal Astronomical Society, 85, 865
Ly, C., Malkan, M. A., Hayashi, M., et al. 2011, The Astrophysical Journal, 735, 91
Maiolino, R., Nagao, T., Grazian, A., et al. 2008, Astronomy & Astrophysics, 488, 463
Mancini, C., Förster Schreiber, N. M., Renzini, A., et al. 2011, The Astrophysical Journal, 743, 86
Mannucci, F., Cresci, G., Maiolino, R., Marconi, A., & Gnerucci, A. 2010, Monthly Notices of the Royal Astronomical Society, 408, 2115
Martin, N. F., Ibata, R. A., Irwin, M. J., et al. 2006, Monthly Notices of the Royal Astronomical Society, 371, 1983
Maseda, M. V., van der Wel, A., da Cunha, E., et al. 2013, The Astrophysical Journal Letters, 778, L22
Maseda, M. V., van der Wel, A., Rix, H.-W., et al. 2014, The Astrophysical Journal, 791, 17
Masters, D., McCarthy, P., Burgasser, A. J., et al. 2012, The Astrophysical Journal Letters, 752, L14
Masters, D., McCarthy, P., Siana, B., et al. 2014, The Astrophysical Journal, 785, 153
Mateo, M. L. 1998, Annual Reviews of Astronomy & Astrophysics, 36, 435
McBride, J., Fakhouri, O., & Ma, C.-P. 2009, Monthly Notices of the Royal Astronomical Society, 398, 1858
McMillan, P. J. 2011, Monthly Notices of the Royal Astronomical Society, 414, 2446
Meurer, G. R., Tsvetanov, Z. I., Gronwall, C., et al. 2007, The Astronomical Journal, 134, 77
Moore, B. 1994, Nature, 370, 629
Moster, B. P., Somerville, R. S., Maulbetsch, C., et al. 2010, The Astrophysical Journal, 710, 903
Muller, C. A., & Oort, J. H. 1951, Nature, 168, 357
Navarro, J. F., Eke, V. R., & Frenk, C. S. 1996a, Monthly Notices of the Royal Astronomical Society, 283, L72
Navarro, J. F., Frenk, C. S., & White, S. D. M. 1996b, The Astrophysical Journal, 462, 563
Nelson, E. J., van Dokkum, P. G., Brammer, G., et al. 2012, The Astrophysical Journal Letters, 747, L28

Nichols, E. F. 1901, The Astrophysical Journal, 13, 101
Nicholson, J. W. 1911, Philosophical Magazine, Series 6, 22, 864
Noeske, K. G., Weiner, B. J., Faber, S. M., et al. 2007, The Astrophysical Journal Letters, 660, L43
Norberg, P., Baugh, C. M., Hawkins, E., et al. 2001, Monthly Notices of the Royal Astronomical Society, 328, 64
Oesch, P. A., Bouwens, R. J., Illingworth, G. D., et al. 2012, The Astrophysical Journal, 759, 135
—. 2014, The Astrophysical Journal, 786, 108
Oke, J. B. 1974, The Astrophysical Journal Supplements, 27, 21
Osterbrock, D. E., & Mathews, W. G. 1986, Annual Reviews of Astronomy & Astrophysics, 24, 171
Pacifici, C., Charlot, S., Blaizot, J., & Brinchmann, J. 2012, Monthly Notices of the Royal Astronomical Society, 421, 2002
Pacifici, C., da Cunha, E., Charlot, S., et al. 2015, Monthly Notices of the Royal Astronomical Society, 447, 786
Pagel, B. E. J., Edmunds, M. G., Blackwell, D. E., Chun, M. S., & Smith, G. 1979, Monthly Notices of the Royal Astronomical Society, 189, 95
Patel, S. G., Fumagalli, M., Franx, M., et al. 2013, The Astrophysical Journal, 778, 115
Peebles, P. J. E. 1982, The Astrophysical Journal Letters, 263, L1
Peebles, P. J. E., & Yu, J. T. 1970, The Astrophysical Journal, 162, 815
Pelupessy, F. I., van der Werf, P. P., & Icke, V. 2004, Astronomy & Astrophysics, 422, 55
Penzias, A. A., & Wilson, R. W. 1965, The Astrophysical Journal, 142, 419
Pettini, M., & Pagel, B. E. J. 2004, Monthly Notices of the Royal Astronomical Society, 348, L59
Pettit, E., & Nicholson, S. B. 1928, Contributions from the Mount Wilson Observatory / Carnegie Institution of Washington, 369, 1
Pirzkal, N., Xu, C., Malhotra, S., et al. 2004, The Astrophysical Journal Supplements, 154, 501
Pirzkal, N., Rothberg, B., Ly, C., et al. 2013, The Astrophysical Journal, 772, 48
Pontzen, A., & Governato, F. 2012, Monthly Notices of the Royal Astronomical Society, 421, 3464
Read, J. I., & Gilmore, G. 2005, Monthly Notices of the Royal Astronomical Society, 356, 107
Reines, A. E., Greene, J. E., & Geha, M. 2013, The Astrophysical Journal, 775, 116
Rhoads, J. E., Malhotra, S., Pirzkal, N., et al. 2009, The Astrophysical Journal, 697, 942
Richards, G. T., Strauss, M. A., Fan, X., et al. 2006, The Astronomical Journal, 131, 2766
Rix, H.-W., Guhathakurta, P., Colless, M., & Ing, K. 1997, Monthly Notices of the Royal Astronomical Society, 285, 779
Robaina, A. R., Bell, E. F., Skelton, R. E., et al. 2009, The Astrophysical Journal, 704, 324
Roberts, I. 1893, Photographs of stars, star-clusters and nebulae, together with records of results obtained in the pursuit of celestial photography (London: Universal Press)
Robertson, B. E., Ellis, R. S., Dunlop, J. S., McLure, R. J., & Stark, D. P. 2010, Nature, 468, 49
Rosseland, S. 1926, The Astrophysical Journal, 63, 218
Rubin, K. H. R., Prochaska, J. X., Koo, D. C., et al. 2014, The Astrophysical Journal, 794, 156
Rubin, K. H. R., Weiner, B. J., Koo, D. C., et al. 2010, The Astrophysical Journal, 719, 1503
Rubin, V. C., & Ford, Jr., W. K. 1970, The Astrophysical Journal, 159, 379
Sargent, W. L. W., & Searle, L. 1970, The Astrophysical Journal Letters, 162, L155
Schaerer, D. 2003, Astronomy & Astrophysics, 397, 527
Schaerer, D., de Barros, S., & Sklias, P. 2013, Astronomy & Astrophysics, 549, A4
Schenker, M. A., Robertson, B. E., Ellis, R. S., et al. 2013, The Astrophysical Journal, 768, 196
Schmidt, K. B., Rix, H.-W., da Cunha, E., et al. 2013, Monthly Notices of the Royal Astronomical Society, 432, 285
Seifert, W., Appenzeller, I., Baumeister, H., et al. 2003, in Society of Photo-Optical Instrumentation Engineers (SPIE) Conference Series, Vol. 4841, Instrument Design and Performance for Optical/Infrared Ground-based Telescopes, ed. M. Iye & A. F. M. Moorwood, 962–973
Shapley, A. E., Steidel, C. C., Pettini, M., & Adelberger, K. L. 2003, The Astrophysical Journal, 588, 65
Shaver, P. A., Wall, J. V., Kellermann, K. I., Jackson, C. A., & Hawkins, M. R. S. 1996, Nature, 384, 439

Shen, S., Madau, P., Conroy, C., Governato, F., & Mayer, L. 2014, The Astrophysical Journal, 792, 99
Shim, H., Chary, R.-R., Dickinson, M., et al. 2011, The Astrophysical Journal, 738, 69
Silk, J., & Rees, M. J. 1998, Astronomy & Astrophysics, 331, L1
Silverman, J. D., Green, P. J., Barkhouse, W. A., et al. 2008, The Astrophysical Journal, 679, 118
Skelton, R. E., Whitaker, K. E., Momcheva, I. G., et al. 2014, The Astrophysical Journal Supplements, 214, 24
Smit, R., Bouwens, R. J., Labbé, I., et al. 2014, The Astrophysical Journal, 784, 58
Sobral, D., Best, P. N., Matsuda, Y., et al. 2012, Monthly Notices of the Royal Astronomical Society, 420, 1926
Sobral, D., Best, P. N., Smail, I., et al. 2014, Monthly Notices of the Royal Astronomical Society, 437, 3516
Sobral, D., Smail, I., Best, P. N., et al. 2013, Monthly Notices of the Royal Astronomical Society, 428, 1128
Sobral, D., Best, P. N., Geach, J. E., et al. 2009, Monthly Notices of the Royal Astronomical Society, 398, 75
Springel, V. 2005, Monthly Notices of the Royal Astronomical Society, 364, 1105
—. 2010, Annual Reviews of Astronomy & Astrophysics, 48, 391
Springel, V., White, S. D. M., Jenkins, A., et al. 2005, Nature, 435, 629
Stark, D. P., Ellis, R. S., & Ouchi, M. 2011, The Astrophysical Journal Letters, 728, L2
Stark, D. P., Schenker, M. A., Ellis, R., et al. 2013, The Astrophysical Journal, 763, 129
Stark, D. P., Richard, J., Charlot, S., et al. 2014a, arXiv: 1408.3649
Stark, D. P., Richard, J., Siana, B., et al. 2014b, Monthly Notices of the Royal Astronomical Society, 445, 3200
Steidel, C. C., Giavalisco, M., Pettini, M., Dickinson, M., & Adelberger, K. L. 1996, The Astrophysical Journal Letters, 462, L17
Steidel, C. C., Shapley, A. E., Pettini, M., et al. 2004, The Astrophysical Journal, 604, 534
Stinson, G. S., Dalcanton, J. J., Quinn, T., Kaufmann, T., & Wadsley, J. 2007, The Astrophysical Journal, 667, 170
Storey, P. J., & Zeippen, C. J. 2000, Monthly Notices of the Royal Astronomical Society, 312, 813
Stott, J. P., Sobral, D., Bower, R., et al. 2013, Monthly Notices of the Royal Astronomical Society, 436, 1130
Straughn, A. N., Meurer, G. R., Pirzkal, N., et al. 2008, The Astronomical Journal, 135, 1624
Straughn, A. N., Kuntschner, H., Kümmel, M., et al. 2011, The Astronomical Journal, 141, 14
Stromberg, G. 1925, The Astrophysical Journal, 61, 353
Strömgren, B. 1933, Zeitschrift für Astrophysik, 7, 222
Swinbank, A. M., Sobral, D., Smail, I., et al. 2012, Monthly Notices of the Royal Astronomical Society, 426, 935
Tacconi, L. J., Neri, R., Genzel, R., et al. 2013, The Astrophysical Journal, 768, 74
Tauber, J. A., Mandolesi, N., Puget, J.-L., et al. 2010, Astronomy & Astrophysics, 520, A1
Teyssier, R. 2002, Astronomy & Astrophysics, 385, 337
Teyssier, R., Pontzen, A., Dubois, Y., & Read, J. I. 2013, Monthly Notices of the Royal Astronomical Society, 429, 3068
Tisserand, P., Le Guillou, L., Afonso, C., et al. 2007, Astronomy & Astrophysics, 469, 387
Toomre, A. 1964, The Astrophysical Journal, 139, 1217
Tosi, M., Greggio, L., & Focardi, P. 1989, Ap&SS, 156, 295
Tremonti, C. A., Heckman, T. M., Kauffmann, G., et al. 2004, The Astrophysical Journal, 613, 898
Treu, T., Schmidt, K. B., Trenti, M., Bradley, L. D., & Stiavelli, M. 2013, The Astrophysical Journal Letters, 775, L29
Trump, J. R., Weiner, B. J., Scarlata, C., et al. 2011, The Astrophysical Journal, 743, 144
Trump, J. R., Konidaris, N. P., Barro, G., et al. 2013, The Astrophysical Journal Letters, 763, L6
Tu, H., Gavazzi, R., Limousin, M., et al. 2009, Astronomy & Astrophysics, 501, 475
van der Wel, A., Straughn, A. N., Rix, H.-W., et al. 2011, The Astrophysical Journal, 742, 111
van der Wel, A., Bell, E. F., Häussler, B., et al. 2012, The Astrophysical Journal Supplements, 203, 24

van der Wel, A., van de Ven, G., Maseda, M., et al. 2013, The Astrophysical Journal Letters, 777, L17
van der Wel, A., Franx, M., van Dokkum, P. G., et al. 2014, The Astrophysical Journal, 788, 28
van Dokkum, P. G., Quadri, R., Marchesini, D., et al. 2006, The Astrophysical Journal Letters, 638, L59
van Dokkum, P. G., Brammer, G., Fumagalli, M., et al. 2011, The Astrophysical Journal Letters, 743, L15
van Dokkum, P. G., Leja, J., Nelson, E. J., et al. 2013, The Astrophysical Journal Letters, 771, L35
Vernet, J., Dekker, H., D'Odorico, S., et al. 2011, Astronomy & Astrophysics, 536, A105
von Hoerner, S. 1960, Zeitschrift für Astrophysik, 50, 184
—. 1963, Zeitschrift für Astrophysik, 57, 47
Weiner, B. J., Willmer, C. N. A., Faber, S. M., et al. 2006, The Astrophysical Journal, 653, 1027
Weisz, D. R., Dolphin, A. E., Skillman, E. D., et al. 2014, The Astrophysical Journal, 789, 147
Weisz, D. R., Dalcanton, J. J., Williams, B. F., et al. 2011, The Astrophysical Journal, 739, 5
Willman, B., Dalcanton, J. J., Martinez-Delgado, D., et al. 2005, The Astrophysical Journal Letters, 626, L85
Wuyts, S., Förster Schreiber, N. M., van der Wel, A., et al. 2011, The Astrophysical Journal, 742, 96
Xue, Y. Q., Wang, S. X., Brandt, W. N., et al. 2012, The Astrophysical Journal, 758, 129
Yang, Y., Zabludoff, A. I., Davé, R., et al. 2006, The Astrophysical Journal, 640, 539
Zahid, H. J., Kashino, D., Silverman, J. D., et al. 2014, The Astrophysical Journal, 792, 75
Zanstra, H. 1927, The Astrophysical Journal, 65, 50
Zaritsky, D., Smith, R., Frenk, C., & White, S. D. M. 1993, The Astrophysical Journal, 405, 464
Zolotov, A., Brooks, A. M., Willman, B., et al. 2012, The Astrophysical Journal, 761, 71
Zucker, D. B., Kniazev, A. Y., Bell, E. F., et al. 2004, The Astrophysical Journal Letters, 612, L121
Zwicky, F. 1933, Helvetica Physica Acta, 6, 110
—. 1957, Publications of the Astronomical Society of the Pacific, 69, 518

Acknowledgements

It is a very pleasant aspect of life that some of the best things seem to happen almost by accident: when I chose of all places to come to Heidelberg (Hans-Walter, let this bit of plagiarism slide as I am paying homage)... It is harder for me to steal some text from your Acknowledgements, Arjen, but you were right that *Het is tijd om te vertrekken.* I really can not thank the two of you enough for giving me a chance. The wheels-within-wheels of HWR's brain determined that this would be a good pairing, and I would certainly say that it was. I could write more about how lucky and happy I am to have worked with you two, but I would prefer to hold those thoughts until I am buying you all beers on my massive postdoc salary; I am not going too far away, so you will not have seen the last of me. Hopefully I have made you proud.

I certainly consider myself incredibly lucky to have a family that allowed me to study whatever I wanted, even if it meant a BS in English and Astrophysics. That I chose to pursue the latter "professionally" without so much as a tiny complaint speaks volumes about the trust that they have in me. I love you all, and I am doing my best every day to make you proud. It is a tremendous shame that my grandparents are not around to see this, but I know that a Dr. Maseda (fingers crossed still, it is not official yet) would have put a smile on their faces.

Likewise, I want to thank the people who I worked with in the past, spending a lot of their own time and resources on bringing me into the scientific community: Jason Rhodes, Joel Bergé, George Djorgovski, Joe Hennawi, and Andrew Benson. None of you had to do this, but I am certainly grateful that you did! A special thanks goes to (Commander) Richard Ellis, who agreed to chat with an even more naïve Michael almost eight (!) years ago and helped me get my first SURF project. You mentored me for four years and actually convinced me that living in Europe was the best thing for me personally and professionally. A huge part of my life, actually, hinged on that decision, and I am glad that I trusted the right person.

So many people have been there for me when I have had questions, or just served as a role model for the type of scientist that I want to be, whether you know it or not: Wallace Sargent (RIP), Anneila Sargent, Marijn Franx, Elisabete da Cunha, Camilla Pacifici, Fabian Walter, Pascal Oesch, Ricardo Amorín, David Hogg, Vivi Tsalmantza, Brent Groves, Jon Trump, Shannon Patel, Dan Stark, Michelle Collins, Sharon Meidt, Kevin Bundy, Tommaso Treu, Eric Bell, Harry Ferguson, Tom Herbst, Dave Thompson (and the rest of the LBT staff), K. G. Lee, Andrea Macciò, Stijn Wuyts, Andreas Aebi, David Politzer, Lynne Hillenbrand, Frank Rice, ...

Also to the 3D-HST crowd, for making me feel welcome from the beginning and sharing your data with me: Gabe Brammer, Iva Momcheva, Pieter van Dokkum, Danilo Marchesini, Unicorn (of course), and everyone else. Mattia Fumagalli and Joel Leja: I will thank you only if we go back to Uganda!

On a personal level, so many people have helped make MPIA and Heidelberg such a pleasant 0.25+3.5 years of my life. The Office 216B stalwarts, Ilya Khrykin and Eduardo Bañados: at the very least you all made me feel guilty about taking naps in the afternoon (I still did, though). Taisiya Kopytova, Sasa Tsatsi, Paolo Bianchini, Iryna Butsky: you all know your place in my heart, so come and visit me in Ongieland! Likewise for Mario Gennaro, Kasper Schmidt, Yu-Yen Chang, Karsten Dittrich, Markus Schmalzl, Marion Dierickx, Miguel Querejeta, Emer Brady, Richard Teague, Anders Thygesen, Ben Laevens, Jakob Herpich (an abstract wizard!), the 8:27 am bus crowd, and all of my fantastic IMPRS generation (we will always have the art gallery in Prague)!

Ioana Aanei: you have helped me keep the wheels on more often than you probably know. It is not easy living across the Atlantic from so many good friends, but hopefully I will be able to come and visit more often (or in this case, at all). Jonathan Newkirk: I will look for an apartment in Leiden with a balcony so we can continue to Skype-stogie. Andrew Stealey and Carlos Ramirez: I will eventually drag you to Miami, mark my words.

Perhaps most importantly, I want to thank Chris Berlind and Ben Faber for being six or seven time zones away so I can actually get some work done in the mornings.

I wish to recognize and acknowledge the very significant cultural role and reverence that the summit of Mount Graham has always had within the red squirrel community. We are most fortunate to have the opportunity to conduct observations from this mountain.

There is no way that I remembered everyone, and there probably is not enough space even if I did. If you are reading this, I probably should be thanking you. Thank you!